DE TTK

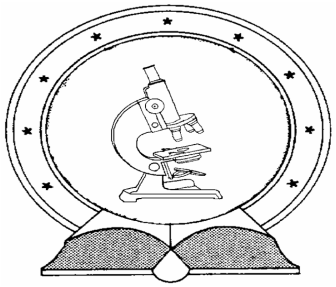

1949

Methods to measure low cross sections for nuclear astrophysics

PhD Thesis
Egyetemi doktori (PhD) értekezés

Tamás Szücs

Supervisor / Témavezető
Dr. Zsolt Fülöp

University of Debrecen
PhD School in Physics

Debreceni Egyetem
Természettudományi Doktori Tanács
Fizikai Tudományok Doktori Iskolája

Debrecen, 2012

Prepared at
the University of Debrecen
PhD School in Physics
and
the Institute of Nuclear Research
of the Hungarian Academy of Sciences
(ATOMKI)

Készült
a Debreceni Egyetem
Fizikai Tudományok Doktori Iskolájának
Magfizikai programja keretében
a Magyar Tudományos Akadémia
Atommagkutató Intézetében
(ATOMKI)

Ezen értekezést a Debreceni Egyetem Természettudományi Doktori Tanács Fizikai Tudományok Doktori Iskola Magfizika programja keretében készítettem a Debreceni Egyetem Természettudományi doktori (PhD) fokozatának elnyerése céljából.

Debrecen, 2012.

Szücs Tamás

Tanúsítom, hogy Szücs Tamás doktorjelölt 2008-2012 között a fent megnevezett doktori iskola magfizika programjának keretében irányításommal végezte munkáját. Az értekezésben foglalt eredményekhez a jelölt önálló alkotó tevékenységével meghatározóan hozzájárult.
Az értekezés elfogadását javaslom.

Debrecen, 2012.

Dr. Fülöp Zsolt
témavezető

Methods to measure low cross section for nuclear astrophysics

Értekezés a doktori (PhD) fokozat megszerzése érdekében a fizika tudományágban

Írta: Szücs Tamás okleveles fizikus és fizika szakos tanár

Készült a Debreceni Egyetem Fizikai Tudományok Doktori Iskolája
Magfizika programja keretében
a Magyar Tudományos Akadémia Atommagkutató Intézetében
(ATOMKI)

Témavezető: Dr. Fülöp Zsolt

A doktori szigorlati bizottság:

elnök: Dr. ....
tagok: Dr. ....
Dr. ....

A doktori szigorlat időpontja: 2011. .....

Az értekezés bírálói:

Dr. ....
Dr. ....

A bírálóbizottság:

elnök: Dr. ....
tagok: Dr. ....
Dr. ....
Dr. ....
Dr. ....

Az értekezés védésének időpontja: 2012. .....

Contents

Introduction

After the discovery of nuclear reactions by E. Rutherford in 1917 (published in 1919 [1]) and the precise measurements of atomic masses by F. W. Aston in 1920 [2], almost immediately A. Eddington suggested that stars obtain their energy from nuclear fusion of hydrogen to form helium. After G. Gamow calculated the quantum mechanical probability for particles to tunnel through potential barriers [3] R. d'E. Atkinson and F. G. Houterman suggested that this quantum mechanical tunneling may explain the energy generation of stars via fusion reactions [4]. Later H. Bethe analysed the different possibilities for reactions by which hydrogen is fused into helium [5]. The explanation of the origin of the heavy elements was presented later by R. A. Alpher, H. Bethe, and G. Gamow [6]. Reviews of the origin of the elements was given first in 1957, when E. M. Burbidge, G. R. Burbidge, W. A. Fowler, F. Hoyle [7] and independently A. G. W. Cameron [8] summarised the existing knowledge. From their work, Nuclear Astrophysics was born. They described the main processes, through which the elements were formed. Since then, many details of these processes were fine tuned and described in textbooks [9–11]. However, many open problems remain and experimental and theoretical physics efforts are needed to resolve them.

The aim of my work is to present improved methods to measure charged particle induced reaction cross sections of astrophysical interest.

In chapter 1 I summarise the main path of the nucleosynthetic processes. Most of them need further data to understand the element composition of the universe, the structure and stability of stars, and time evolution and material ejection by supernovae explosions. Most of these reactions occur

in such environment where – on nuclear physics scale – the reaction energies are low resulting small cross sections. In case of charged particle induced reactions – which are in the scope of this work – the reaction energies are mainly below the Coulomb barrier, and the cross sections are dropping exponentially towards lower energies. Other scenarios, like the heavy element synthesis, involves huge reaction networks mostly on radioactive nuclei. These reactions are modelled theoretically. Each theory, however, require experimental validation. The main topic of our work in the Nuclear Astrophysics Group at Institute of Nuclear Research of Hungarian Academy of Sciences (ATOMKI) is to perform this, to measure experimental cross sections to pin down the theories.

It is experimentally cumbersome to measure these tiny cross sections. In the following work I introduce methods, which are useful for experiments if small signals related to γ- or X-ray emission have to be measured. These quantities are the keys to understand the chemical evolution of the universe.

In chapter 2 an introduction is given about the "signal" and the "noise" in γ-spectroscopy, and about their relation to mathematical statistics.

Two basic methods to measure cross sections via γ-detection are reviewed in chapter 3. This chapter also contains the details of signal related quantities.

Introduction about the laboratory background and general reduction methods is given in chapter 4. I made laboratory background measurements in several laboratories with different detectors to test the effect of the overburden on the laboratory background. As a member of the LUNA collaboration I had access to a deep underground physics laboratory, where part of my measurements was done. Additionally I tested the effect of the active shielding on the laboratory background at these different sites.

My own measurements related to the underground studies will be introduced in chapter 5, where the used detectors, the studied sites, and the observed effects are detailed. A feasibility study is given about possible accelerator based cross section measurements at underground laboratories. These are in the front line of nuclear astrophysics studies to understand the energy production of stars and neutrino production in our Sun, but the relevant energy range can be reached experimentally only at an underground

location.

In chapter 6 I introduce the possibility of activation method combined with the X-ray counting, a method where higher signal is expected than in normal γ-counting. At the beginning of this chapter details of the counting systems and the derived sensitivities are presented. I designed and tested a shield, which provides improved sensitivity in the X-ray region. Details of the shield and the calculations are also presented in this chapter. In section 6.3 the first application of X-ray counting for α-induced reaction cross section measurements on ^{169}Tm is presented. Details of the target preparations, irradiations, and countings are shown. In this mass range there are no experimental data for low energy α-capture reactions, however, the γ-process is very sensitive to these cross sections. The resulted data can be used to test the theoretical cross section calculations. The X-ray counting system opens the way to measure lower cross sections. At the end of the chapter a few possible γ-process related reactions, which turned to be measurable with the new method and the new counting system are shown.

Finally in the last chapter the summary of this work, both in English and in Hungarian is given.

Chapter 1

Nuclear Astrophysics

1.1 The main nucleosynthetic processes

In this chapter I introduce the synthesis of the elements based on the following textbooks [9–11]. The solar abundance of the elements is shown in fig. 1.1. The main nucleoshyntetic processes are the following:

During the Big Bang nucleosynthesis 76 % hydrogen, 24 % helium and a small fraction of heavier elements like ^{7}Li (less than 10^{-3} %) were formed. With few exceptions all the other elements were formed at different life phases of the stars.

One exception is the region of Li, Be, B. Those nuclei are much rarer than the neighbouring ones, because the binding energy of these nuclei is low, and the stellar environment can easily destroy them. These light elements are synthesised via spallation reactions in the interstellar medium from heavier nuclei.

First step in the life of a star is the hydrogen burning[1] phase, where protons are converted to helium. The net reaction is $4\,^1\mathrm{H} \rightarrow {}^4\mathrm{He} + 2\,e^+ + 2\,\nu_e$. Because many body reactions have very low probability, this reaction proceeds through two body interaction chains like the pp–chain and the CNO cycle. These processes are responsible for the energy production of the

[1] In astrophysics, the burning means nuclear fusion, and not oxidation as in chemistry.

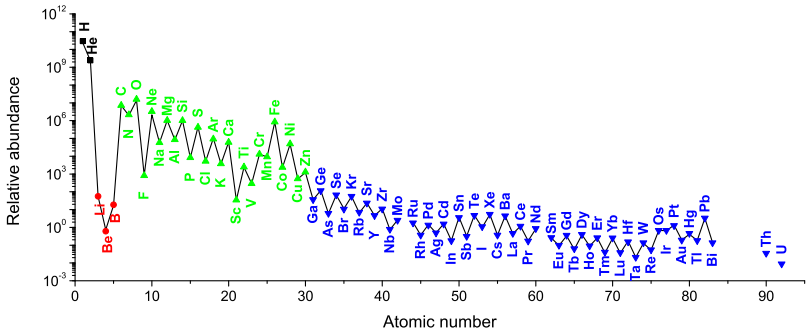

Figure 1.1: Abundance of the elements in the solar system. (Si = 10^6) [12]. The main nucleosynthetic processes are marked with different colors and described in the text.

stars. The pp–chain has bigger share in the energy production in lighter stars or it is unique in first generation stars, where no metals[2] are present. If there are metals in the core of a star, and the temperature is high enough, then carbon, oxygen and nitrogen can catalyse the hydrogen fusion. There are some other cycles, which have no importance in energy production, but in element synthesis. They require higher burning temperatures, and are called higher order CNO cycles, and advanced hydrogen burning cycles named by the involved catalytic elements, like Ne–Na cycle; Mg–Al cycle.

After the hydrogen is exhausted from the core, a contraction occurs and the star becomes hotter. In this phase the helium burning starts. The unstable ^{8}Be can not be the next step in the element synthesis, however it has sufficient half-life (10^{-16} s) to form a 2α–^{8}Be dynamical equilibrium. The next step is fusion with a third α particle within this lifetime. In this so called triple α process ^{12}C is formed. With further α-captures ^{16}O and a small fraction of ^{20}Ne are produced.

At stellar energies the α-capture rate of ^{16}O is so low, that further α-captures have small probability. However, the nucleosynthesis continues

[2]In astrophysics terms, all elements heavier than hydrogen and helium are called metals.

with carbon, neon, oxygen and silicon burning; and with the so called nuclear statistical equilibrium phase, where photodisintegration breaks up the nuclei before the fusion. The elements are built up to the iron region forming a peak in the abundance distribution.

The isotopes beyond the iron peak are mainly formed by neutron capture reactions. There are two neutron capture process chains, where the capture rate is very different.

The slow neutron capture process (s-process) has two sites: low mass thermally pulsing asymptotic giant branch stars (TP-AGB) for the main s-process ($A \geq 90$) [13] and massive stars for the weak s-process ($A = 60 - 90$) [14]. The neutrons for this process are produced in few burning reactions like $^{13}C(\alpha,n)^{16}O$ and $^{22}Ne(\alpha,n)^{25}Mg$. The characteristic time of the neutron capture is larger than the half-life of the β-decay of the radioactive nuclei close to the valley of stability (fig. 1.2), therefore, the path of the s-process follows that valley, and stops at ^{209}Bi, where the further neutron capture is followed by an α-decay, forcing the material into a loop.

The other reaction flow – the r-process – is named after the rapid neutron capture. It occurs in an explosive environment, where the neutron flux, therefore, the neutron capture rates, are higher than the rate of the β-decays. The path of the r-process goes far away from the valley of stability, close to the neutron drip line (fig. 1.2). This path is by-passing the α unstable region, which stops the s-process. When the neutron density drops, and the temperature decreases ("freeze out"), the material decays back to the stability via long β-decay chains. Such a high neutron density requires an explosive stellar environment. The exact r-process scenario is still under discussion, but the presently favoured candidates are core collapse supernovae [15] and merging neutron stars [16].

There are a few nuclei on the proton rich side of the valley of stability (fig. 1.2), which can not be produced either by s- or by r-process. They were formed by the so called p-process, which consist of several subprocesses, mainly γ-induced reactions, on the s- and r-seed nuclei (γ-process). The needed high energy photons for the γ-induced reactions are available in explosive nucleonsynthetic scenarios like the Ne/O burning layer in type II supernovae, where temperatures of around a few GK [17–20] are reached.

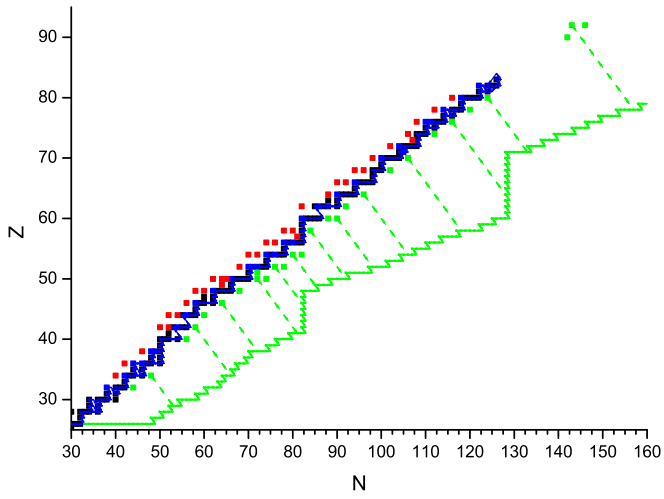

Figure 1.2: The main path of the *s*- and *r*-process (blue and green, respectively) on the isotope chart. Colored and black boxes are the stable isotopes. The *p*-isotopes are marked with red boxes.

With (γ,n) photodisintegration reactions, the material becomes proton rich, at a certain point (γ,p) or (γ,α) becomes more probable, and the material is pushed to the lower mass region [17, 18, 20, 21]. There are network calculations modelling the γ-process. They involve about 2000 nuclei and 10 000 reactions, most of them on unstable nuclei, therefore, the reaction cross section can be calculated only theoretically. To fine tune the theory or to produce direct cross section inputs to the network calculations, experimental data are highly needed. To find the related data, huge databases [22] should be reviewed and arranged [23].

The γ-process in its own, can not reproduce the abundance of the observed *p*-nuclei. Additional processes should exist, some of them are not yet confirmed, like rapid proton capture process [24], neutrino induced *p*-process [25]. To find out the share of the other processes, nuclear physics input of the γ-process should be well understood. In the heavy mass region ($140 \leq A \leq 200$) the reaction flow is strongly sensitive to (γ,α) photodisin-

tegration rates [20, 21]. If those rates are high, more material contributes to the synthesis of lower mass p-isotopes, however, if the reaction rates are lower, more material stays in the higher mass region. Consequently, to reproduce the path of the γ-process, experimental data are highly needed.

Photodisintegration cross sections can be directly determined by photon induced reaction studies [26]. However, in such an experiment the target nucleus is always in its ground state, whereas in stellar environment thermally populated excited states also contribute to the reaction rate. This leads to large corrections of the ground state rate, which can only be theoretically modelled [27]. The radiative capture reaction rates are less affected by the thermal population. So, it is advantageous to measure in the direction of particle capture and convert the measured rate to the rate of the inverse reaction by applying the principle of detailed balance [28, 29].

There are very few experimental cross section data related to the γ-process in the heavy mass region [30], because of the experimental difficulties, mostly caused by the low reaction energies consequently low yields.

Most of the experimental techniques to measure cross sections of astrophysical interest are based on detection of electromagnetic radiation (γ- or X-rays). My work deals with the detection of these radiations.

1.2 Typical energy range and reaction rates

In my work I deal with charged particle induced reactions, therefore I consider only these reactions in this section. The astrophysically relevant reactions occur at low energies compared to the Coulomb barrier of the nucleus. Naturally, these reactions are taking place in stars, where the "accelerator" is the thermal motion. At these energies, the Coulomb barrier has to be penetrated by quantum mechanical tunneling, leading to very low cross section values. In turn, this results in very low reaction rates.

The reaction rate is proportional to the product of two probabilities. The Boltzmann distribution of the thermal motion, and the tunneling probability. The former is determining, how many particle has a given energy at a certain temperature. The later comes from quantum mechanics, where

particles can react with non zero probability, even if they have not enough energy to overcome a potential barrier.

The Maxwell-Boltzmann distribution is proportional to $\exp(-\frac{E}{k_B T})$ (if $E > k_B T$) where k_B is the Boltzmann constant and T the temperature. The tunneling probability is proportional to $\exp(-(\frac{E_C}{E})^{1/2})$ where E_C is the height of the Coulomb barrier. The product of these two functions results in a peak, the so called Gamow peak (fig. 1.3). Recently, more detailed studies showed that in most cases the Gamow peak is even lower in energy than that of resulted by the simple equation [31]. The charged particle induced nuclear astrophysical reactions take place in this energy region, which lies higher than the average energy of the thermal motion, but not as high where the penetration factor can be ignored. For proton capture reactions on heavy elements at typical γ-process temperatures ($2-3\,\mathrm{GK}$) the Gamow peak lies between $1-5\,\mathrm{MeV}$, for the α-capture reactions between $5-13\,\mathrm{MeV}$. At these energies the reaction cross section is tiny, in some cases in the picobarn range. For experiments it is a big challenge to measure such tiny yields.

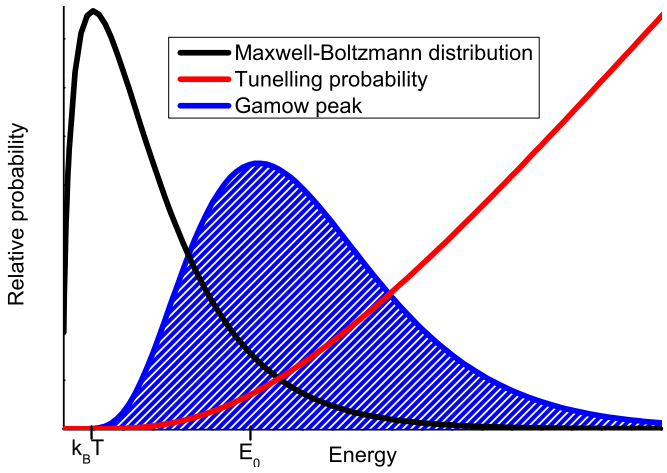

Figure 1.3: The so called Gamow-peak (strongly enlarged for clarity), the energy region where the nuclear reactions are taking place in an astrophysical object. E_0 is the Gamow-energy, at the maximum of the peak.

Chapter 2

Gamma-spectroscopy

This chapter summarises the statistics of counting, the behaviour of the statistical errors in counting experiments, and introduces the main response characteristic of γ-detectors. Finally, the peak area determination for γ-spectroscopy, and statistical limits – which are used later in this work – are given.

2.1 Counting statistics

In this section I shortly introduce the statistical behaviour of γ-counting. This is the summary of the relevant chapters from two textbooks, written by Knoll [32, Chapter 3] and Gilmore [33, Chapter 5].

Radioactive decay is a random process. Therefore, some degree of statistical fluctuation is involved in any measurement based on observing radiation emitted in a nuclear decay, therefore, mathematical statistics should be used to derive the results.

Basically, radioactivity counting involves a source, a suitable detector for the radiation emitted by the source, a scaler to count those decay events that are detected and a timer. If we measure the rate of detection of events, we can directly relate this to the number of radioactive atoms present in the source. The basic premise is that the activity ($\equiv$ decay rate) of the

sample (R) is proportional to the number of atoms of radioactive nuclide present (N), while the proportionality constant is the decay constant (λ):

$$R = -\frac{dN}{dt} = \lambda N \tag{2.1}$$

Therefore, if the number of events (C) detected by the detector in a fixed period of time (Δt) is counted, the decay rate can be estimated as follows (if $\Delta t \ll \frac{1}{\lambda}$):

$$R = \frac{C}{\epsilon \Delta t} \tag{2.2}$$

where ϵ is the absolute efficiency of the counting.

All scientific measurements are estimates of some unattainable true measurement, this is particularly true of radioactivity measurements, because of the statistical nature of radioactive decay. This fundamental uncertainty underlies all radioactivity measurements, and is in addition to the usual uncertainties (random and systematic) imposed by the measurement process itself. Several statistical models can be used in case of radioactivity counting.

The statistics of radioactive decay is **binomial** in nature, because:

- there are two possible states for each atom (either decayed or still present)
- the probability of an atom decaying during the count period is independent of how many times we repeat the counting
- the decay of one particular atom does not affect the probability of other atoms decaying

The binomial distribution is the most general model and widely applicable to all processes where the probability of success (p) is constant. In case of radioactive decay this is the probability that the atom decays during the period of the measurement (Δt):

$$p = \left(1 - e^{-\lambda \Delta t}\right) \tag{2.3}$$

The binomial distribution predicts that, in any particular sample of n atoms, the probability of x atoms decaying in a given time is:

$$P(x) = \frac{n!}{(n-x)!x!} p^x \, (1-p)^{n-x} \tag{2.4}$$

Unfortunately, it is computationally cumbersome in case of radioactive decay, where the number of nuclei is always very large.

The next used model is the **Poisson** distribution, which is the direct mathematical simplification of the binomial distribution, when p is small and constant (see fig. 2.1). Practically it applies when the observational time is small enough, compared to the half-life. Then the number of radioactive nuclei remains essentially constant during the observation, and the probability of recording a count from a given nucleus in the sample is small. This model is used in the case of low count rate systems, where the total accumulated counts are less than 20 or 30. The distribution is asymmetric, therefore, the mean value and the most probable value (mode) is not the same. Furthermore, the uncertainty of a given value following this distribution is asymmetric.

Further simplification is the **Gaussian** distribution, if the average number of success is relatively large (see fig. 2.2). This condition is fulfilled when more than a few counts is accumulated during the measurement. This distribution is symmetric, therefore, the mean value and the mode is the same.

Other important property of the distributions is the variance. Its square root is the standard deviation, and with multiplying factors it can be used as the uncertainty of the derived values.

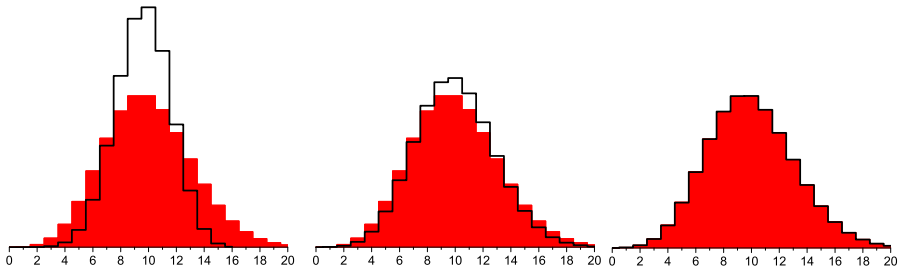

Figure 2.1: Black histograms are binomial distributions around mean of 10, with p = 0.6; 0.02; 0.001, respectively. Red full areas are Poisson distribution with mean of 10. With decreasing p the binomial and Poisson distributions become similar.

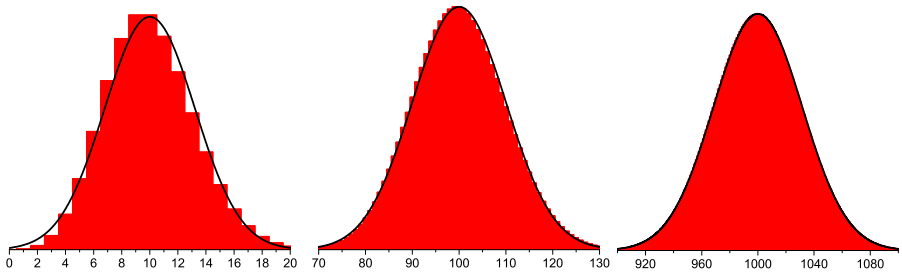

Figure 2.2: Red histograms and black curves are Poisson and Gaussian distributions, respectively, for mean equal to 10; 100; 1000. They become more and more similar.

Table 2.1: The most common statistical models, used in radioactivity counting measurements.

	Binomial	Poisson	Gaussian
Distribution	$P(x) = \frac{n!}{(n-x)!x!} p^x (1-p)^{n-x}$	$P(x) = \frac{(pn)^x e^{-pn}}{x!}$ $= \frac{\bar{x}^x e^{-\bar{x}}}{x!}$	$P(x) = \frac{1}{\sqrt{2\pi pn}} \exp\left(-\frac{(x-pn)^2}{2pn}\right)$ $= \frac{1}{\sqrt{2\pi\bar{x}}} \exp\left(-\frac{(x-\bar{x})^2}{2\bar{x}}\right)$
Mode	$(n+1)p$ or $(n+1)p-1$	$pn-1$ $= \bar{x}-1$	pn $= \bar{x}$
Mean	$\bar{x} = pn$	$\bar{x} = pn$	$\bar{x} = pn$
Variance	$\sigma^2 = np(1-p)$ $= \bar{x}(1-p)$	$\sigma^2 = np$ $= \bar{x}$	$\sigma^2 = np$ $= \bar{x}$

2.2 Gamma detection

2.2.1 Interactions between γ-rays and detector material

In this work, I deal with electromagnetic radiation (γ- and X-rays). To detect them, it is essential to know about their interaction with material. The γ- and X-rays interact with the detector material mainly by the following processes:

- Photoelectric absorption
- Compton scattering
- Pair production
- Coherent scattering

In the photoelectric absorption the full γ-energy is given to an atomic electron, and it is ejected from one of the bound shells of the atom. The interaction can not take place with free electrons, because of the energy and momentum conservation. The most probable origin of the photoelectron is the most tightly bound shell. Through the interaction an ionised absorber atom is also created with a vacancy. This vacancy is quickly filled, and one or more Auger electrons or characteristic X-ray photons may be generated. In most cases these X-rays are absorbed close to the origin through photoelectric absorption involving less tightly bound shells. Their migration and possible escape from the detector can influence their response (see Escape peaks in sec. 2.2.3).

At Compton scattering the γ-quantum interacts with a free or a less tightly bound electron. In this scattering some energy is transfered to the e^-, and the photon also changes its direction. Because all angles of deflection are possible, the energy transferred to the electron can vary from zero to large fraction of the γ-ray energy, but it never reaches the full γ-energy.

In case of pair production, energetic γ-radiation ($E_\gamma > 1022\,\mathrm{keV}$) creates $e^- - e^+$ pair in the Coulomb-field of a nucleus. All the excess energy (carried by the photon above the 1022 keV required to create the pair) goes into

kinetic energy shared by the positron and electron. After slowing down, the positron annihilates with an electron, and produces two 511 keV photons. The subsequent fate of this annihilation radiation has important effect on the detector response (see Escape peaks in sec. 2.2.3).

During the coherent scattering the γ-ray interacts coherently with all the electrons of an atom. This scattering neither excites nor ionises the atom, and the γ-ray is re-emitted after the absorption with unchanged energy but different direction. There is no energy transfer to the material, therefore, the coherent scattering can not play role in generation of detector signal, and there is no need to consider it later in this work.

2.2.2 Detector types used in this work

In each detector the γ-ray energy is transferred to electrons, and – in the case of pair production – positrons with the above mentioned processes. These particles lose their kinetic energy by scattering within the detector. The difference between the detectors comes from this point, how to transform this energy to a proportional charge signal, which can be read out by the data acquisition system.

The typical energy range of the radiation is between 15 keV and 15 MeV in nuclear astrophysics related radiative capture measurements. The lower border is usually in activation measurements, where the radiation follows the decay of a radioactive isotope. The upper border is reached when the prompt γ-ray after a capture reaction with positive Q value is detected. In this work I deal with two main types of radiation detectors. Short general introduction about their signal producing mechanism, and signal read out is given in this section.

Semiconductors

In solids the electron energy levels form bands, each of which can contain a fixed number of electrons. The uppermost occupied energy band called valence band, one above called conduction band. In case of semiconductors these bands are separated by a band gap of about 1 eV. A few electrons

from the valence band can move to the conduction band by thermal excitation, resulting in a highly temperature dependent small conductance compared to metals, in which there is no band gap. Cooling the material reduces the number of electrons in the conduction band, thereby reduces the background current.

In semiconductors the γ-rays created primary electrons have much higher energy than the band gap, so they can not directly take part in the charge signal. During scatterings from its energy electron-hole pairs are created. Electrons appear mainly in the bottom of the conduction band, the holes on the top of the valence band. This population of secondary entities forms the basis of the detector signal. By applying an electric field on the semiconductor crystal, the created secondary charge carriers are read out, and a detector pulse is formed.

Scintillators

Scintillators are insulators, therefore they have a wider band gap. The primary electrons raise secondary electrons to the conduction band, leaving holes in the valence band, but in some cases the energy given to the electron may not be quite sufficient to raise it to the conduction band. Then, the electron and hole could remain electrostatically attached as an entity called *exciton*. If the electrons de-excite by falling back to the valence band, they will emit electromagnetic radiation, which is in (or near) optical wavelengths. This light can be detected by a photomultiplier or other light measuring device to provide a detector signal.

2.2.3 Features of γ-spectra

The γ-spectrum is the digitalised form of the accumulated detector pulses. The output of a typical detector-preamplifier-amplifier system is a voltage impulse. The height of this impulse is proportional to the absorbed photon energy. This signal is digitalised, and according to its value, the number of counts in the corresponding channel is incremented. In the γ-spectrum these accumulated counts are shown as a function of the channel number

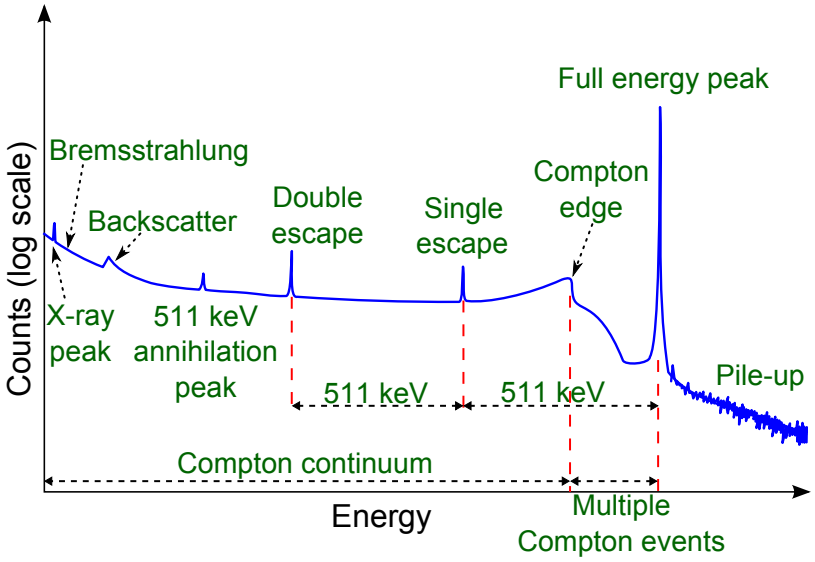

Figure 2.3: Typical semiconductor detector response to a monoenergetic γ-radiation, if its energy exceeds 1024 keV.

or – if the x-axis is rescaled (calibrated) – as a function of the energy.

A typical γ-ray spectrum is shown in fig. 2.3. Both semiconductors and scintillators have similar spectra, but the former has better energy resolution, and it has smaller probability to peak overlaps, therefore it was chosen as the example. The marked features are corresponding to the mentioned γ-interactions in the detector or the unavoidable interaction with the surroundings of the detector (shielding, cryostat, detector cup, source mount, etc.). In fig. 2.3 from right to left the features are:

Pile-up

The continuum above the full energy peak is due to random coincidences, when more than one γ-rays hit the detector within the signal processing time, and their energy add up. These events are determined by the statistical probability, in fact, by the sample count rate. The energy of the two absorbed γ-quanta do not summed up

fully, only part of the energy of the second pulse is added to the first one depending on their time overlap. (The second pulse sits on the tail of the first one.) Several standard main amplifier has a so called "pile-up rejection", which is the following: the amplifier produces an anti-coincidence gate for the ADC to reject the subsequent pulse within the shaping time of the amplifier, thus reduces pile-up events. The disadvantage of such a rejection system is the increased deadtime.

Full energy peak

The γ-ray hitting the detector volume releases its energy with the three mentioned processes. If the detector is big enough then the history of the Compton scattering, pair production and annihilation up to the photoelectric absorption have no importance, because the full γ-energy is converted to moving electrons (charge impulse), regardless in which process they are created. Because the γ-rays are identical, the detector response is the same, forming a peak at the incident γ-energy. If the detector were infinite thick, and a monoenergetic γ-radiation hit it with smaller rate than the signal processing rate, then just this peak would be in the spectrum, nothing else.

Sum peak

This feature is not shown in the example spectrum. In this case the source emits a number of γ-rays, and possibly X-rays practically simultaneously, and there is a certain probability that more than one of these is detected, and a peak is formed at the sum of their energy (sum–in). These counts are missing from the full energy peak (sum–out). The probability of the so called true coincidence summing depends on the nuclide decay scheme and the full energy peak as well as the total efficiencies of the detector. These events cannot be vetoed by the pile-up rejection, since the energies of both γ-rays absorbed withing the charge collection time of the detector, and only one pulse arrives to the input of the signal processing system.

Compton continuum, Compton edge and multiple Compton events

If γ-rays are Compton scattered in the detector volume, and release some energy, but after the event they escape, a count appears in the Compton continuum. The continuum has special shape, with a sharp edge on the high energy side (Compton edge). This is the highest energy which can be transferred with a single scattering event (when the γ-ray backscatters in 180°). Taking into account the mass of an electron (m_e), and the full energy of the γ-ray (E), the maximum possibly transferred energy within one scattering, thus the position of the Compton edge is at $2E^2/(m_e c^2 + 2E)$. Between the Compton edge and the full energy peak there are the multiple Compton events. These signals occur, when the γ-ray scatters more then once before it escapes from the detector.

Escape peaks

After the pair production, the e^+ annihilates with an e^- in the detector volume forming two 511 keV γ-rays. If the detector is big enough, these γ-rays are absorbed by the detector, and the signal appears in the full energy peak. However there is a certain probability, that one or both of these γ-quanta escape, and two peaks are formed in the spectrum exactly 511 keV and 1022 keV below the full energy peak.

Another type of escape peak can appear, which is not marked in the example spectrum. After the photoelectric absorption the deexcitation of the atom of the detector can occur by releasing a characteristic X-ray, if this X-ray escapes from the detector, a peak is formed a few keV below the full energy peak in the spectrum. This is the so called X-ray escape peak.

511 keV annihilation peak

If the radionuclide emits positrons as part of its decay process, then it is natural to observe the annihilation peak. However, it is worth remembering, 511 keV photons can also be expected in other cases. One possibility, if the pair production by the high energy γ-rays from the source appears outside the detector (e.g. in the shield), and one

of the annihilation γ-s reaches the detector. Pairs can be produced in the shield also by energetic cosmic rays.

Backscatter

The γ-rays from the source can backscatter from the shielding. The relationship between the energy of the scattered γ-rays and scattering angle reveals that, whatever the initial energy is, the energies of backscattered γ-rays (all those scattered through more than 120°) are within the broad range $200-300\,\mathrm{keV}$. The result is that backscattered radiation appears as a broad, ill-shaped peak in the spectrum.

X-ray peaks

These peaks may appear below 90 keV. Those are the X-ray fluorescence of the shield, the source, the source impurities, if the source or cosmic rays excite them.

Bremsstrahlung

Bremsstrahlung is electromagnetic radiation produced by the interaction of fast electrons (β-particles) with the Coulomb field of the nucleus. The electron energy loss appears as a continuum of photons, largely apparent in the X-ray region, although in principle the maximum energy is that of the β-particle. Any source emitting β-particles will have a bremsstrahlung spectrum superimposed on the γ-ray spectrum. In practice, this is only significant if the β-particle energy is much greater than 1 MeV. The presence of this radiation causes a considerable increase in continuum background at low energy.

2.3 Peak area determination

In this section short introduction of the peak area determination is given following the textbook written by Gilmore [33, Chapter 5].

In γ-ray counting experiments, the signal is the peak area, that is proportional to the number of the γ-rays released by the source. The proportionality factor is the peak detection efficiency. In principle, the actual

distribution of counts in a peak is irrelevant; measurement of the peak area should require no more than a simple summation of the number of counts in each of those channels that we consider to be part of the peak, and subtraction of the background counts beneath the peak. This background usually represents the Compton continuum of other γ-ray interaction within the detector.

The number of gross counts (G) within the peak region can be precisely calculated, but only an estimation can be derived about the background counts (B). Usually the background level is estimated by using the channel contents at the upper and lower edges of the peak region. The net peak area (A), is the difference of the gross area and the background ($A = G - B$). In certain circumstances, when small peaks lie on large backgrounds, the uncertainty in the background estimate can dominate the total uncertainty of the peak area measurement.

The uncertainty of the peak area (σ_A) is the quadratic sum of the uncertainty of the gross area (σ_G) and that of the background (σ_B). Because of Poisson statistics the variance (σ^2) is numerically equal to the count itself, therefore,

$$\sigma_A = \sqrt{\sigma_G^2 + \sigma_B^2} = \sqrt{G + B} = \sqrt{A + 2B} \tag{2.5}$$

This expression is certainly correct for peak plus background counts in a single channel, but not valid for peak area calculations, where the variance of the background depends on how many channels are used in its estimation. If the regions used to estimate the background contains equally m channels on the left and on the right side of the peak region, then the exact expression is:

$$\sigma_A = \sqrt{A + B + \frac{n}{2m} B} \tag{2.6}$$

where n is the number of channels used for the peak area integration. If the background regions have not the same size, the variance of the background estimation is even more complicated. Considering B_1 as average background on the left side of the peak estimated from m_1 channels, while B_2 average background estimated from m_2 channels on the right side of the

peak, then the uncertainty of the peak area is:

$$\sigma_A = \sqrt{A + B + \frac{n^2}{4m_1^2 m_2^2}\left(m_2^2 B_1 + m_2^2 B_2\right)} \tag{2.7}$$

where B is the background under the peak: $B = n(B_1/m_1 + B_2/m_2)/2$

In the following calculations I will use eq. 2.5 to have simpler formulae.

2.4 Statistical limits

Because of statistical behaviour of counts, statistical uncertainty of results can be derived only within a confidence limit, and there are numerous decision limits. A short introduction will be presented on them.

2.4.1 Critical limit (L_C)

After the peak area has been measured, it is important to determine its statistical significance. The background and its uncertainty should be taken into account, not just the peak area. If there were no any background, then a single count in the peak would be significant anyway.

If the background has been measured repeatedly many times, a series of counts will be obtained which is distributed in a Gaussian fashion above and below the mean value, with standard deviation of σ_0.

About any particular measurement which has near zero net count, it should be decided if those counts are truly zero or represent a true positive value. There must be some level, which we can call the critical limit, above which we can be confident, to a degree, that a net count is valid. If the net counts are above a certain number (k) of standard uncertainties of the distribution of background counts, we would be confident that the peak existed. This multiplying factor would be selected to provide a predetermined degree of confidence in the conclusion. In case of critical limit determination, which is a one-tailed confidence, for 84.13 %; 90 %; 95 %; 99 % confidence levels the multiplying factor is $k = 1;\ 1.282;\ 1.645;\ 2.326$, respectively.

In practice the standard deviation of the background count distribution is not known, however, it is needed to the critical limit determination ($L_C = k\sigma_0$). Only the background estimate (B) is known, and because of its Poisson statistics, the variance of it is itself B. The variance of the net counts is the sum of the net counts, the background counts, and the variance of the background. In case of critical limit calculation the net counts equals to 0, and therefore the **critical limit** is:

$$L_C = k\sqrt{2B} \tag{2.8}$$

So, if the peak area exceeds L_C, it is significant.

2.4.2 Upper limit (L_U)

If the net count is below or equal to L_C, then the activity must be declared "not detected" and an upper limit should be quoted. So a level should be set, which exceeds the actual peak area, if any. The limit can be related to the distribution of counts, if the sample were measured repeatedly a large number of times. Accordingly $L_U = A + k\sigma_A$, where σ_A is the uncertainty of the actual measured value, and k is again the multiplicity factor of the one-tailed confidence. If A is less than zero then, although statistically reasonable, it does not represent a true situation, and A should not be included in the calculation. Using the eq. 2.5, the **upper limit** can be calculated as follows:

$$L_U = \begin{cases} k\sqrt{A+2B} & \text{if } A \leq 0 \\ A + k\sqrt{A+2B} & \text{if } A > 0 \end{cases} \tag{2.9}$$

2.4.3 Detection limit (L_D)

This is an other kind of limit than the previous. Those are *a posteriori* estimates based on actual measured counts. The detection limit answers an *a priori* question.

The detection limit should be above the critical limit, because if the activity is exactly the critical limit, than owning the fact of a symmetric distribution only 50 % of the counts are significant (above the limit). It is clear that L_D must be some way above L_C.

If the sample would be measured many times, the standard deviation of the detected counts is σ_D. Then the detection is certain, to a degree determined by k, if the net counts are more than the detection limit:

$$L_D = L_C + k\sigma_D \tag{2.10}$$

Using eq. 2.5 the standard deviation of the detected counts is:

$$\sigma_D = \sqrt{L_D + 2B} \tag{2.11}$$

Substituting eq. 2.8 and eq. 2.11 to eq. 2.10 using equal k factors, it results:

$$L_D = k\sqrt{2B} + k\sqrt{L_D + 2B} \tag{2.12}$$

Solving this quadratic equationon for L_D, the **detection limit** is given as follows:

$$L_D = k^2 + 2k\sqrt{2B} \tag{2.13}$$

To see graphically these limits, artificial spectra are shown in fig. 2.4. In most cases, if the peak area is above the detection limit it is visible by eye, meanwhile if it is less then L_D but significant, it is not clearly visible.

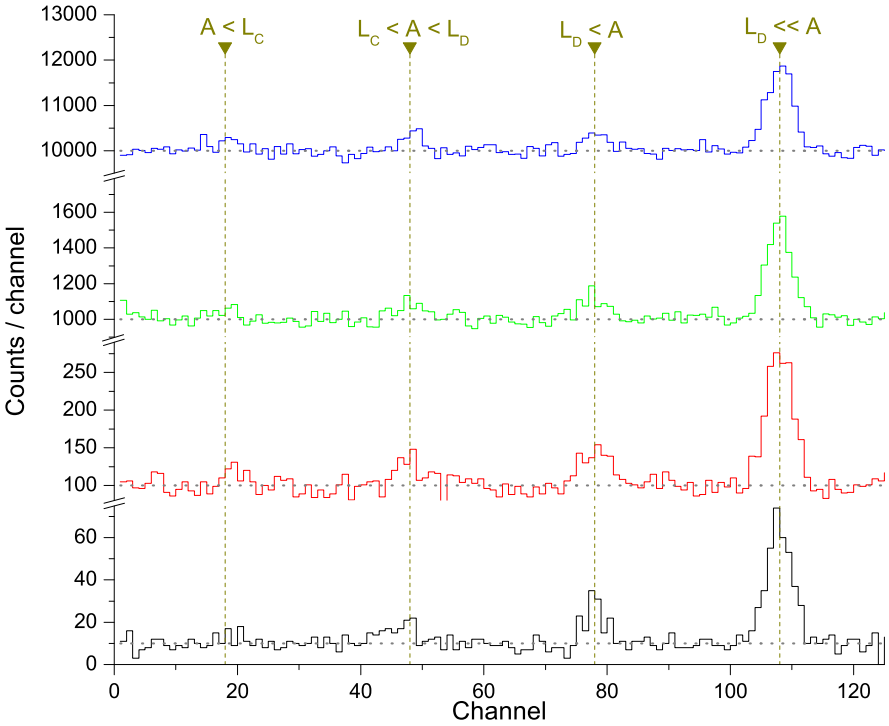

Figure 2.4: Artificial spectra with various peaks on different backgrounds. The average background levels (10; 100; 1000; 10000) are marked with grey dotted lines. The positions of the simulated peaks are marked with brown arrows and dashed lines. The full width at half maximum of the simulated peaks is 5 channels, and the peak areas were chosen to mach the indicated relations (for 95 % confidence) on the top.

2.4.4 Determination limit (L_Q)

The determination limit answers also an *a priori* question similar to the detection limit.

If the aim is to reach $i\,\%$ statistical uncertainty, then the standard deviation of the peak area (σ_Q) should be $i\,\%$ of L_Q. In equation form $L_Q = k_Q\sigma_Q$, where k_Q is the inverse of the required relative standard deviation. Using eq. 2.5, this turns to $L_Q = k_Q\sqrt{L_Q + 2B}$. The solution of this quadratic equation is:

$$L_Q = \frac{k_Q^2}{2}\left(1 + \sqrt{1 + \frac{8B}{k_Q^2}}\right) \tag{2.14}$$

Assuming a counting system where the background rate (b) and also the signal rate (s) are constant. Then the total background (B) and net peak area (A) counts during a given counting time (t) are the following:

$$B = bt \quad \text{and} \quad A = st \tag{2.15}$$

To calculate how long counting is necessary to reach a given statistical uncertainty, combination of the last equations can be used, assuming that the peak area is equal to the determination limit.

$$st = \frac{k_Q^2}{2}\left(1 + \sqrt{1 + \frac{8bt}{k_Q^2}}\right) \tag{2.16}$$

Solving for t this quadratic equation results:

$$t = \frac{k_Q^2}{s}\left(1 + \frac{2b}{s}\right) \tag{2.17}$$

the time requiring to reach given statistical uncertainty with constant signal and background rates.

2.5 Figure-of-merit

For us, the signal is the peak area, everything else is background. The error of the peak area is sensitive also to the background and not only to the net peak area as shown in eq. 2.5. The relative error is

$$\frac{\sqrt{A+2B}}{A} = \sqrt{\frac{1}{A} + \frac{2B}{A^2}} \tag{2.18}$$

The traditional S^2/B criterion for the figure-of-merit is coming from this expression.

It is seen that to improve the figure-of-merit the signal need to be enhanced or the background should reduced. The signal enhancement is more effective than the background reduction. In chapter 3 the sources and the enhancement methods of the signal, while in chapter 4 the sources and the reduction methods of the background are summarised.

Chapter 3

Signal in γ-spectroscopy

In this chapter an introduction about the signal in a counting experiment and its possible enhancement in different methods are given. The signal related quantities are also introduced.

3.1 Methods to determine reaction cross sections

For nuclear physics cross section determination, two main types of measurement are used, where electromagnetic radiation is observed: the in-beam γ-spectroscopy, and the activation method. Both of them have advantages and disadvantages, a short description is presented below.

3.1.1 In-beam γ-spectroscopy

After a particle capture reaction usually the product compound nucleus is formed in an excited state. During the rearrangement of its structure it can emit neutrons, protons, α-particles, depending on the excitation energy. During and after the particle emission the nucleus also loses its energy by γ-emission before it reaches the ground state. In most of the cases this process goes through several excited levels, and produces a bunch of γ-quanta. Detection of this radiation is the basis of the in-beam γ-spectroscopy.

In order to determine the total reaction cross section, the decay scheme of the produced nucleus with the intensities of the transitions must be known. If these parameters are not known, and some transitions remain undetected, an underestimation in the reaction cross section may occur. Ideally, the angular distribution of all transitions must be determined or known from other experiment. If a single detector setup is used, it should be placed at 55° or 125° with respect to the beam axis to minimise the effect of the angular distribution. The second-order Legendre polynomial approximately vanishes for these angles so that angular correlation effects are weakened at these angles. Other possible source of uncertainty is the Compton continuum of the high energy peaks, which give a background in the low energy region, and the weakest transitions can be buried. Usually very complicated γ-spectra have to be analysed for heavy nuclei. The extension of the method is using large detector arrays instead of a single detector (e.g. [34]) to cover as large solid angle as possible.

An alternative of this approach can be the angle-integrated γ-yield measurement using 4π summing scintillators [35]. The working principle of this method is the almost 100 % detection efficiency of the large volume scintillator crystal. All radiation emitted by the product nucleus is fully absorbed in the crystal, and since the transitions occur within the time resolution of the detector, they will result in an energy signal equal to the full energy of the compound nucleus decay, which is given by the reaction Q value plus the center of mass energy. Every count in the full energy peak corresponds to a capture reaction. This method is free from the necessity of measuring all transitions, and the angular distributions. However, the energy resolution of the scintillator is poor, care must be taken to avoid background reactions having similar Q values as the investigated one, since they may produce a similar energy sum peak in the spectrum. For example, highly enriched targets are needed, because the difference between the Q values of reactions on different isotopes of a heavy nucleus can be less than few hundred keV, consequently the full energy peaks could overlap.

The big advantage of the in-beam method is the wide applicability, because in principle every cross section of capture reactions followed by γ-emission can be measured with this method.

3.1.2 Activation method

Although the activation method is limited to those reactions where the product nucleus is radioactive, it has many advantages. The biggest advantage is the separation of the irradiation from the γ-detection. Thus, most of the problems encountered in in-beam cross section measurements can be avoided. There is no need to measure the angular distribution, because usually there is no effect which orders the activated atoms, therefore they are randomly distributed in the sample, and the angular distribution of the emitted radiation is isotropic.

The method is the following. The sample is irradiated by the ion beam provided by an accelerator, after this the activated sample is transported to a shielded detector, where the counting occurs. From the detected activity, the reaction cross section can be derived.

This approach was used in several experiments to measure proton- or α-induced cross sections at astrophysical energies in recent years [36–49]. In most of the cases the activation experiments have been carried out by the detection of γ-radiation following the β-decay of the reaction product. The exception is the ^{144}Sm(α,γ)^{148}Gd reaction, where the α-decay of ^{148}Gd has been measured [36].

Although the activation method proved to be very fruitful, it has some serious limitations. In order to have reasonable count rate in the γ-spectra, reactions leading to a final nucleus with long half-life (typically more than a few weeks) were usually excluded. Furthermore, the product nuclei must decay via the emission of at least one high intensity γ-transition. Moreover high efficiency detection is necessary to compensate the low cross section, long half-lives or low branchings. For this purpose a detector with high intrinsic efficiency, and/or close counting geometry must be used. The laboratory background can be reduced using a passive shielding, but the beam-induced background on the impurities of the target and/or the backing can still be present. Furthermore, if the reaction product decays via γ-cascades, in close geometry the true coincidence summing effect has to be also taken into account.

3.2 Variable quantities

In the following factors and their limitations are discussed, which are related to the signal in the two mentioned methods.

The detected counts (C) in the spectra is the product of the absolute detection efficiency (ϵ), the intensity of the investigated transition (I), and the number of decays (n) during the counting.

In case of in-bean spectroscopy every produced radioactive atom is decaying almost immediately except isomers. Taking into account the angular distribution of the radiation in the intensity factor the detected counts are given by:

$$C = \epsilon I \sigma \phi D t_i \tag{3.1}$$

where σ is the reaction cross section, ϕ is the incident particle flux, D is the areal number density of the target, and t_i is the duration of the irradiation.

In case of activation method the active atoms are produced during the irradiation, and their number are decreasing following the exponential decay law. Thus, the detected counts are given by:

$$C = \epsilon I \sigma \phi D \left(1 - e^{-\lambda t_i}\right) e^{-\lambda t_w} \frac{1 - e^{-\lambda t_c}}{\lambda} \tag{3.2}$$

where λ is the decay constant of the reaction product, t_w and t_c are the waiting time between the end of the irradiation and the beginning of the counting, and the duration of the counting, respectively. The other factors are the same as in eq. 3.1.

The factors and the dependence of the total counts on them are shown in eq. 3.1 and eq. 3.2. The question arises, *how can the total counts be increased?* In the following these factors are discussed one by one.

3.2.1 Detection efficiency (ϵ)

Detection efficiency enhancement can be done by decreasing the distance of detector and source, thus increasing the solid angle covered by the detector, but this method has physical limitations. In case of activation method the source can not be closer than the thickness of housing of the detector crystal. In in-beam case the situation is even worse, because the beamline, and the target holder also need space. In the case of activation method the so called well type detector can be used. Thus, the sample is inside the active volume of the detector, but this geometry can be used only in case of small samples and small activities. Also a problem with high efficiency is the higher probability of true coincidence summing effect.

In an in-beam measurement the covered solid angle can be increased by using more than one detector or large detector arrays.

The above mentioned methods change the absolute detection efficiency. There is a possibility to increase the intrinsic (relative) efficiency of a detector. Using a detector consisting of active volume of higher atomic mass, the total absorption of the radiation has higher probability. Also radiation with smaller energy has higher chance to get fully absorbed, thus every detector has decreasing efficiency with the detected energy. From this point of view, it is favourable to count γ-rays with smaller energy. (From the background point of view it is unfavourable, because the background counting rate is also the highest in the low energy region.)

3.2.2 Intensity of the investigated transition (I)

The branching ratio of transitions from a level is determined by nature. It is not always good to measure the transition with the highest intensity, because the detection efficiency also depends on the energy. In general it is favourable to count the radiation, where the product of the intensity and the efficiency ($\epsilon \cdot I$) is the highest.

It should be highlighted that both the absolute efficiency and the relative transition intensity have a maximum value of 1.00, the product of them can never be higher than one.

3.2.3 Beam current (ϕ)

Increase in the beam current is limited by the ion source, the accelerator and the beam optics, but also by the target itself. The target can not resist above a given released power without degradation, even if this process is well understood and monitored, at a certain point the number of target atoms becomes so low, that the measurement makes no sense any more.

3.2.4 Target thickness (D)

Increase of the number of target atoms has limitations, because the energy loss of incident particles in the target. In nuclear astrophysics we are interested in excitation functions, in other words, the energy dependence of the cross section. For this purpose, a good energy resolution is needed, because at astrophysical energies the cross section is changing exponentially. The beam energy can be well set with analysing magnets. Limitation comes from the target in which the beam loses energy. Particles interact with different energy in the front and in the back of the target. To minimise this effect thin targets are usually used.

In case of thick targets energy integrated cross section can be measured. Excitation function can be recorded also in this way, for this two yields should be subtracted from each other. If those are close to equal then the uncertainty of the derived value can be very large.

3.2.5 Measuring times (t_i, t_c and t_w)

In case of in-beam measurements with stable beam intensity the total accumulated counts are linearly proportional to the irradiation time, because γ-quanta are released only during the irradiation. Increasing the length of the irradiation is usually limited by the availability of the accelerator.

In case of activation the time factors are in exponential relation with the accumulated counts. To increase the number of detected counts, the irradiation and the counting time can also be increased, but both have upper limits. It makes no sense to increase the irradiation time several times longer than the half-life of the produced nucleus, because the accumulated

activity reaches a maximum value. This maximum is a dynamic equilibrium depending on the beam current. Counting time also depends on the half-life and the accumulated activity. After 10 times the half-life, the activity decreases three orders of magnitude, and usually can not be counted any more. The third timing factor is the waiting time, which should be minimised to increase the number of counts in the detector. Here the limitation often comes from the short lived parasitic activity created on target and backing impurities. The other open reaction channels from the investigated isotope can produce also parasitic activity, which is unavoidable. Those increase the background and the dead time of the detector, making hard to measure before their activity reaches a sufficiently low level.

Chapter 4

Background reduction

In this chapter the laboratory background and widely used reduction techniques are summarised.

4.1 The origin of the laboratory background

To reduce the laboratory background, its source has to be known. To show the typical features of the laboratory background spectrum, I measured it with a high purity germanium (HPGe) detector without any shielding at ATOMKI (fig. 4.1). Two different parts are clearly seen, which are different both in counting rate and in structure.

In the low energy part there are many peaks with rapidly decreasing average counting rate by increasing energy. As described in sec. 2.2, the γ-rays generate peaks in the spectrum. Most of the observed peaks come from γ-rays hitting the detector. All of them have Compton-continuum, which are superposed on each other. This is the reason of decrease in counting rate from the low to the high energy.

Above a certain energy, there are no more peaks observed. This part of the spectrum shows a flat distribution with much smaller slope of the average counting rate. The main source of this background is the energy loss of cosmic rays passing through the active detector volume.

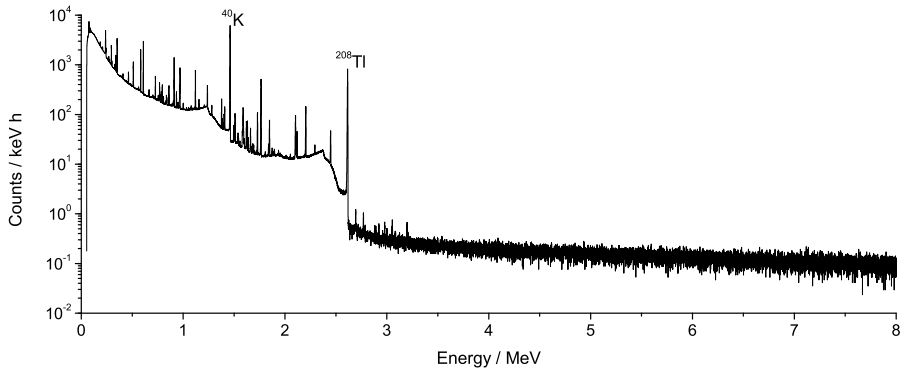

Figure 4.1: Measured laboratory background spectrum of a HPGe detector at Earth's surface without any shielding.

In the following, both parts will be discussed in details. To see the relative importance of the different background sources, the typical integral counting rate from the given source in a low-level HPGe detector of 1 kg mass located in a 10 cm thick lead shield is shown in the brackets after the titles. The values are adopted from [50].

4.1.1 Radionuclides in the environment ($30-300\,\mathrm{s}^{-1}$)

In the environment there are many radionuclides. The γ-rays following their decay are clearly visible in laboratory background spectra. The highest peak is at 1460.822 *6* keV originating from ^{40}K, a long lived radioisotope ($t_{1/2} = 1.248\,3 \cdot 10^9$ y [51]).[3] The natural abundance of this potassium isotope is 0.012 % [52], and it can be found everywhere in the environment. Its Compton edge is also clearly visible at 1243 keV. This value is in agreement with the maximum possibly transferred energy within one scattering mentioned in sec. 2.2.

[3] In this work I show the error of a given literature value with an italic number after the last digit(s). (For example in the above case 1460.822 *6* = 1460.822 ± 0.006)

The sources of the other peaks are the so called natural decay chains. Starting points of these chains are long lived transactinides like ^{232}Th, ^{238}U and ^{235}U for thorium, uranium and actinium series, respectively. These isotopes are decaying with series of α- and β-decays into stable elements. Along the chains there are several isotopes emitting γ-radiation with high probability. The most common radioactive isotopes detectable in the laboratory background are ^{228}Ac, ^{208}Tl from the thorium series and ^{214}Bi from the uranium series. The decay of ^{208}Tl shows a strong γ-line at 2614.511 *10* keV marked in the spectrum. Its Compton edge at 2382 keV is more prominent than that of the ^{40}K. Taking into account the natural γ-lines, 3 MeV is considered as border between low and high energy background regions, however, some peaks from true coincidence summing can appear above this value. This terminology for low and high energy range is used later in this chapter.

4.1.2 Cosmic rays ($0.3-2\,\mathrm{s}^{-1}$)

The composition of cosmic rays on the Earth's surface and their typical fluxes are the following [50]:

- the nucleonic part consists of energetic neutrons (97%), protons and some heavier nuclei ($66\,\mathrm{m}^{-2}\mathrm{s}^{-1}$)
- energetic muons, which are often called the hard component ($190\,\mathrm{m}^{-2}\mathrm{s}^{-1}$)
- electrons, positrons which are called the soft components ($46\,\mathrm{m}^{-2}\mathrm{s}^{-1}$)

The hard component has the biggest effect on the laboratory background. The main source of the high energy background in a germanium detector is the direct ionisation energy loss of energetic muons, which are passing through the shielding with practically no reduction. Slower muons may stop in the detector, however their average energy (≈ 4 GeV) is much higher than what can be fully absorbed in the crystal [53, Chapter 3]. The energy loss of the muons in germanium has an average value between $6-8$ MeV/cm [54, 55]. Therefore, the detector response for the muons

mostly depends on the geometry of the crystal, and not on the incident muon energy. The angular distribution of the muons is proportional to $\cos^2\theta$ (where θ is the zenith angle), so the most important quantity is the vertical length of the detector. The muons produce a broad peak in the spectra around $6-8$ times the length of the crystal, considering the energy in MeV and the length in cm.

Cosmic rays generate background not only via direct interaction, but through production of radionuclides in the detector or in the shielding material. Muons can be captured, the atomic number decreases by one, and the nucleus radiates γ-rays and fast neutrons when re-arranging its structure. Energetic muons can also directly knock out nucleons from the nucleus.

4.1.3 Neutrons ($0.03-0.2\,\mathrm{s}^{-1}$)

The main sources of neutrons are cosmic (cosmic neutrons), and secondary production by the cosmic ray muons (terrestrial neutrons). Other sources will be described in details along the shielding techniques in sec. 4.2.3.

Peaks can be formed in the laboratory background also by direct interaction of neutrons with the detector and shielding materials. These can be excited by inelastic scattering of neutrons. γ-rays following the de-excitation can be detected. In case of neutron inelastic scattering on germanium, sawtooth shape peaks are produced (fig. 4.2), which have the sharper edge on the low energy side. The Ge nuclei de-excite almost immediately compared to the time of the charge collection, therefore the de-excitation energy is summed with the continuously distributed recoil energy of the nucleus, including some quenching [57].

Another way of neutron interactions is capture reaction. After neutron capture, energetic γ-rays can be emitted depending on the reaction Q value. On the other hand the neutrons can activate the detector and the shielding material, producing radioactive isotopes. The decay of these isotopes may produce detectable γ-radiation, X-ray or bremsstrahlung.

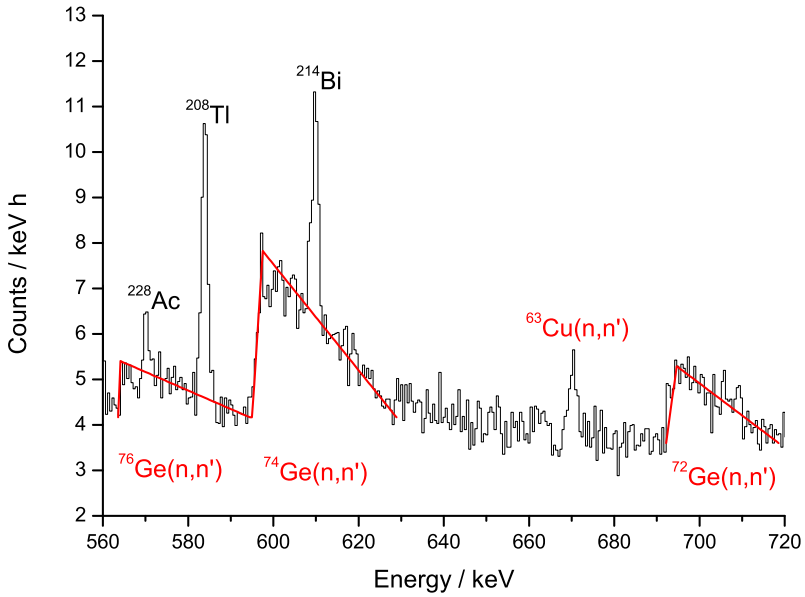

Figure 4.2: Sawtooth shaped peaks, highlighted by red lines produced by neutron inelastic scattering on germanium nuclei, in a laboratory background spectrum recorded by a HPGe detector at Earth's surface in a 15 cm thick lead shield lined with copper. Peak produced by neutron inelastic scattering on Cu also marked with red label [56]. Peaks produced by environmental radionuclides are marked with black labels.

4.1.4 Radioimpurities in the shield and in the detector material ($0.013 - 0.23\,\mathrm{s}^{-1}$)

The shield and the detector itself can contain radionuclides depending on the primordial radionuclide content of the ore the material is made of, or on the cosmic ray exposure of the material, and on the production method.

The most common contamination in the lead shielding is ^{210}Pb from the uranium series, and from cosmic ray production. The half-life of this isotope is 22.20 *22* y [58]. Because it is a radon daughter, it can be attached on the

surface of every detector part. ^{210}Pb itself usually does not contribute significantly to the background of Ge detectors as its very soft β-radiations (E_{max} of 16.5 keV and 63 keV) and γ-ray (46.5 keV) hardly escapes self-absorption. The main problem is the bremsstrahlung continuum with end point of 1162.1 *8* keV [58], due to the β-particles emitted by its daughter ^{210}Bi. The hard β-radiation also generates Pb X-rays with energies of 72.8 keV, 75.0 keV, 84.9 keV and 87.4 keV. ^{210}Pb can be present also in the solder of the crystal connection [59, 60]. Alpha particles emitted by its other daughter (^{210}Po) can reach the active volume of the crystal, and produce there high energy signals around 5.3 MeV.

Activated contaminations can sometimes be also important beside the residual primordial contaminations. Most important mechanisms of activation are secondary neutrons (at shallow depths or higher altitudes), and negative muon capture or fast muon interactions (at underground laboratories). For example ^{65}Zn can be produced by neutron activation on germanium, or ^{57,60}Co isotopes can be formed by activation of copper or nickel parts [56].

4.1.5 Radon ($0.01 - 0.1\,\mathrm{s}^{-1}$)

Radon is also part of the environmental radioactivity, however, it should be treated separately because it is a noble gas. Every decay chain includes one radon isotope. One of them – ^{222}Rn from the uranium series – has a few days long half-life ($t_{1/2} = 3.8235\,3$ d [61]). It emanates from the walls and ground, therefore, its daughters can be found everywhere. Air always contains radon, its equilibrium content depends on the ventilation of the room and the building material used. (The average indoor concentration is about 40 Bq/m^3 [62].) The admixture of ^{220}Rn from thorium series varies strongly, due to the much shorter half-life ($t_{1/2} = 55.6\,1$ s [63]) makes its concentration more sensitive to barometric pressure changes and other factors influencing the emanation.

4.1.6 Secondary radiation of the shield

Cosmic rays and the γ-radiation can excite the detector and the shielding materials. Usually the deexcitation is followed by X-ray production. These are recorded in the spectra as peaks below 100 keV. Cosmic rays can produce bremsstrahlung and neutrons in the shielding too, enhancing the average background continuum. This background source is strongly attached to the others and does not exist in its own, therefore its counting rate is included in the integral counting rate of its parent sources.

4.2 Laboratory background reduction methods

4.2.1 Shielding against environmental radioactivity

In order to reduce background from natural radioisotopes, a massive shield should be applied. Materials with high atomic number are the best way to attenuate γ-radiation. The most common shielding material is lead, because of its high atomic number, reasonable cost, and mechanical properties. Furthermore, it has low neutron capture cross sections and a favourably low interaction probability with cosmic rays, including the formation of radionuclides by activation. Unfortunately, its intrinsic radioactivity is generally not negligible, as described in sec. 4.1.4.

The continuum in the spectrum is attenuated almost independently of the energy [64]. It could be expected that the photons of lower energies would be absorbed more efficiently than those with higher energies. The reason that this does not occur is, that lower energy photons are continuously replenished by Compton-scattered photons of higher energies when passing through the thick layer of material. In this way the continuous spectrum reaches an equilibrium shape with a general attenuation coefficient. Unfortunately very thick shielding can not be applied because from a certain thickness (about 150 g/cm^2 [50, 65], which is about 13 cm in case of lead) the internal radioactive contaminations, and the secondary radiation (mainly neutrons produced by muons) does not allow further reduction of the background at Earth's surface.

4.2.2 Shielding against cosmic rays

Protons from the nucleonic component have low intensity compared to neutrons, moreover, they are converted to neutrons in nuclear reaction with construction materials of the building and with a metallic shield. The weak component and the charged nucleonic part are directly absorbed by the shield (10 – 20 cm of lead or 20 – 40 cm of iron). This absorption can be followed by secondary radiation, as described in sec. 4.1.6. To shield against the hard component of the cosmic ray, two main possibilities are widely used:

Active shield

The direct effect of the muons can be reduced with a veto detector. This is usually a scintillator or a proportional chamber on the top of the HPGe, or surrounding it. The signals from this guard detector are used as anti-coincidence gate. Every count from the germanium is excluded, when in a short time period the veto detector produces a signal as well. For example penetrating muons produce this kind of coincidence events. The advantage of proportional chamber is their small count rate, and hence negligible correction for dead time. Plastic scintillator veto detectors are more effective at sea level and shallow depth than gas counters. In order to keep the count rate of the scintillator at a rate that allows longer veto times ($>$ a few μs) an additional layer of lead should be used to shield against environmental γ-radiation.

If the veto detector is close to the other one, it also can be used as a Compton suppressor. Scattered γ-radiation can produce a signal in the veto detector, too. From this signal with suited electronics a veto gate signal can be formed, and the signal processing of the ADC can be disabled, thus counts from the Compton region can be excluded.

The indirect effect of the muons can not be suppressed in this way. The muon induced neutrons inside the shielding still contribute to the background even if a veto detector is applied.

Disadvantages of the active shield are the more complicated signal pro-

cessing chain, and the increased deadtime due to the random coincidences. In these cases the veto gates are also produced and the ADC is disabled. In case of a measurement where a cascade of γ-rays is emitted, the efficiency of the counting system may be decreased due to true coincidences events (if one γ-ray from the cascade hits the veto detector).

Passive shield

Cosmic rays can be attenuated by placing the setup in an underground location. In this case muons have to penetrate a big amount of material. Muons with lower energy are stopped, so that the spectrum becomes less

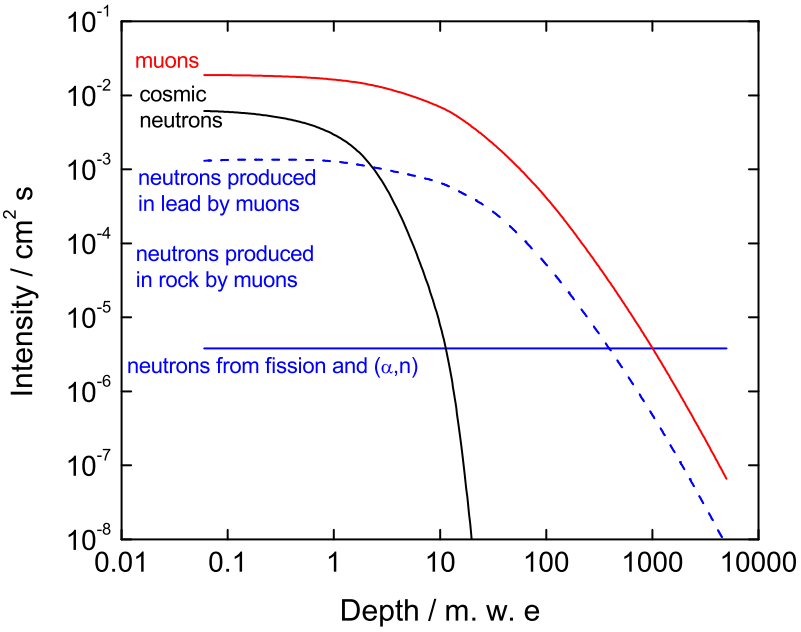

Figure 4.3: Dependance of intensity of muons and neutrons on depth. Adopted from [62] and extended with equations from [69]. The neutron background rate from (α,n) reactions at Gran Sasso [67, 68] is also included.

intense but harder (higher in average energy) when going deep underground [53, Chapter 4]. In fig. 4.3 behavior of the intensity of different components of cosmic rays is shown. Just the hard component and secondary neutrons caused by it survive more than 15 m of water equivalent (m.w.e) depth. As it is shown the muons can survive huge depths, it leads also to the presence of muon induced neutrons. Until a certain depth – depending on the composition of the laboratory walls and the surrounding rock [66] – these neutrons dominate the neutron background, which can not be suppressed with a veto detector as mentioned before. Considering the typical (α,n) neutron rate at Gran Sasso laboratory [67, 68] (further details of this deep underground laboratory can be found in sec. 5.2.3), these neutrons starting to dominate below 600 m.w.e. Therefore, the typical proposed underground laboratories for nuclear astrophysics are more than 1000 m.w.e. depth [70, 71].

4.2.3 Shielding against neutrons

Neutrons do not have charge, so they lose energy only by scattering on nuclei. The best way to moderate them is using materials with low effective Z or a lot of hydrogen (like water, polyethylene or paraffin). Because of the similar mass of the involved particles, the neutron can lose almost its whole energy in one scattering. Subsequent capture on lithium, boron or cadmium may eliminate the neutrons. The first two are preferable, because they use the (n,α) reaction. Cd captures the neutrons with radiative capture followed by γ-quanta with 558 keV energy. Unfortunately the other captures are also followed by soft γ emission, therefore, the neutron capture should occur outside of the lead shield to attenuate the γ-radiation. Unfortunately, this means that neutrons produced inside the shield mainly survive.

A better way to reduce the flux of the neutrons is to shield the whole experimental area. It can be done by reducing natural neutron production. A good way to make this, is placing the experiment underground. At different depths the source of the main fraction of the neutrons is very different.

Energetic neutrons are coming directly from cosmic rays. These are attenuated to negligible level with a shield of around 15 m.w.e. [72]. At shallow underground (≈ 100 m.w.e.) the most probable source of the neutrons is knock out reactions by the energetic muons, or neutron emission as deexcitation after a muon capture. At deep underground (> 1000 m.w.e.) the muons are highly suppressed, therefore, muon-induced neutrons become negligible. At this depth the main source of the neutrons are spontaneous fission of uranium and thorium, and (α,n) reactions occurring in the rock. The ^{238}U and ^{232}Th decay chains are the sources of these α particles. The simplest way of eliminating this background source is to shield the U and Th containing walls with a neutron shielding material of sufficient thickness (at least 20 cm), or to put in cement depleted in uranium and thorium.

4.2.4 Avoiding radioactive contaminations

The typical contamination of the lead shield (^{210}Pb) was mentioned in sec. 4.1.4. It can be suppressed by using old lead – which was produced several half-lives of ^{210}Pb ago – as the internal part of the shield. However, the availability of such lead is limited, since it is produced from water pipes more than 200 years old, sunken shiploads, or ballast of sailing ships. Furthermore, the age of the lead is not enough, if uranium was not removed at the beginning of lead production, then ^{210}Pb is in secular equilibrium with the uranium decay series.

Other possibility is using old iron plates or rods, but it always has to be tested, to avoid possible ^{137}Cs contaminations (from the atmospheric nuclear weapon tests), or ^{60}Co (usual contamination during the production of steel in a furnace).

Electrolytic copper is less likely to be contaminated, because the redox potential is generally an important factor influencing the degree of radiopurity that can be achieved. However, it is much more expensive and attenuates the γ-radiation less then the above mentioned materials. The other problem is that Cu has a high cross section for capture of thermal neutrons and for cosmogenic production of radioactive nuclei. It is also inferior to higher Z material such as Pb in the interaction with cosmic ray muons.

4.2.5 Shielding against radon

Daughters of radon are solids, which can be attached to aerosols, the internal side of the shielding, or directly to the detector endcap. The contaminated surface should be cleaned by acid, during the build up of the shielding. To prevent further contamination, the most common way to remove radon from the detector is the so called radon box. This is usually a plastic box surrounding the whole shielding, flushed with nitrogen gas. The slightly overpressured nitrogen prevents the air (and its radon content) to reach the internal part of the shielding. More sophisticated systems use shield cavities that can be evacuated and filled with radon-free gas, e.g. nitrogen or old air [73]. Plastic materials should not be placed inside the shield as their surfaces draw radon progenitors by electrostatic attraction. Radon outside of the box is less problematic, because the lead shield is suppressing its radiation.

4.2.6 Attenuate X-rays and bremsstrahlung

To attenuate X-rays and bremsstrahlung a special lining can be used on the inner side of the lead shield. This should consist of materials with decreasing atomic numbers from outside to inside. Each material captures the X-ray of the outer neighbor, and radiates its own which have lower energy and lower intensity, at least because of the isotropic angular distribution. Therefore, smaller fraction of the radiation is penetrating towards the detector. After the closest material, the detector would not be sensitive enough to count the radiation, or simply the lower cut of the spectra should be set above the lowest X-ray energy. For example cadmium, copper and aluminium (from outside to inside) can be used. The cadmium is also suited to suppress the neutron background. The production mechanism and the suppression techniques of the neutrons are described in sec. 4.2.3.

Chapter 5

Background studies

In this section I introduce my own measurements which concentrate on the high energy background in a γ-detector, and its reduction. This energy region is important for many in-beam experiments for nuclear astrophysics. I combined two shielding methods, the underground location, and the active shielding with a veto detector. The goal of my investigations was to check how low the laboratory background can be in a shallow underground laboratory, and find out whether it is suited for accelerator based nuclear astrophysics studies. Until my work only deep underground sites were considered as suitable sites for these kind of studies. The background measurements were performed at different underground locations, both shallow and deep underground. Several spectra were taken at Earth's surface as comparison, and also to test the efficiency of the veto detectors.

5.1 Detectors used

Several detectors were used in all examined laboratories. Two of them had active shields, the others were used to compare the effect of the depth.

5.1.1 NaI

One of the scintillators used for the studies is a long box-shaped sodium iodide (NaI) detector, 43 cm long with a square area of 10.5 cm · 10.5 cm. The spectra were taken in horizontal geometry, and no active shield was applied for this detector.

5.1.2 60 % HPGe

The other detector without active shielding is a p-type coaxial HPGe detector of 60 % relative efficiency[4]. The crystal is 60 mm long and has a diameter of 71 mm. The detector was used in vertical geometry. This detector was not transported to the deep underground site, but for comparison spectra were taken at Earth's surface and at shallow underground with dynamic range up to 80 MeV.

5.1.3 HPGe Clover

The first actively vetoed detector used in our studies is the Clover detector [74] of ATOMKI. It consists of four coaxial n-type HPGe detectors arranged like a four-leaf clover (fig. 5.1). Each crystal is 70 mm long and has a tapered circular area of originally 50 mm diameter; they are supplied with a common high voltage on the inner contacts and are mounted in the same cryostat. The spacing between the crystals is only 0.2 mm, leading to a closely packed geometry. A single crystal has 20 % relative efficiency. The analog signals can be summed leading to a virtual large detector of 122 % relative efficiency (add-back mode) [75]. This is more than four times one crystal efficiency,

[4] compared to a 76 mm in diameter and 76 mm long cylindrical NaI crystal, for the 1.33MeV ^{60}Co photo-peak, at a source-detector distance of 25 cm in the symmetry axis of the cylinder [32, Chapter 12].

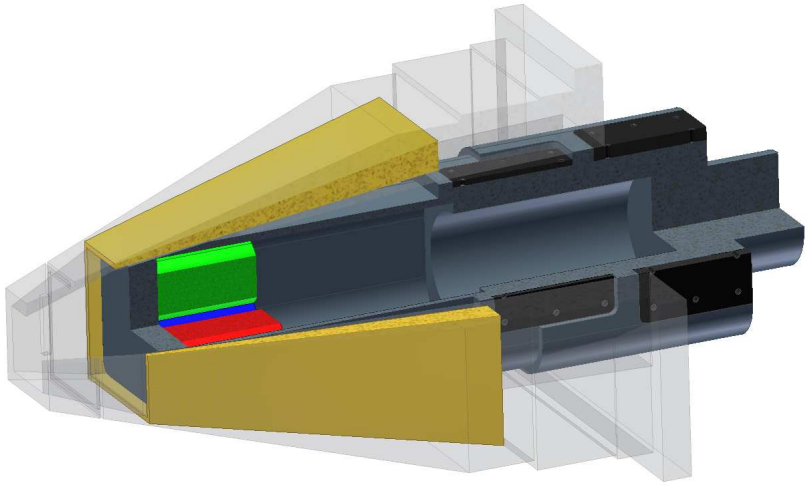

Figure 5.1: Schematic view of the Clover-BGO system. Three crystals (green, blue, red) and the BGO escape-suppression shield (yellow) are shown, the fourth crystal is left out from the figure for clarity.

because of such γ-rays which produce a signal in more than one detector (e.g. Compton scattering in one crystal and secondary γ-ray absorbed by the neighboring one). In the add-back spectrum these events produce one count in the full energy peak, instead of Compton events in a single crystal. The sum of the active volume of all four crystals is $470\,\mathrm{cm}^3$. This kind of summing can be done just with n-type detectors, because they have much thinner (few tenths of a micrometer) dead layers than normal p-type detectors (several hundred micrometers). The disadvantage of the n-type detector is the high production price, because the p-contact is made by ion implantation, and in case of n-type detectors it is much bigger (since it is on the outer surface of the crystal). Nowadays, special p-type detectors with thin entrance window exist (e.g. Canberra Extended Range Coaxial Ge Detector /XtRa/), but composite detectors still can not be produced from them.

In our studies the Clover was additionally equipped with a surrounding

bismuth germanate (BGO) scintillator. It is 24 cm long, has a truncated pyramidal shape, and at its front end there is a "heavy met" collimator. This alloy consists of tungsten ($> 90\,\%$), nickel and copper. The collimator is used in case of in-beam measurements to avoid a direct hit of the BGO by the γ-rays from the target. In my studies it has no particular importance, because the laboratory background γ-rays are not coming from one defined direction. The BGO has high density ($7.13\,\mathrm{g/cm^3}$), therefore, it always acts as a passive shield, and with anticoincidence electronics, it can be used as a Compton suppression veto. The BGO material contains radioactive ^{207}Bi, whose γ-lines are visible in the recorded laboratory background spectra. This contamination does not disturb the high energy region, I concentrate on. For comparing background studies, the detector system was used in horizontal geometry, so the BGO shield can act as a veto against penetrating muons passing the germanium detector volume.

The electronic chain of the signal processing system is shown in fig. 5.2. Signals from the four individual crystals are split after the preamplifiers. One part is fed into four main amplifiers, and the signals are then digitized and recorded in selftriggered, histogramming mode. These four individual histograms were gainmatched and added channel by channel, to form just one histogram. This histogram has typically 2.5 keV resolution at 1.33 MeV.

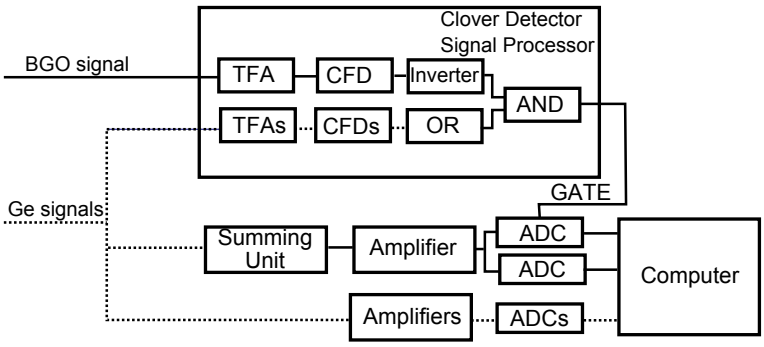

Figure 5.2: Box view of the signal processing chain of the Clover-BGO system. Four independent signal lines are marked by dashed line.

It helps to identify the peaks and multiplets, but was not used in this work in the further analysis.

The second part of the signals are fed into an analog summing unit implementing the gain-matching and summing of the four signals. The analog sum signal is then passed to a fifth main amplifier and digitized. The signal can then be recorded either in free-running, self-triggered mode, or in anti-coincidence with the signal from the BGO escape suppression shield. In this case the typical resolution was 8 keV at 1.33 MeV, but this bad resolution is compensated by higher efficiency, and for checking – e.g. whether a peak doublet appears – we had the individual spectra with 2.5 keV resolution. For producing the gate signal, the so called Clover detector signal processor unit (made by the ATOMKI electronic department) was used. It consists of timing filter amplifiers (TFA), and constant fraction discriminators (CFD) selected and adjusted to the time characteristics of this particular Clover-BGO system.

5.1.4 $LaBr_3$

Another actively shielded detector used in our studies is a lanthanum bromide ($LaBr_3$) scintillation detector. In recent years, $LaBr_3$ detectors have become increasingly popular due to their higher intrinsic efficiency and better energy resolution when compared with NaI detectors. The disadvantage is a significant contamination from ^{138}La ($t_{1/2} = 1.02\,1 \cdot 10^{11}$ y [76]) that is intrinsic in the detector material, preventing low-countrate applications at least for low-energy γ-rays. Because this isotope is intrinsic in the active volume, the 1436 keV γ-ray following the decay of ^{138}La is summed up with the Ba X-ray from the daughter nuclide, and a peak appears at 1468 keV with a shoulder peak at 1436 keV (fig. 5.3). This structure buries the natural ^{40}K line at 1461 keV. Bremsstrahlung continuum is also summed up with the 789 keV γ-line. Quenched α-lines of actinium series contaminants in the crystal are also detectable [77]. This point, however, is less of a concern when high-energy γ-rays from a nuclear reaction are to be detected.

In order to study the effect of the depth and the active shielding on the cosmic ray induced events with a completely different setup, a cylindrical

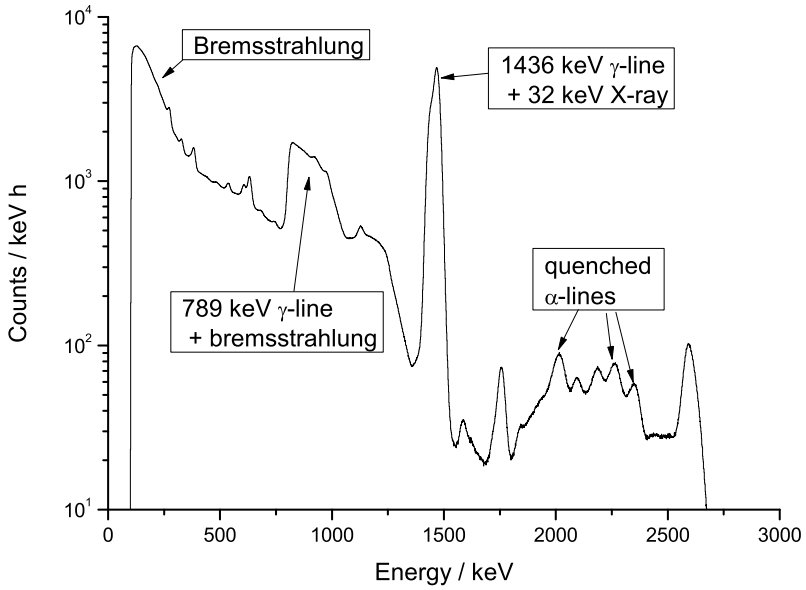

Figure 5.3: γ-spectrum recorded by the $LaBr_3$ detector. The marked features are the intrinsic activity of $LaBr_3$. Rest of the peaks are from the laboratory background.

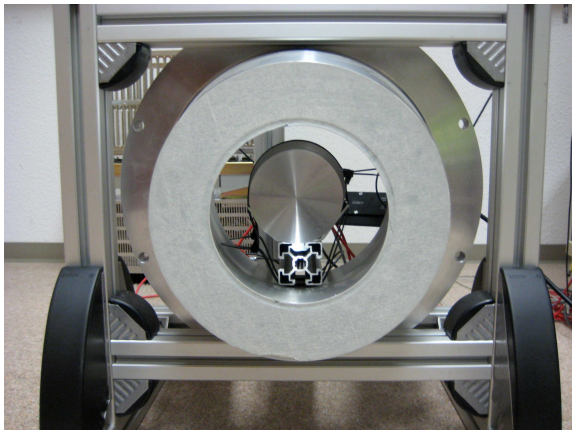

Figure 5.4: Photo of the $LaBr_3$ placed in the large BGO shield.

$LaBr_3$ of 7.6 cm length, 7.6 cm diameter, and 350 cm^3 volume was inserted in the center of a large BGO anticompton shield of 23 cm length and 13 cm internal diameter, that was originally designed to host a Cluster detector (fig. 5.4). Since it was much longer than the $LaBr_3$, the BGO shield formed a muon veto.

The detector pair was transported to the same sites as the Clover-BGO, and background spectra were recorded. The active shield was not transported deep underground, because no more reduction in the cosmic ray continuum was expected (see sec. 5.4). The signal processing system is similar, except in the $LaBr_3$ case, there is no need to have a gain matching.

5.2 Sites studied

Measurements were performed at laboratories with different depth to test the effect of the rock shield, and also to test the efficiency of the veto detector on the remaining cosmic radiation. In the following the different sites are described.

5.2.1 Earth's surface

Surface measurements which are presented here in the Clover case were performed both at ATOMKI[5], on the ground level in a one storey building, and at Helmholtz-Zentrum Dresden-Rossendorf (HZDR)[6], in the basement of a three-storey building. In case of the other detectors surface spectra were taken only at HZDR. Different ceiling thickness had no effect in the high energy region, as it was tested for the Clover (fig. 5.5). The spectra taken at the two surface locations were found to be consistent in the high energy region. In the low energy background region, there were different count rates observed, because of the different environmental radioactivity in the surrounding materials. This fact does not affect the conclusions, because my investigations concentrate on the high energy region.

[5] http://www.atomki.hu/
[6] http://www.hzdr.de/

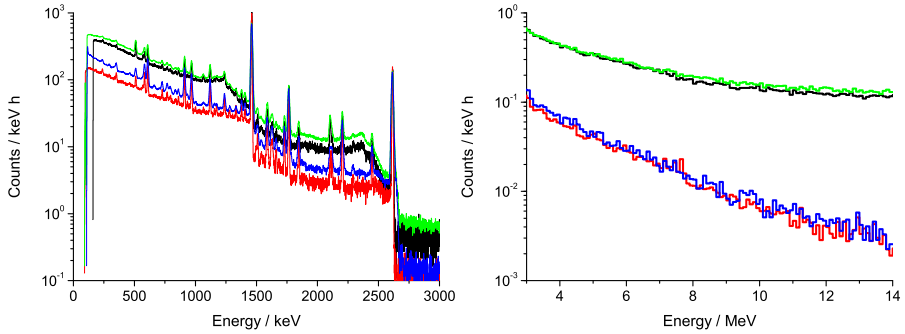

Figure 5.5: Laboratory background spectra taken at the two different surface locations with the Clover-BGO. Black curve HZDR with disabled veto, red line HZDR with active veto, green curve ATOMKI with disabled veto, blue ATOMKI with active veto. In the high energy region (right) there is no difference in the background rate at the two locations.

5.2.2 Shallow underground

The shallow underground study was performed in the Felsenkeller laboratory [78] in the Plauenscher Grund former quarry in Dresden. In the 1850's, a tunnel system was dug into the outside wall of a former quarry in order to make ice cellars for a nearby brewery. Since 1982, the Felsenkeller low-level counting facility is installed in one of the eight existing tunnels (fig. 5.6). The depth of the laboratory is 47 m, equivalent to 110 m of water.

The rock of the Felsenkeller hill consists of hornblende monzonite, with a relatively high ^{232}Th and ^{238}U content of 200 Bq/kg and 120 Bq/kg, respectively [79]. Fresh air is brought in from outside through a ventilation system, reducing the radon content in the underground facility to 40 Bq/m^3.

The low level counting facility consists of two laboratories, called hereafter MK1 and MK2, respectively, for Messkammer 1 and 2. MK1 dates from 1982 and is shielded by pre-1945 steel and serpentinite rock [80]. MK2 has been constructed in 1995 and has 25 cm thick walls of iron and steel, in part pre-1945 [79]. In addition, there is an unshielded workshop room underground.

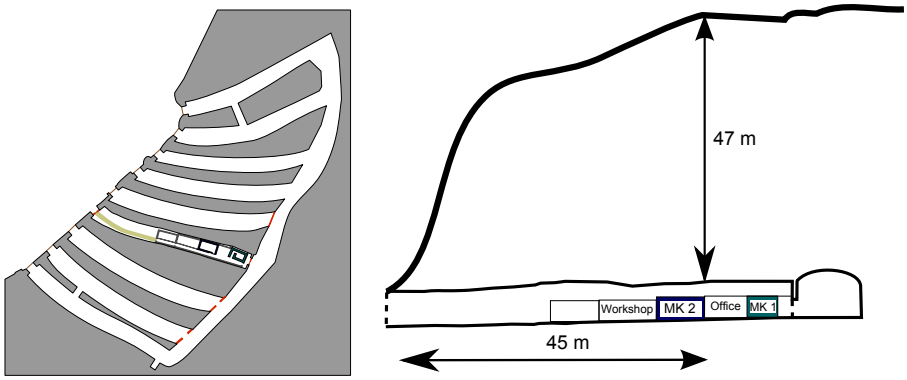

Figure 5.6: Plan view of the Felsenkeller tunnel system, and cross section of the rock hosting the low-activity laboratory.

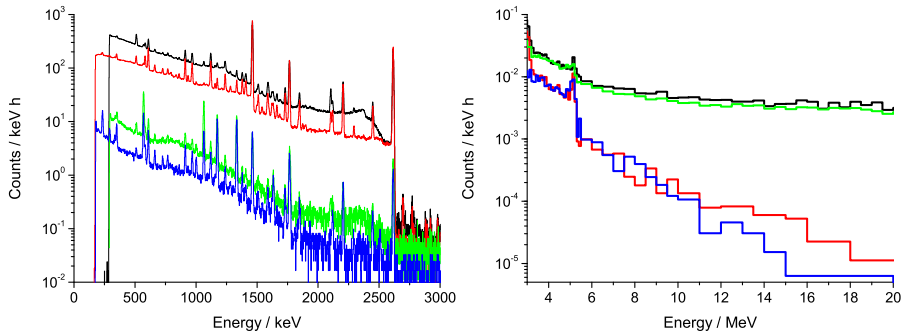

Figure 5.7: Laboratory background spectra taken in different rooms at Felsenkeller with the Clover-BGO. Black curve unshielded workshop room with disabled veto, red line: workshop with active veto, green curve: MK2 with disabled veto, blue: MK2 with active veto.

All of the Felsenkeller spectra used in the calculations were recorded in MK2. For comparison spectra were recorded in the non shielded workshop room, too. In the high energy region (which is our region of interest) a small difference is expected due to the different rock overburden (see fig. 5.6) which is thinner around 55° respect to the horizon at the position of MK2 [81], and the wall thickness of MK2 (≈ 2 m.w.e). Background rate difference was found consistent with the expectations (fig. 5.7).

5.2.3 Deep underground

Deep underground experiments have been performed at the underground facility of Laboratori Nazionali del Gran Sasso (LNGS)[7] (fig. 5.8) in Assergi, Italy. Excavation began in 1983 in conjunction with construction of the freeway tunnel crossing the Gran Sasso Mountain. The first large experiment started in 1989. At present the laboratory consists of three large experimental halls and service tunnels with a total volume of about 180 000 m^3. The whole facility is shielded from cosmic rays by a 1400 m thick dolomite rock overburden equivalent to 3800 m of water.

[7] http://www.lngs.infn.it/

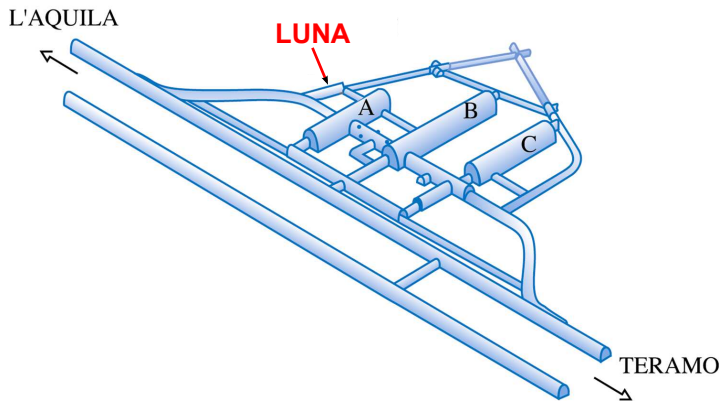

Figure 5.8: Schematic layout of the LNGS deep underground laboratory at the side of the highway.

LNGS is the only deep underground laboratory hosting an accelerator The accelerator facility is called Laboratory for Underground Nuclear Astrophysics (LUNA) [70]. Owing to this special opportunity the LUNA collaboration is pioneering in very low cross section measurements for nuclear astrophysics. The collaboration measured many reaction cross sections related to stellar hydrogen burning reactions directly at the solar Gamow energy or at lower energy than ever reached before [70]. Our Clover detector was used at LUNA for in-beam measurements [82–84] with astrophysical motivation. Between the runs, the laboratory background reported here was recorded. The dynamic range of the Clover was set up to 8 MeV for the purpose of the measurements.

5.3 Effect of the rock overburden

First, the effect of the rock overburden was studied with the mentioned detectors. In case of detectors equipped with active shield, the veto detectors were inactive during the measurements but not removed.

For the NaI detector, the laboratory background in the 10 – 15 MeV range is lower by a factor of 46 in Felsenkeller as compared to the Earth's surface (see fig. 5.9 and table 5.1). Consistent reduction factors were found for the two HPGe detectors. The slightly different reduction factors for the scintillators can be attributed to different detector types reacting differently to passing muons and to neutrons (table 5.1). At LNGS none of the counting had enough statistics in this energy region for the ratio calculation. (In NaI 6 counts, in $LaBr_3$ 3 counts were observed in the mentioned region.)

A second effect is apparent in both detectors, namely reduction in the counting rate for $E_\gamma < 2.7$ MeV in Felsenkeller MK2. This reduction is mainly due to the shielding offered by the thick and specially selected walls of MK2 against natural radionuclides which are present in the surrounding rock, and only in minor part to the muon flux reduction. At Earth's surface and at LNGS, rooms without specially shielded walls were used.

The effect of the passive shielding of the MK2 is clearly seen in all cases in the low energy background region, except for the $LaBr_3$. This detector's

Table 5.1: Reduction factors in the 10 – 15 MeV region due to depth, calculated from the spectra shown in fig. 5.9.

	Earth's surface/Felsenkeller
NaI	46.4 ± 0.9
60% HPGe	37.4 ± 1.4
$LaBr_3$	25.4 ± 1.0
Clover	36.2 ± 1.1

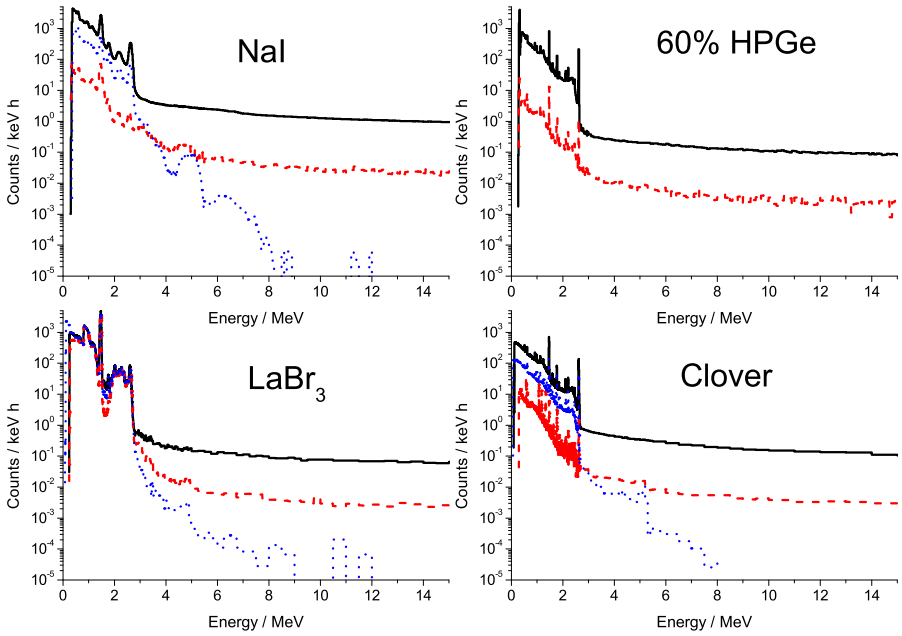

Figure 5.9: Counting rate in four different detectors without escape suppression at Earth's surface (black solid line), in Felsenkeller MK2 (red dashed line) and at LNGS (blue dotted line). There was no measurement at LNGS with the 60 % HPGe. In the Clover case at LUNA the spectrum was not recorded above 8 MeV. The continuum counting rate in the high energy region is decreasing with the depth.

background is dominated by intrinsic ^{138}La radioactivity at low energy, as mentioned before.

Owing to the lower counting rate in Felsenkeller and at LNGS, also some counts due to α-emitting contaminants can be discerned in the NaI detector, around 3.0 MeV and 4.5 MeV light-yield equivalent and in the Clover around 5.2 MeV. At the surface of the Earth, these contaminant lines are buried in the muon-induced background. Quenched α-lines are most probably due to uranium and thorium chain contaminations inside the crystal [85], or in the solder [60].

5.4 Effect of the active shield

The efficiency of the active shield to suppress the remaining muon continuum was tested with the Clover-BGO at each site. At LNGS there was no further reduction observed in the high energy region due to the active veto detector (fig. 5.10). This was expected, because at this depth the (n,γ) reactions dominate the high energy laboratory background [86], which cannot be suppressed by a veto detector.

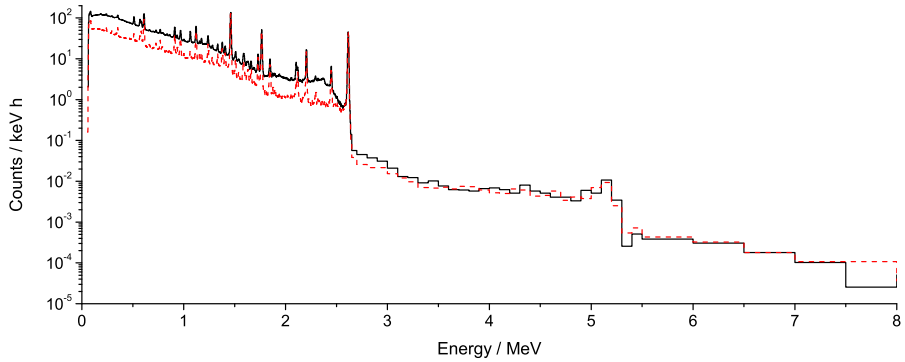

Figure 5.10: Free running (black solid line) and escape suppressed (red dashed line) spectra at LNGS recorded with the Clover-BGO. There is no difference in the high energy region.

It can be clearly seen in the figure, that the veto detector only acts as a Compton suppressor in this instance. In the low energy region, there is a factor of $2-3$ difference in the average counting rate. In the high energy region, there is no difference in the counting rate. As it was shown in sec. 4.2.2 the (α,n) neutrons dominate the background deep underground, therefore, the veto detector is not effective any more in the high energy region.

A strong reduction is observed due to the active shield at Earth's surface and at shallow underground. In fig. 5.11 the measured spectra are presented. It is clearly seen in table 5.2, that the reduction factor is increasing with the depth, and also increasing in the higher energy region.

The increasing efficiency of the veto detector while going underground can be attributed to the changing muon energy spectrum and angular distribution. The muon spectrum becomes harder at an underground location as mentioned in sec. 4.1.2. The muons with higher energy would give signal in the veto detector with higher probability, therefore can be vetoed with higher efficiency. The muon signal in the detector mostly depends on the muon track length in the active volume (see sec. 4.1.2). For higher energy signals, the muons should penetrate more active material, thus the track should be more parallel to the crystal sides. In this case the muon has higher probability to go through the veto detector, too. This can be the reason of the increasing veto efficiency with the increasing energy.

In the Clover-BGO system, the reduction is stronger, because this BGO was designed to the Clover, and acts much more effectively, than that of the $LaBr_3$. As it was mentioned the BGO of the $LaBr_3$ was designed originally to host a Cluster detector, with much larger diameter.

Table 5.2: Reduction factor due to the active shield at different sites in different energy ranges calculated from spectra shown in fig. 5.11.

	10 – 15 MeV	15 – 20 MeV	20 – 30 MeV
Clover, Earth's surface	31.4 ± 0.8	71 ± 3	133 ± 6
Clover, Felsenkeller	76 ± 11	368 ± 117	N/A
$LaBr_3$, Earth's surface	20 ± 1	35 ± 3	42 ± 3
$LaBr_3$, Felsenkeller	24 ± 4	53 ± 15	45 ± 8

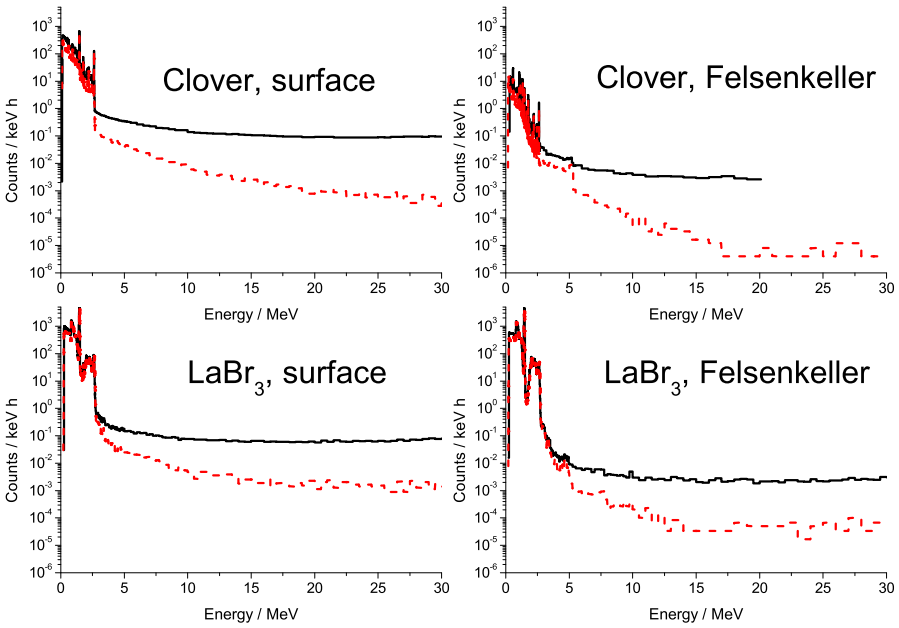

Figure 5.11: Effect of the active shield at different sites. Black solid lines show free running spectra, red dashed lines the vetoed spectra. Free running Clover spectrum was recorded at Felsenkeller only up to 20 MeV. The active shield reduces the continuum background through the whole spectra, but it is more effective in the high energy region (see table 5.2).

5.5 Muon peak

As it was mentioned in sec. 4.1.2, the passing muons form a peak in the high energy part of the spectra. I checked the muon peak in the 60 % HPGe and in the Clover-BGO spectra. The effects of the depth and the active shield on the muon peak were studied.

Depth

To test the effect of the depth on the muon peak, spectra were recorded with the 60 % HPGe with a dynamic range up to 80 MeV in vertical orientation at Earth's surface and at Felsenkeller (fig. 5.12).

The muon peak is visible in the spectra at 45 MeV. This energy corresponds to the most probable muon track length of 6.1 cm, taking into account that the muons lose about 7.3 MeV/cm in germanium by ionization [50]. The value is in good agreement with the 6 cm length of the crystal. Choosing the region of interest between 30 and 70 MeV the reduction factor due to the depth is 31, consistent with the expected muon flux reduction in Felsenkeller.

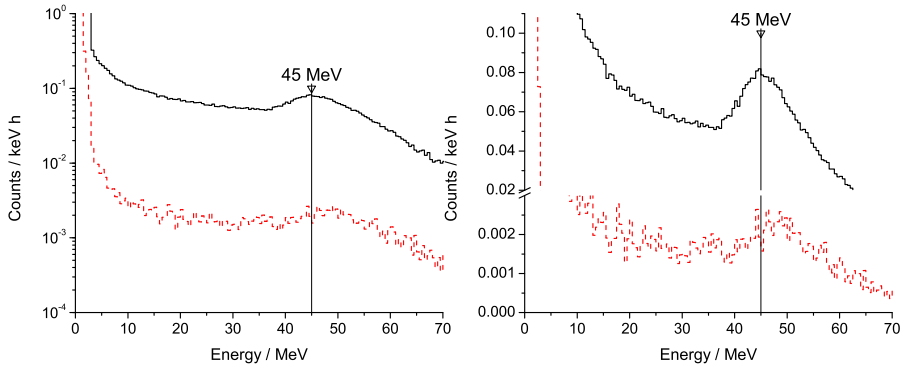

Figure 5.12: Spectra with high dynamic range recorded at the Earth's surface (black solid line) and Felsenkeller (red dashed line) with the 60 % HPGe detector. The same spectra are shown with logarithmic (left) and linear (right) scaled axis. An arrow shows the muon peak.

Active shield

To test the efficiency of the active shield spectra with a dynamic range up to 70 MeV were recorded with the Clover-BGO in horizontal and also in vertical orientation at Earth's surface (fig. 5.13).

One can clearly see the muon peaks in the spectra. In vertical orientation, it is apparent at 52 MeV both in the escape-suppressed and in the free-running spectrum, meaning a most probable muon track length of 7 cm. This is in excellent agreement with the 7 cm length of the crystals.

In horizontal geometry, in the escape suppressed spectrum the peak appears also around 52 MeV. This proves that the active shield is so effective, that less vertically coming muons can make signal in the detector than horizontally arrived, regardless of the $\cos^2\theta$ angle distribution of the incoming muons. In horizontal orientation, a structure is visible in the free-running spectrum. There are two bumps, one at 30 MeV, the other at 59 MeV,

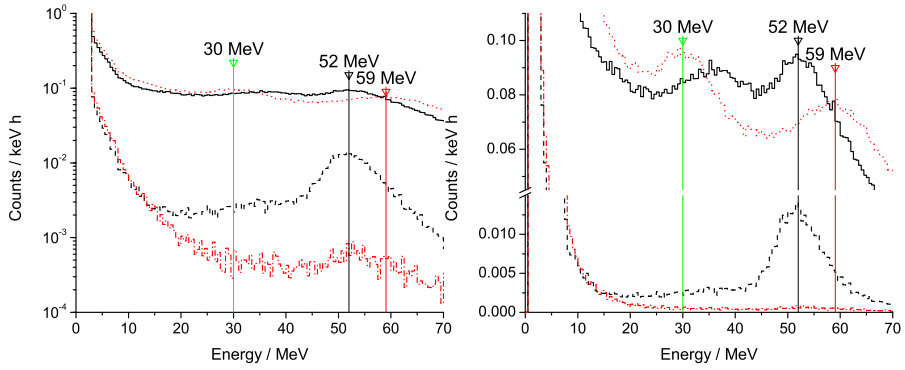

Figure 5.13: Spectra with high dynamic range recorded at the Earth's surface with the Clover-BGO system: Downlooking vertical orientation, free running (black full line) and with active veto (black dashed line). Horizontal orientation, free running (red dotted line) and with active veto (red dot-dashed line). The same spectra are shown with logarithmic (left) and linear (right) scaled axis. Arrows show the muon peaks.

corresponding to 4 cm and 8 cm muon track length. The values are in fair agreement with the 4.5 cm average width of a single crystal and the overall width of 9 cm of the four-crystal assembly, respectively.

In vertical orientation, the BGO shield reduces the counting rate between 30 – 70 MeV by a factor of 15, despite the fact that the zenith direction is not covered in this geometry. This can be explained by the angular distribution of the muon flux, and the relatively small opening angle left uncovered by the rather long BGO shield (fig. 5.1).

In horizontal orientation, there is a factor of 160 reduction in 30 – 70 MeV counting rate by the BGO anticoincidence. This improvement is due to the relatively low muon flux incident at near horizontal angles.

5.6 Combination of active and passive shielding

The combination of the two shielding methods shallow underground is now studied. In fig. 5.14 it is shown, that the actively shielded spectrum at shallow underground is only a factor of 2.5 higher than that at deep underground. Shallow underground laboratories also offer satisfactory background conditions, if a suitable active shield is applied, surrounding either just the detector or the whole laboratory suppresses remaining muons. This finding opens the way to consider shallow underground laboratories also as a possible site for in-beam cross section measurements of astrophysical interest, alongside the deep underground ones.

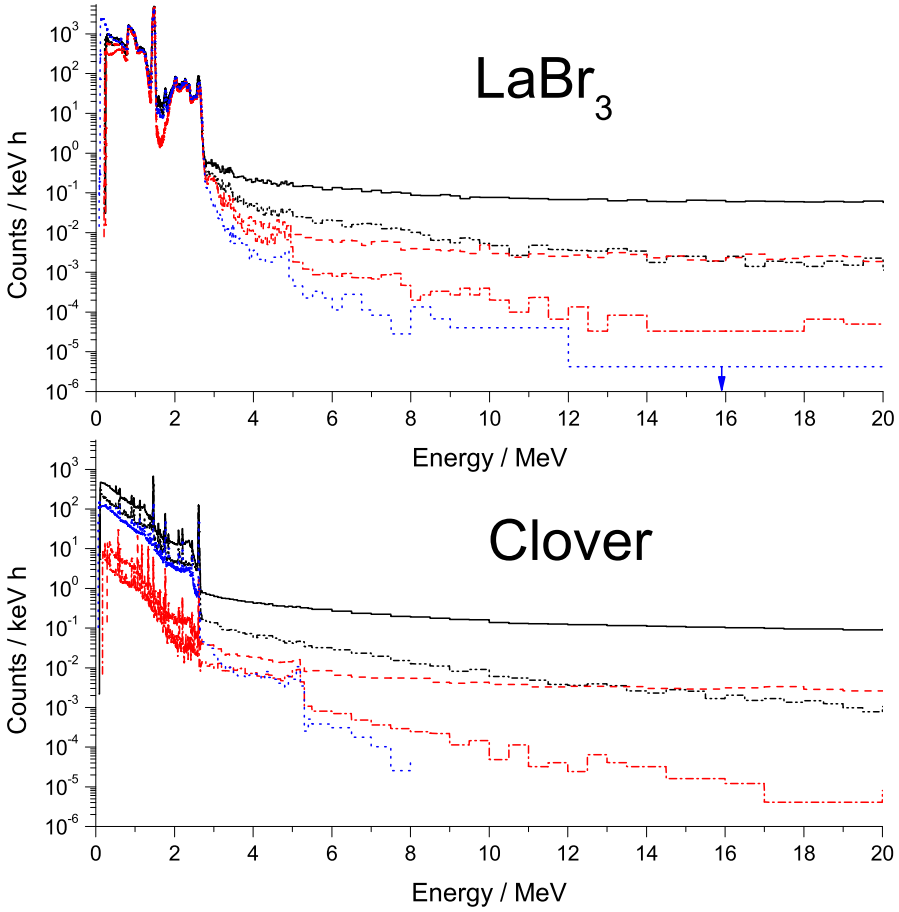

Figure 5.14: γ-background recorded by the actively shielded detectors: Earth's surface, without (black solid line) and with (black dot-dot-dashed line) active veto. Shallow underground, without (red dashed line) and with (red dot-dashed line) active veto. Deep underground without active veto (blue dotted line). Clover spectrum at LNGS ended at 8 MeV. In $LaBr_3$ spectra at LNGS above 12 MeV upper limit is given.

5.7 Feasibility of in-beam reaction cross section measurements

In recent years, underground nuclear astrophysics experiments have helped put the understanding of nuclear fusion in our Sun on firm experimental ground [87].

After hydrogen burning, helium burning ensues. The relevant reactions of helium burning are still not understood on a sufficient level of precision [88]. This applies e.g. to the $^{12}C(\alpha,\gamma)^{16}O$, $^{16}O(\alpha,\gamma)^{20}Ne$, $^{18}O(\alpha,\gamma)^{22}Ne$ reactions. The first two proceed mainly through direct capture (DC) at astrophysically important energies ($\sim 300\,\mathrm{keV}$), which is at present not accessible experimentally. In massive stars these reaction rates together with the triple-α reaction determine the ^{16}O abundance at the ignition of the carbon burning phase in late stellar evolution. This abundance in turn, strongly influences the subsequent hydrostatic burning stages, thus affecting the pre-supernova stellar structure, the explosive nucleosynthesis, and the nature of the remnant [89]. The end product of the third reaction, ^{22}Ne is very important for the slow neutron capture process, because $^{22}Ne(\alpha,n)$ is one of the neutron source reactions supplying the neutrons for the *s*-process. The $^{18}O(\alpha,\gamma)^{22}Ne$ reaction proceeds via resonant capture (Res), but the relevant resonance strengths are not well known experimentally.

Table 5.3 is summarising the existing experimental data on the mentioned reactions. The measured points are far above the Gamow window, and have big uncertainty. In this section the possibility to measure these reactions at an underground location is discussed.

To see the opportunities in the combination of the two shielding methods, a feasibility study of accelerator-based experiments is shown. Each mentioned reaction emits γ-rays of $E_\gamma \geq 3\,\mathrm{MeV}$, where γ-lines from environmental radionuclides do not play a role, and a lead shield is not expected to further improve the background. The feasibility of in-beam γ-spectroscopy experiments is discussed based on the Clover-BGO system used here. The detector endcap is considered to be at 9.5 cm distance from the targets, as it was already used for in-beam measurements at LUNA [82–84]. A typical

value of $6 \cdot 10^{17}$ active target atoms/cm^2 is assumed, with the composition given in table 5.4. For the fixed-energy γ-ray from the ^{18}O(α,γ)^{22}Ne reaction, the width of the γ-ray region of interest (ROI) is taken as two times the full width at half maximum (FWHM) γ-energy resolution. For the other cases, the ROI widths were determined from the energetic target thickness, folded with the resolution. The S-factor or resonance strength and branching ratio are adopted from the given reference (table 5.4). A beam intensity of 250 particle-μA is assumed.

It should be noted that the given background levels are lower limits, neglecting ion beam induced background. However, this latter problem usually did not limit experiments at LUNA. In principle, an experiment is also possible when the signal is much lower than the background. However, the time required to reach a given statistics scales with the ratio of background to signal. The running times in months to reach 10 % statistical uncertainty, assuming full availability of the accelerator for the type of experiment discussed here in table 5.4 has been computed according to eq. 2.17, and are shown in table 5.5. It is clearly seen that an experiment cannot be performed in a realistic time with these counting rates when the background is much higher than the signal. As a rule of thumb the signal counting rate should be higher than or at least comparable to the background in order to find experiments to be feasible.

When adopting this criterion, it is apparent that for the two reactions proceeding through mainly DC, an experiment at the surface of Earth is impossible. For the ^{18}O(α,γ)^{22}Ne reaction, recent experiments at Earth's surface were still limited by background [91].

For all the cases studied here, already the shallow underground location offers a background that is a factor of 25 – 55 lower than at Earth's surface, sufficiently low so that experiments are feasible. Deep underground, the background is even lower than shallow underground by a factor of 2 – 2.5. It is also clearly seen, that shallow underground site gives reasonable measuring time, close to the deep underground ones.

Table 5.3: Experimental data on the three reactions of helium burning used in the feasibility calculation. Gamow windows at 0.15 GK are given. In DC cases the uncertainty is the error of the measured S-factor, in case of resonance the error of the resonance strength.

Reaction	Ref.	Main reaction mechanism	GW / keV (T = 0.15 GK)	Lowest meas. point $E_{C.M.}$ / keV	Uncertainty
$^{12}C(\alpha,\gamma)^{16}O$	[88]	DC	190–330	940	> 75 %
$^{16}O(\alpha,\gamma)^{20}Ne$	[90]	DC	250–400	1200	upper limit
$^{18}O(\alpha,\gamma)^{22}Ne$	[91]	Res	250–400	385	33 %

Table 5.4: Signal counting rate for capture to the ground state of the final nucleus, at the astrophysically relevant center-of-mass energy E. Adopted S-factors or resonance strength from the given references are also shown. For ^{12}C in Au, an atom number ratio of 5:1 [92] is assumed. Background counting rate at different depths with active veto is given.

Reaction	$E_{C.M.}$ / keV	Adopted S-fac. or $\omega\gamma$	Ref.	γ-ray ROI / keV	Target	Full energy peak efficiency of Clover
$^{12}C(\alpha,\gamma)^{16}O$	800	45 keV b	[88]	7929 – 7968	^{12}C in Au	$8.9 \cdot 10^{-4}$
$^{16}O(\alpha,\gamma)^{20}Ne$	1300	1900 keV b	[90]	5991 – 6035	Al_2O_3	$1.2 \cdot 10^{-3}$
$^{18}O(\alpha,\gamma)^{22}Ne$	385	0.48 μeV	[91]	10045 – 10058	$Al_2\ ^{18}O_3$	$6.7 \cdot 10^{-4}$

Reaction	Signal / h^{-1}	Laboratory background counting rate / h^{-1}		
		Earth's surface	Shallow underground	Deep underground
$^{12}C(\alpha,\gamma)^{16}O$	0.018	0.59 ± 0.05	0.024 ± 0.008	0.006 ± 0.004
$^{16}O(\alpha,\gamma)^{20}Ne$	0.025	1.39 ± 0.05	0.039 ± 0.007	0.021 ± 0.006
$^{18}O(\alpha,\gamma)^{22}Ne$	0.045	0.082 ± 0.005	0.0015 ± 0.0006	0.0006 ± 0.0004[a]

[a] Rescaled from the $LaBr_3$ background.

Table 5.5: Time required to reach 10 % statistical uncertainty with the Clover detector, based on the signal and background counting rates in table 5.4 computed with eq. 2.17.

Reaction	Required time / months			
	Earth's surface	Shallow undergr.	Deep undergr.	Without background
$^{12}C(\alpha,\gamma)^{16}O$	507 ± 42	28 ± 7	13 ± 8	7.6
$^{16}O(\alpha,\gamma)^{20}Ne$	615 ± 22	23 ± 3	15 ± 4	5.5
$^{18}O(\alpha,\gamma)^{22}Ne$	14.1 ± 0.7	3.25 ± 0.08	3.13 ± 0.05	3.0

5.8 Conclusions

Presently there is only one underground accelerator worldwide used for nuclear astrophysics studies (the LUNA 400 keV machine). The aim of my work was to check how much additional reduction can be reached in the laboratory background counting rate in the high energy region ($E_\gamma > 3$ MeV), if an active shield is applied in an underground settings. For this purpose I measured the laboratory background with the same Clover-BGO detector system at LNGS (deep underground), at Felsenkeller (shallow underground), and at ATOMKI (surface of Earth). Additionally, comparisons were done with other detectors as well.

It was shown, that although the active shield causes a big reduction in the high energy background at the surface of Earth, this reduction is still not sufficient, for many in-beam cross section measurements for nuclear astrophysics.

Deep underground, the active shield works only as a Compton-suppressor, because there the sources of the high energy background are not the muons any more, but neutrons from (α,n) reactions and/or fission. (Related publications from my publication list: Scientific paper: 1; Poster: 1.)

It was proven that the combination of a shallow underground location and an active shield offers satisfactory background conditions for a number of in-beam γ-spectrometry experiments, owing to the fact that nuclear reaction experiments require low but not ultra-low [94, e.g.] background. (Related publications from my publication list: Scientific paper: 4; Proceedings and other publication: 1, 2, 4; Talks: 1, 2; Posters: 2, 3, 4, 6.)

This finding opens a new way for a complementary approach to place our understanding of stellar nucleosynthesis on a firm experimental foundation. The easy access to shallow underground facilities and standard detectors should be exploited to quickly gain low-energy data near the Gamow peak, while large detector arrays at deep underground sites push the data limit even lower, in some cases to astrophysical energies.

Based on my measurements, a plan of an accelerator facility in the Felsenkeller tunnel system was born. As a consequence a workshop on underground accelerators for nuclear astrophysics was held in Dresden [95],

and this plan was supported by the scientific community. The possible underground accelerator facility was also supported at two follow up workshops [96, 97], and was discussed at several conferences [98, 99].

Chapter 6

X-ray counting to determine nuclear cross sections

In the previous section the background reduction was studied. The other way to get higher sensitivity is the signal enhancement. Some of the quantities mentioned in sec. 3.2 can be enhanced by detection of characteristic X-rays following the decay of a nucleus.

In heavy mass region radioactive isotopes on the proton rich side of the valley of stability decay totally or partially by electron capture. After electron capture a vacancy is produced most probably at inner atomic shell, since it has the biggest overlap with the nucleus. This vacancy will be filled by an electron from the outer shells. The process is dominantly followed by X-ray emission. X-rays can also be produced after the nucleus de-excitation by internal conversion. The goal is to detect this radiation to measure the activity, instead of counting γ-rays.

X-ray detection has many advantages. Usually X-rays have higher branching than γ-rays, (if those exist at all) since X-ray emission is an atomic process. The energy of the X-rays is below 100 keV where most of the detectors have the highest efficiency.

Unfortunately there are disadvantages, too, which are limiting the applicability of the method. The X-ray counting is not able to distinguish

between the decay of the different isotopes of the same element. If both the (α,n) and (α,γ) channels are open (which is very often the case for heavy p-isotopes in possibly investigated energy range), then two isotopes of the same element are produced. More than one isotope of the same element is inevitably produced if the target consists of more than one isotope, too.

Some way should be found to separate the produced isotopes. The different half-lives of the reaction products help. Following the decay-curve of the X-ray yield and fitting two (or more) exponentials, the activity of the two isotopes can be separated. If the products have extremely different half-lives there is no need to follow the decay-curve. X-ray counting can be carried out more than once. In every counting those isotopes produce predominantly the X-ray peak, which are still in the source, and did not decay out. With subtraction the number of active atoms can be derived. Other possibility is, if some of the reaction products have sufficiently high intensity γ-rays, combination of the X-ray and γ-counting can help the disentanglement. Activity of one isotope can be measured via γ-ray counting, and this can be subtracted from the activity derived from X-ray counting.

Other possible difficulty can be the X-ray self absorption in the target. If the resulted nucleus emits X-ray with higher energy than the K-edge of the target, increased self absorption in the target should be taken into account. In our studies the strongest X-rays (K_α) of the product nucleus is always lower in energy than the K-edge.

Usually for X-ray detection measurements (X-ray fluorescence (XRF), Proton Induced X-ray Emission (PIXE), etc.), lithium drifted silicon (Si(Li)) detectors are used. The resolution of them at typical X-ray energy of 5.9 keV is around 140 – 170 eV. X-ray escape peak of the silicon is 1.8 keV below the full energy peak, which complicates the spectra, because the typical energy difference of the X-ray peaks are also close to this value. Disadvantage of these detectors is the very fast dropping of the efficiency above 50 keV, and they are totally unusable above 100 keV [100].

To overcome this problem thin HPGe crystals started to be used. Improvements in fabrication processes reached the level, that these detectors are competitive in resolution with the Si(Li). The efficiency of HPGe does not drop so fast in the higher energy region, and X-ray escape peak of Ge

occurs 10 keV below the full energy peak, much easily distinguishable from the peak, and does not overlap with other close peaks.

6.1 Detectors

For the X-ray measurements a dedicated detector should be chosen. For this I compare two HPGe detectors available at ATOMKI.

100 % HPGe

The first detector is an n-type coaxial HPGe detector with 100 % relative efficiency. The high intrinsic efficiency and the carbon fiber entrance window is making this detector suited for measurement of radiation at both low and high energies. Recently, this detector was used for activation measurements for nuclear astrophysics by the ATOMKI group [49, 101].

LEGe

The other detector suited to low energy radiation counting is a low energy germanium detector (LEGe). This detector has a 15.5 mm thick HPGe crystal with 2000 mm^2 active area. The p-type front contact leads to just a few tenths of a micrometer dead layer. Entrance window is 0.5 mm thick beryllium, allowing us to take the full advantage of the low energy response of intrinsically thin window detector. The rear n contact is smaller than the full area of the crystal leading to smaller capacitance. Since preamplifier noise is a function of detector capacitance, this detector affords lower noise and consequently better resolution.

6.2 Sensitivity

To compare the two counting systems the efficiency in its own is not enough. For example the LEGe efficiency is less than that of the 100 % HPGe, but

it is more suited to count low energy radiation because of its background conditions and resolution.

The minimum detectable activity (MDA) [33, Chapter 5] is a good measure to compare different counting systems. It is inversely proportional to the detection efficiency (ϵ), and proportional to the square root of the background (B) times the full width at half maximum of the peaks (FWHM).

$$\mathrm{MDA} \propto \frac{\sqrt{B \cdot \mathrm{FWHM}}}{\epsilon} \tag{6.1}$$

The inverse of this equation is sometimes used as "figure-of-merit" for a counting system, because it is the square root of the traditional S^2/B criterion (sec. 2.5).

Eq. 6.1 is only valid if we consider only one region of interest under the peak (eq. 2.5), rather than the correct peak area (eq. 2.6), because that involves an other ROI to estimate the background. Using the exact equation results an MDA expression, where FWHM is not square rooted:

$$\mathrm{MDA} \propto \frac{\sqrt{B} \cdot \mathrm{FWHM}}{\epsilon} \tag{6.2}$$

For comparison, the ratio of two MDAs can be calculated as follows:

$$\frac{\mathrm{MDA}_1}{\mathrm{MDA}_2} = \sqrt{\frac{B_1}{B_2}} \cdot \frac{\epsilon_2}{\epsilon_1} \cdot \frac{\mathrm{FWHM}_1}{\mathrm{FWHM}_2} \tag{6.3}$$

In the following the different factors for the two mentioned detectors are discussed.

6.2.1 Laboratory background and shieldings

100 % HPGe

The 100 % HPGe is equipped with commercial 4π lead shield (10 cm) lined by 1 mm cadmium and 1 mm copper. This shielding causes a big reduction in the background counting rate (see fig. 6.1), because it suppresses the radiation from the natural long lived radioactive isotopes.

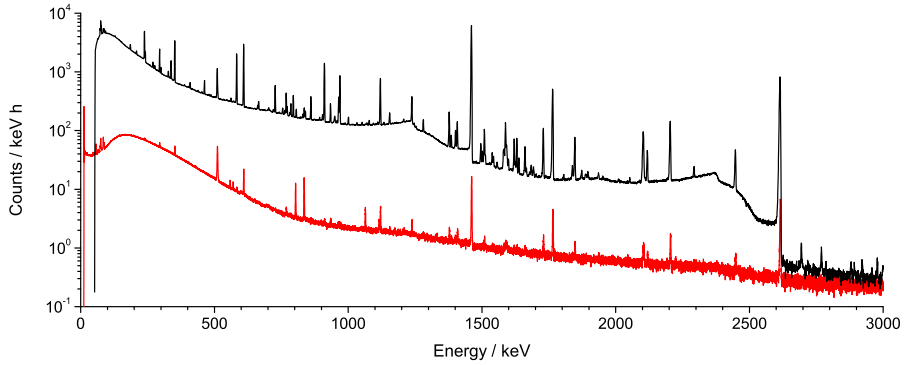

Figure 6.1: Measured laboratory background of the 100 % HPGe without (black curve) and with (red curve) the shielding. The lines and Compton continuum of ^{40}K, ^{208}Tl, and ^{214}Bi natural radioactive isotopes are highly suppressed.

LEGe

Because of the thin crystal the LEGe is naturally insensitive for the high energy γ radiations. In addition a graded shield was also applied to suppress environmental radioactivity. I designed a shield consisting of inner layers of 4 mm copper, 2 mm cadmium, 5 mm aluminium and an 8 cm thick outer lead shield which covers almost 4π. The aluminium is used only to hold the inner two, and has no importance in the background reduction. On the bottom of the shield the lead is just 1 cm thick, and there is a small opening at the neck of the detector where the cold finger is passing through. (see fig. 6.2).

In fig. 6.3 laboratory background spectra from the LEGe detector with different shieldings are shown. First the bare detector without any shielding, then only the lead is applied. As it was mentioned in sec. 4.1.6, lead shielding is good only in the higher energy region. It also applies to our case, as it is clearly seen in the figure, lead shield suppresses the background, but X-ray fluorescence becomes dominant. To overcome this problem a lining made of copper and cadmium was applied. The full shield causes a factor of about 70 reduction compared to the unshielded case around 50 keV.

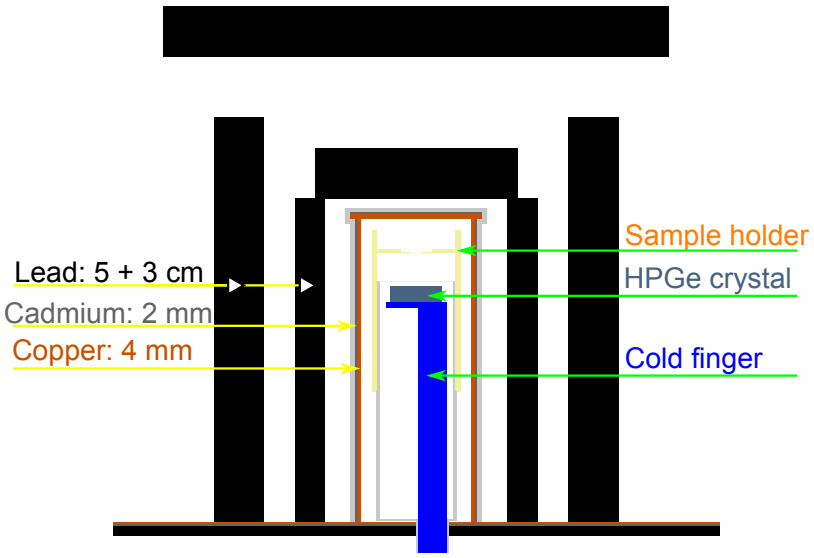

Figure 6.2: Schematic view of the home made shield of the LEGe detector.

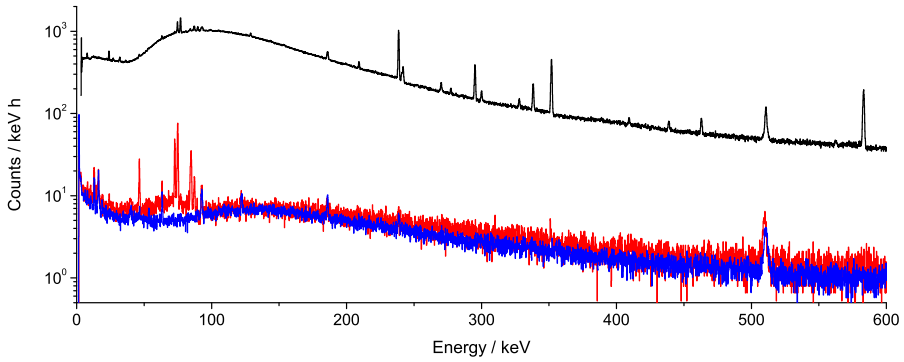

Figure 6.3: Measured laboratory background spectra of the LEGe detector, without shielding (black line), with 8 cm of lead without the lining (red line), and with the full shield (blue line). The reduction is about a factor of 70 in the energy region of X-rays.

6.2.2 Efficiencies

The detector efficiencies were measured using calibrated ^{57}Co, ^{133}Ba, ^{152}Eu, ^{241}Am ^{60}Co, ^{137}Cs, ^{54}Mn, ^{65}Zn, and ^{7}Be γ-sources. The absolute efficiency was measured at 10 cm source–detector distance.

In fig. 6.4 the absolute full energy peak efficiencies of the detectors are shown. Below 100 keV the efficiency difference is less than a factor of two. For the lowest energies the 100 % HPGe efficiency drops faster, because the absorption of the carbon fiber entrance window is higher than the absorption of the Be window. To the higher energy range the LEGe efficiency drops much faster because of the thin crystal can absorb much less γ-s with high energy.

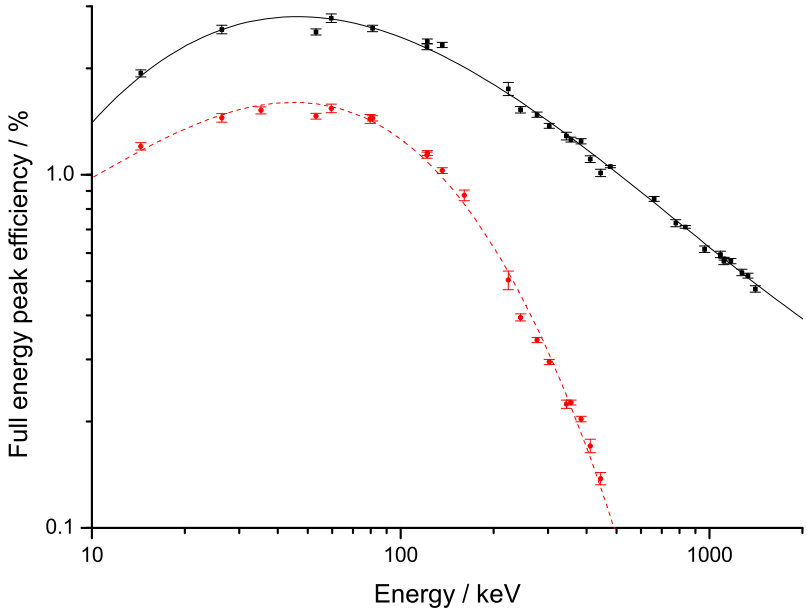

Figure 6.4: Measured absolute full energy peak efficiency at 10 cm source–detector distance. (Black squares: 100 % HPGe; Red dots: LEGe.) The points are fitted by third order logarithmic polynomials.

6.2.3 Calculated sensitivity ratio

The sensitivity calculation was done to compare the LEGe and 100 % HPGe detectors. The following ratio was calculated:

$$\frac{\mathrm{MDA_{HPGe}}}{\mathrm{MDA_{LEGe}}} = \sqrt{\frac{B_{\mathrm{HPGe}}}{B_{\mathrm{LEGe}}}} \cdot \frac{\epsilon_{\mathrm{LEGe}}}{\epsilon_{\mathrm{HPGe}}} \cdot \frac{\mathrm{FWHM_{HPGe}}}{\mathrm{FWHM_{LEGe}}} \tag{6.4}$$

The elements of the MDA ratio are shown in fig. 6.5. The x axes show the energy from 20 keV to 600 keV. The lower boundary was chosen, because below in the HPGe spectra noise appears, which can be misleading. The other boundary was set because of the LEGe efficiency drops very rapidly, and it makes no sense to expand further the measurements.

In case of background, a spline was fitted to the average continuum, regardless the peaks and it was used in the calculation. In addition to the background ratio, its square root is also shown with green line, because this is the quantity which is used in the calculation. It is around 3 in the X-ray region, slightly increasing up to 300 keV, but never higher than 5.

The fitted lines to the efficiencies are third order logarithmic polynomials. These fits were used in the calculation. In the X-ray region the ratio is always higher than 0.5, and only decreases below it above 100 keV.

The resolutions were fitted by square root of a second order polynomial [33, Chapter 6]. In the low energy region for the LEGe it is better than a factor of 2, and remains better up to 550 keV.

The calculated relative MDA (eq. 6.3) is shown in fig. 6.6. The sensitivity of the LEGe is more than a factor of 3 higher than that of the 100 % HPGe. The line crosses the one around 350 keV. This means now the LEGe is more suited even for γ-counting too, if the energy of the investigated radiation is below 350 keV. Therefore we used the LEGe detector for the X-ray counting, and consider it to use for low energy γ counting in the future.

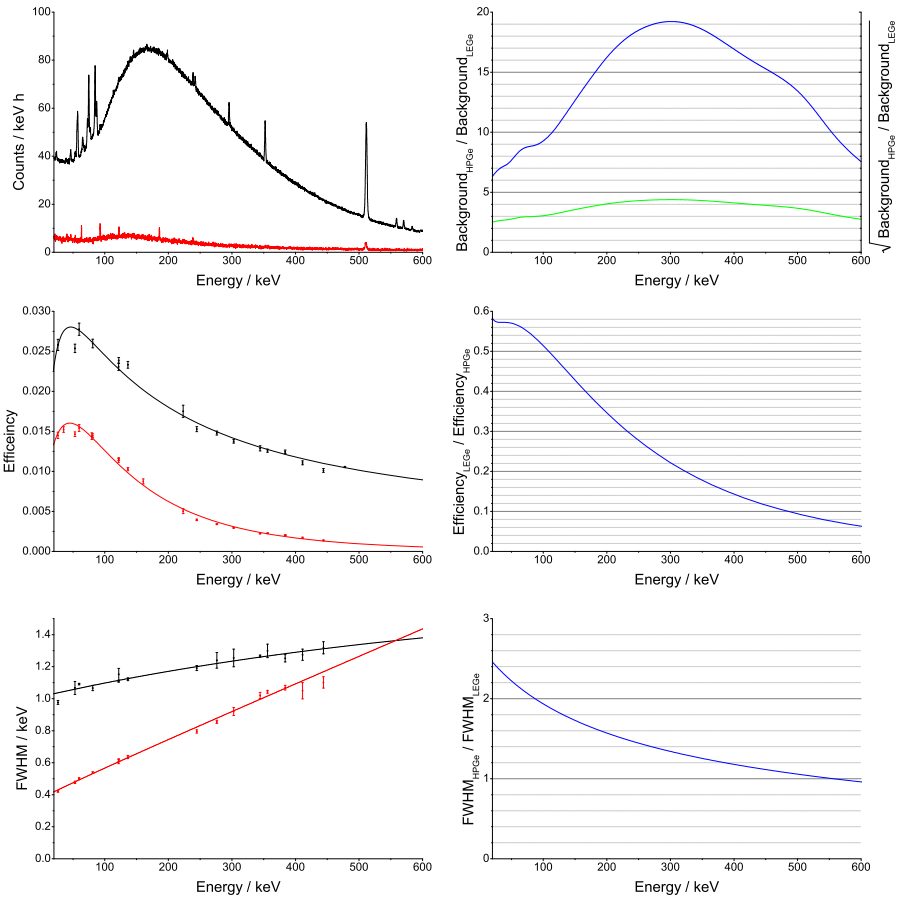

Figure 6.5: From up to down: Background, efficiency, FWHM. In first column always the measured quantities and fitted curves are presented. The ratio of the fitted values are in the second column. Black points and curves: measurements with the 100 % HPGe. Red points and curves: measurements with the LEGe. Blue curves are the ratios, green curve is the square root of the ratio. For details see text.

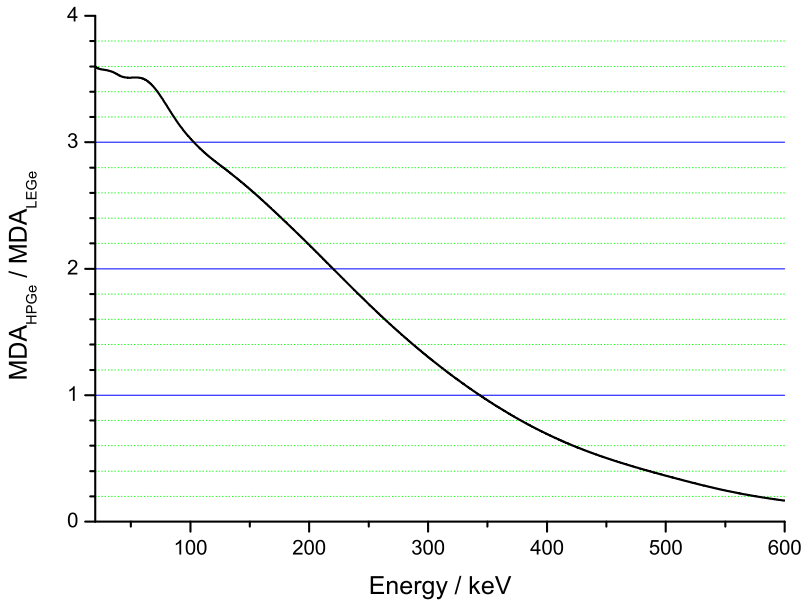

Figure 6.6: Sensitivity ratio of the 100 % HPGe and LEGe. The LEGe is more suited to count radiation with energy up to 350 keV.

6.3 α-induced reaction cross section measurement on ^{169}Tm

6.3.1 Investigated reactions

To demonstrate the applicability of the X-ray counting method I have chosen to measure α-induced reactions on ^{169}Tm at low bombarding energies. This reaction is well suited for the present study, and these data can be used to test and improve the theoretical cross section calculations for the astrophysical γ-process in this mass region, where no experimental data exist.

Gamow window for these reactions at a typical γ-process temperature of 2 – 3 GK is between 6.3 MeV and 10.7 MeV [31]. Thulium has only one

stable isotope (^{169}Tm), therefore enrichment is naturally guaranteed, and there is no need to take care on the reactions on other thulium isotopes. However, above $E_\alpha = 10.4\,\mathrm{MeV}$ the $^{169}\mathrm{Tm}(\alpha,\mathrm{n})^{172}\mathrm{Lu}$ channel is also open beside $^{169}\mathrm{Tm}(\alpha,\gamma)^{173}\mathrm{Lu}$, making separation of the two reaction products necessary. Decay parameters of the two reaction products are shown in table 6.1.

The half-life of ^{173}Lu is about 75 times longer than that of ^{172}Lu. Thus, separation can be done with the following procedure. The X-ray counting has to be carried out at least two times for each sample. Shortly after irradiation the decay spectrum is totally dominated by the decay of ^{172}Lu. The reason is the shorter half-life and higher cross section of the (α,n) channel, which above threshold becomes dominant, and exceeds by orders of magnitude that of the (α,γ) channel. In this case, X-rays belong dominantly to ^{172}Lu. Countings have to be repeated after many half-lives of ^{172}Lu, when its activity decreases to a negligible level and the measured X-ray yield belongs solely to the decay of ^{173}Lu. Thus, with two countings of the same target separated by a suitably long period, both cross sections can be determined from X-ray counting.

Table 6.1: Decay parameters of reaction products from (α,n) and (α,γ) reactions [102, 103].

Residual nucleus	Decay mode	Half-life/d	Energy/keV	Relative intensity per decay / %
^{172}Lu	ϵ 100 %	6.70 ± 0.03	51.35 (K_{α_2})	31.5 ± 0.9
			52.39 (K_{α_1})	54.9 ± 1.5
			810.06	16.6 ± 0.7
			900.72	29.8 ± 1.3
			912.08	15.3 ± 0.7
			1093.63	63.0 ± 3.0
^{173}Lu	ϵ 100 %	500 ± 4	51.35 (K_{α_2})	43.8 ± 1.4
			52.39 (K_{α_1})	76.3 ± 2.4
			272.11	21.2 ± 0.8

6.3.2 Target preparation

Targets were made by evaporating metallic thulium onto thin (2 μm) aluminium foils with the Leybold Univex 350 vacuum evaporator of ATOMKI. The foils were weighted before and after the evaporation and from the difference (assuming the evaporated layer is uniform) the number of target atoms was calculated. Thickness of targets varied between 100 and 380 μg/cm^2 (see table 6.2). To prove the uniformity, and to check the absolute number of target atoms, they were also determined by PIXE method [104] using the Nuclear Microbeam Facility of ATOMKI. A 2 MeV proton beam with a beam spot area of 3 μm $\times$ 3 μm provided by the Van de Graaff accelerator scanned over a surface of 500 μm $\times$ 500 μm at several different positions of the target. The precision of the determination of the number of target atoms was better than 3 %, and the thickness was found to be uniform within 2 %. The agreement between derived thicknesses from the two methods are within 4 %. A detailed list of the used targets is shown in table 6.2,

Table 6.2: Investigated energies, target thicknesses, used detectors in countings. Irradiations marked with * were carried out on two different targets.

E_α / MeV	Thickness / $\frac{\mu g}{cm^2}$	detector used for (α,n) channel	detector used for (α,γ) channel
11.5	346 ± 13	LEGe	–
11.85	353 ± 13	LEGe	–
12.2	326 ± 12	LEGe	–
12.5	294 ± 11	LEGe	–
12.6	377 ± 15	LEGe	LEGe
13.0	331 ± 13	LEGe	LEGe
13.5*	357 ± 13 & 167 ± 8	LEGe & 100% HPGe	LEGe & LNGS
14.0*	322 ± 12 & 225 ± 9	LEGe & 100% HPGe	LEGe
15.0*	356 ± 13 & 106 ± 4	LEGe & 40% HPGe	LEGe
15.5	225 ± 8	40% HPGe	LEGe
16.0*	305 ± 11 & 77 ± 3	LEGe & 40% HPGe	LEGe
16.5	232 ± 9	40% HPGe	LEGe
17.0	303 ± 11	LEGe & 40% HPGe	LEGe
17.5	185 ± 7	40% HPGe	LEGe & LNGS

where the weighted average of the derived thickness from the two different methods are shown. At lower energy irradiations thicker targets, at higher energy irradiations thinner targets were used.

6.3.3 Irradiations

The ^{169}Tm targets were irradiated with α beams from the MGC-20E cyclotron of ATOMKI. At the entrance of the activation chamber there is a tantalum collimator and a secondary electron suppressor with voltage of -300V. Rest of the chamber is insulated. Current both on beam defining aperture and the target can be measured in order to help adjusting the beam and to measure the number of particles arrived on the target. To monitor the target stability Rutherford backscattering (RBS) technique was applied. RBS spectrum was followed on-line by using the built-in ion implanted silicon detector of the chamber (fig. 6.7). α-particles backscattered from thulium form a peak in the spectra. The peak area per incident particles (proportional to the measured charge on the target) is constant, if the number of target atoms is constant. No target deterioration during the irradiations was observed.

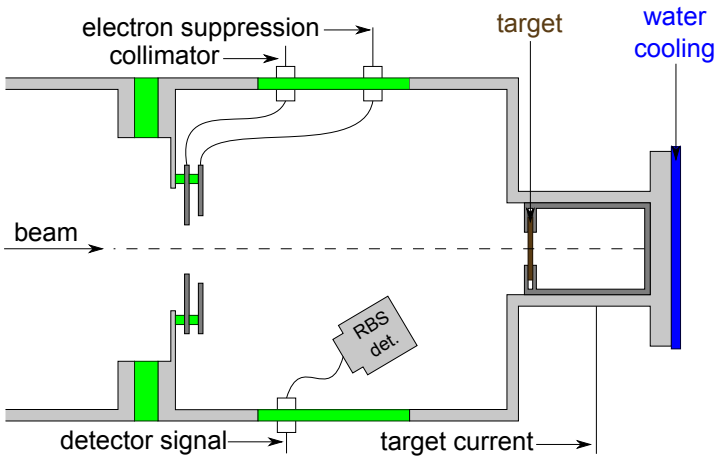

Figure 6.7: Schematic view of the activation chamber. Green parts are insulators.

The energy of the α beam was between $E_\alpha = 11.5 - 17.5$ MeV, covered with $0.5 - 1$ MeV steps (detailed list in table 6.2). Each irradiation lasted between 8 h and 24 h, and the collected charge was between 50 mC and 250 mC. Current integrator counts were recorded in multichannel scaling mode, stepping the channel every one minute to take into account the possible changes in the beam current.

6.3.4 Countings

Countings were performed with four different detectors offering different efficiency and background conditions. Some of the targets were measured with more than one detector (detailed list in table 6.2) to avoid systematic errors, and check the reliability of X-ray counting.

Detectors

γ-spectra of targets irradiated at higher bombarding energies (at and above 15 MeV) were recorded with an n-type coaxial HPGe detector with 40 % relative efficiency. This detector was used in several activation measurements at ATOMKI in the past (e.g. [28, 41, 48]). A 10 cm thick lead shield was applied during the countings with an opening at the rear side of the detector where its neck is.

In case of targets irradiated at 14.0 MeV and 13.5 MeV the already mentioned 100% HPGe detector was used. (see sec. 6.1)

In order to investigate further the effect of background on detection limit, a HPGe detector providing almost the lowest possible background was also used. This p-type HPGe detector with 86 % relative efficiency is located in LNGS (sec. 5.2.3). Strong reduction of cosmic radiation provides a unique possibility for ultra low background γ-detection. The detector was shielded from the environmental radioactivity by 10 cm Cu + 20 cm Pb shield and radon removal system was also applied [105]. The sample was placed directly on the relatively thin entrance window of 0.5 mm copper on the endcap to reach the highest possible efficiency.

X-ray countings were carried out with the LEGe detector. (see sec. 6.1)

Efficiencies

For cross section measurements, knowledge of the absolute efficiency of the detectors is necessary.

In case of the 40 % HPGe calibrated sources (^{57}Co, ^{133}Ba, ^{152}Eu, and ^{241}Am, ^{60}Co, ^{137}Cs) were used. For the 100 % HPGe additional single line sources (^{54}Mn, ^{65}Zn, ^{7}Be, ^{22}Na) were used. The efficiency for these detectors was measured at 10 cm source–detector distance. For the cross section measurements it is enough to know the absolute efficiency in the region of investigated γ-lines. In case of γ-counting at ATOMKI this region is between 800 keV and 1100 keV (table 6.1). Energy dependence of the efficiency on log-log scale appears to be linear in this region (fig. 6.4), therefore a fitted logarithmic straight line was used as calibration curve (fig. 6.8).

Efficiency of the low background detector at LNGS was determined by running a Monte Carlo simulation program based on GEANT4 [106]. The program was validated with calibrated point and volume γ-sources.

The absolute efficiency of the LEGe detector was determined using 53.16 keV, 79.61 keV and 81.00 keV lines of ^{133}Ba and 59.54 keV line of

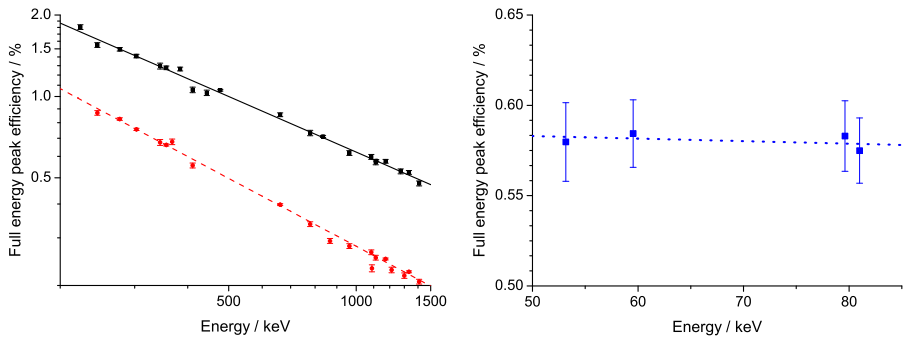

Figure 6.8: Used efficiency curves in case of the three ATOMKI detectors. Black solid and red dashed lines are log-log straight lines fitted to the measured points at 10 cm source–detector distance with the 100 % and 40 % HPGe, respectively. Blue dotted line is a fitted linear on the LEGe data measured at 16 cm source–detector distance.

^{241}Am calibrated radioactive sources at 16 cm source–detector distance. As it is shown in fig. 6.4 the efficiency does not vary so much in this energy range, therefore a linear fit was applied as efficiency calibration (fig. 6.8).

To increase the absolute efficiency, some of the countings were performed in so called "close geometry" (means 3 cm, at both measurements). At this distance true coincidence summing is not negligible, therefore, peak areas should be corrected, sometimes with more than 50 %. This applies also for the calibration sources. To avoid this complication the efficiencies were measured just in "far geometry" (In case of HPGe detectors it is 10 cm, at LEGe measurements 16 cm). For all measured transitions a conversion factor was calculated between the far and close geometry efficiencies. For this purpose, spectra of strong sources were recorded at both close and far geometry. Taking into account the decay between the two measurements, the conversion factor – containing both the ratio of efficiency at the two geometries and the true coincidence summing effect – for all transitions between the two geometries could be determined.

The self absorption of the targets was calculated by the LISE code [107], and found to be less than 0.2 % assuming the used target thicknesses.

6.3.5 Results

Several ^{169}Tm(α,n)^{172}Lu cross sections were measured above $E_\alpha \geq 13.5$ MeV both via X-ray and γ-counting, for $E_\alpha < 13.5$ MeV only via X-ray counting, because the γ yield was not sufficient for the analysis. Typical spectra are shown in fig. 6.9. The cross sections obtained from X-ray and γ-counting found to be in agreement within 4 %.

Because of high laboratory and beam-induced background (compared to weak signals from the reaction) γ-lines belonging to ^{169}Tm(α,γ)^{173}Lu reaction were not observable in the γ-spectra recorded at ATOMKI at any of the studied energies. Therefore, cross section of it was deduced only from X-ray counting, except targets irradiated with $E_\alpha = 13.5$ MeV and $E_\alpha = 17.5$ MeV. In these cases γ-countings were performed at LNGS in order to validate the X-ray counting method by the commercial γ-counting. In fig. 6.9 the peak from decay of ^{173}Lu is clearly seen, which can be used to

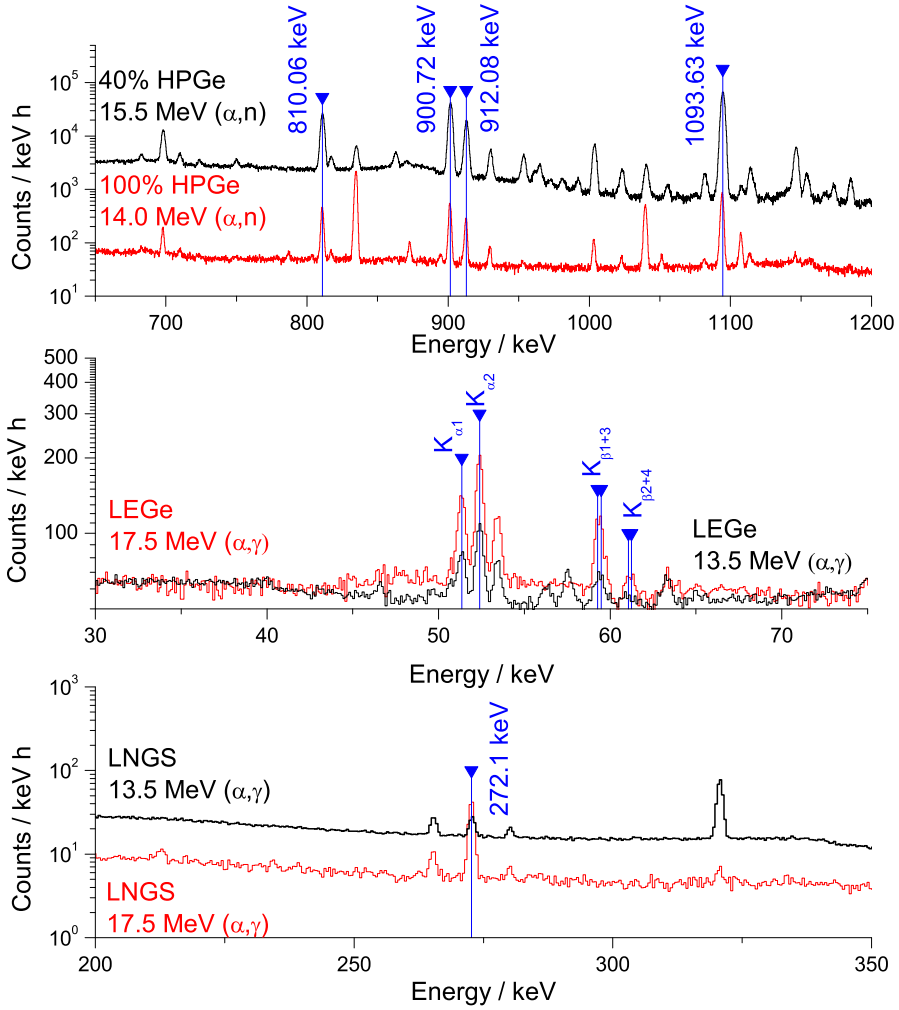

Figure 6.9: Top panel: Typical γ-ray spectra from the (α,n) channel recorded by the 40 % and 100 % HPGe detectors (black and red lines, respectively). The α-beam energy is also shown. Middle panel: X-ray spectra recorded by the LEGe at two bombarding energies. Bottom panel: γ-ray spectra from the (α,γ) channel at two bombarding energies recorded at LNGS. Peaks used for the analysis, are marked.

derive the cross section. Cross sections measured via X-ray counting and via γ-counting are in agreement within 3.5 %.

Table 6.4 and fig. 6.10 summarise the derived cross sections. Consistent results were found, regardless the detection method, the source–detector distance and the irradiation (where more than one target were irradiated at the same energy). It was proved, that the X-ray counting provides the same result as the widely used γ-counting. The X-ray counting can be the substitution of the γ-counting for several cross section measurement of astrophysical interest where the activation method can be used. The effective center-of-mass energies indicated in the second columns were calculated taking into account the beam energy loss in the target. From the known target thickness the energy loss was calculated with the SRIM code [108]. Since the cross section is a smoothly varying function of the energy in the studied energy range and it does not change much within the thicknesses of the target, the effective energy was chosen to correspond to the middle of the target. For the uncertainty of the effective energy the quadratic sum of half of the target thickness and the uncertainty of the beam energy was taken. The quadratic sum of partial errors shown in table 6.3 was used as final uncertainty of the cross sections.

The experimental cross section was compared to predictions of the statistical model code NON-SMOKER$^{\mathrm{WEB}}$ [109]. This can be seen in fig. 6.10, where the (α,n) cross section is overestimated by a factor of 3, and the (α,γ) by a factor of 5. The theoretical cross section for these reactions are mainly sensitive to the calculated average α widths which, in turn, mainly depend on the optical potential used. It is clearly seen that the standard optical α + nucleus potential by [110], widely used in astrophysical calculations,

Table 6.3: Error budget of the derived cross sections

efficiency of HPGe detector	6 %
efficiency of LEGe detector	4 %
the number of target atoms	4 %
current measurement	3 %
decay parameters	$\leq$ 5 %
counting statistics	0.5–7 %

Table 6.4: Derived experimental cross sections of ^{169}Tm(α,n)^{172}Lu and ^{169}Tm(α,γ)^{173}Lu reactions.

E_α / MeV	$E_{C.M.}$ / MeV	^{169}Tm(α,n)^{172}Lu σ / μbarn via X-ray	^{169}Tm(α,n)^{172}Lu σ / μbarn via γ-ray	^{169}Tm(α,γ)^{173}Lu σ / μbarn via X-ray	^{169}Tm(α,γ)^{173}Lu σ / μbarn via γ-ray
11.5	11.21 ± 0.06	0.57 ± 0.06			
11.85	11.55 ± 0.06	1.49 ± 0.16			
12.2	11.90 ± 0.06	4.1 ± 0.5			
12.5	12.19 ± 0.06	8.0 ± 0.7			
12.6	12.28 ± 0.09	9.8 ± 0.9		0.60 ± 0.15	
13.0	12.68 ± 0.07	28 ± 3		0.85 ± 0.13	
13.5	13.16 ± 0.07	94 ± 8		1.20 ± 0.12	1.31 ± 0.13
13.5	13.17 ± 0.08	96 ± 10	99 ± 8	1.35 ± 0.13	
14.0	13.65 ± 0.07	259 ± 21	265 ± 22	2.6 ± 0.2	
14.0	13.66 ± 0.07	261 ± 20		2.6 ± 0.2	
15.0	14.63 ± 0.08	$1\,874 \pm 146$	$1\,780 \pm 196$	8.1 ± 0.8	
15.0	14.63 ± 0.08	$1\,759 \pm 110$	$1\,962 \pm 169$	8.2 ± 0.8	
15.5	15.12 ± 0.08		$4\,471 \pm 366$	14.6 ± 1.5	
16.0	15.59 ± 0.08	$8\,778 \pm 685$	$8\,385 \pm 931$	21.9 ± 1.7	
16.0	15.64 ± 0.08	$7\,963 \pm 488$	$7\,911 \pm 704$	22.1 ± 1.7	
16.5	16.10 ± 0.08		$17\,075 \pm 1\,246$	30 ± 2	
17.0	16.59 ± 0.08	$33\,434 \pm 1\,929$	$31\,675 \pm 2\,597$	41 ± 3	
17.5	17.08 ± 0.09		$56\,436 \pm 4\,176$	61 ± 5	59 ± 4

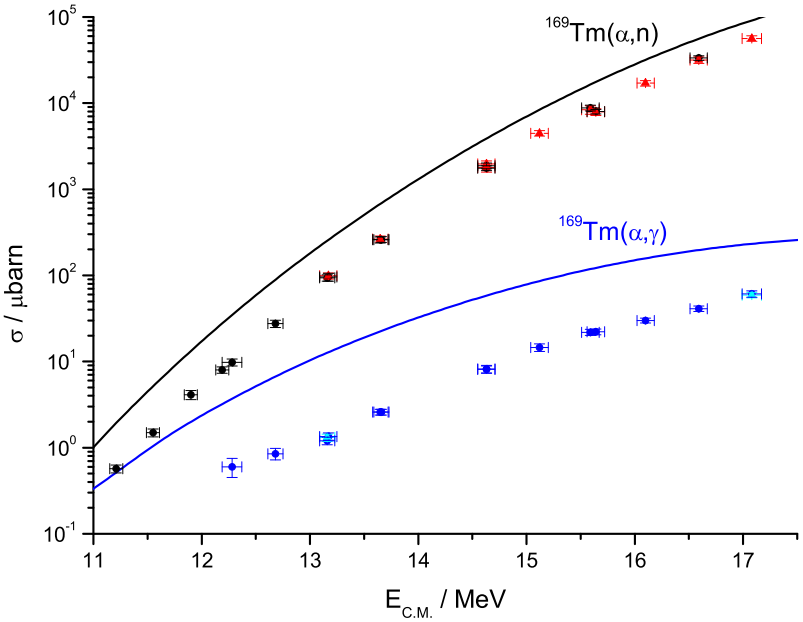

Figure 6.10: Cross sections listed in table 6.4, and theoretical curves [109]. Dots and triangles are values measured via X-ray and γ-ray, respectively.

may not be optimal at α energies close to or below the Coulomb barrier. The results underline the importance of measurements at energies as close as possible to the astrophysically relevant energy window, to construct reliable theoretical predictions.

The optimal shielding configuration was found out during the measurements, and was finished after the publication of most of the points. With the final shielding, the LEGe become suited to measure even lower cross section values. In case of thulium (α,γ) reaction cross sections at $E_\alpha = 13.0$ MeV and 12.6 MeV turned to be measurable. Publication of these points is in progress [111].

6.4 Feasibility of other α-induced reactions

Applicability of the activation technique based on X-ray counting was demonstrated by the cross section measurement of ^{169}Tm(α,n)^{172}Lu and ^{169}Tm(α,γ)^{173}Lu reactions. This is a powerful method for some cases where traditional γ-counting based activation measurements fail.

To see the opportunities in the activation method combined with X-ray counting, a feasibility study of some γ-process related cross section measurements is shown. One day long irradiations are assumed with typical 1 particle-μA beam current. A typical value of 100 μg/cm^2 active target thickness is considered (except the ^{124}Xe where tenth of this is assumed since it is a gas). Isotopic composition is assumed to be the maximum

Table 6.5: Several (α,γ) reactions related to the astrophysical γ-process, which lead to radioactive products. Some decay parameters are also listed.

Target nucleus	Enrichment / %	Half-life / d	Decaying nucleus	Strongest γ-ray E / keV	Strongest γ-ray I / %	Strongest X-ray E / keV	Strongest X-ray I / %	Ref.
^{121}Sb	99.7	59.41	^{125}I	35.4925 *5*	6.68 *13*	27.472	73.1 *19*	[112]
^{127}I	100	9.7	^{131}Cs	no γ-ray		29.782	38.9 *9*	[113]
^{124}Xe	99.99	2.43	^{128}Ba	273.44 *1*	14.5	30.973	38.8 *10*	[114]
^{130}Ba	11.8	3.16	^{134}La	604.721 *2*	5.04 *20*	33.442	38.8 *9*	[115]
^{136}Ce	30.6	3.37	^{140}Pr	1596.1 *2*	0.49	36.026	39.0 *9*	[116]
^{162}Er	28.2	2.36	^{166}Yb	82.29 *2*	15.552	50.742	69.0 *15*	[117]
^{168}Yb	85.0	683	^{172}Hf	23.9331 *2*	20.3 *17*	54.07	63 *6*	[102]
^{175}Lu	99.8	665	^{179}Ta	no γ-ray		54.07	21.9 *5*	[118]

enrichment available at the market shown in table 6.5. With this enrichment and the assumed waiting times, the (α,n) reaction on the investigated isotope, and the other open channels on the other isotopes would not disturb the X-ray counting. Table 6.5 also summarise the used parameters of the reactions (half-lives of the produced nucleus, and the intensity of the strongest γ- and X-ray transitions). Cross section was assumed to be tenth of the theoretical value from [109]. Usually this theoretical calculation overestimates the cross section by a factor of 5 (as in the ^{169}Tm(α,γ) case). With my assumption I can be sure that the yield in the detector would not be overestimated. The detector efficiency is considered to be 10 times the measured values (see fig. 6.4), which is approximately the real efficiency for both detectors at 1 cm source–detector distance. The counting times are assumed to be 30 days or one half-life if that is less. 10 days is accounted as waiting time (if the half-life of the isotope exceed this time), and 5 times the laboratory background rate is assumed (this was the typical background in the thulium source measurements). For the shorter living isotopes 1 day waiting time and 400 times the laboratory background rate is supposed. (Typical beam induced background from measurements.) Two times the measured resolution of the detectors (see last part of fig. 6.5) was used as ROI width for the background estimation.

Table 6.6 shows the minimum energies where experimental cross section data exists, and the calculated energy where the counts in the detector from

Table 6.6: Minimum reaction energies, where the cross section can be measured with the mentioned detectors via γ-ray or X-ray counting, for (α,γ) reactions mentioned in table 6.5.

Target nucleus	GW / MeV (T = 2 – 3 GK)	E_{min} / MeV Measured	Ref.	E_{min} / MeV HPGe	E_{min} / MeV LEGe γ	E_{min} / MeV LEGe X-ray
^{121}Sb	5.1 – 8.7	in progress		10.3	9.7	8.4
^{127}I	5.2 – 8.6	in progress		not possible		9.2
^{124}Xe	5.1 – 10.1	in progress		11.4	11.3	9.0
^{130}Ba	5.3 – 10.2	11.6	[101]	11.1	12.3	8.6
^{136}Ce	5.5 – 10.2			14.7	–	9.6
^{162}Er	6.2 – 11.5			12.3	11.7	10.1
^{168}Yb	6.3 – 11.6	in progress		13.4	13.0	12.2
^{175}Lu	4.7 – 9.6			not possible		12.5

the reactions would be equal to our detection limit (see sec. 2.4.4). With the X-ray counting the upper edge of the effective energy window (GW) [31] turned to be reachable for most of the reactions, or experimental data can be obtained for reactions where γ-rays can not be counted.

6.5 Conclusions

One of the main topics of the ATOMKI nuclear astrophysics group is to measure (α,γ) cross sections of astrophysical interest with the activation method. The accumulated activity is usually determined from the counting of γ-rays emitted by the product nuclei.

Recently, the possibility was investigated to determine the activity from X-ray counting. For this purpose a LEGe detector was used. I designed and built up a multi-layer shielding around the detector. To prove the applicability of this new counting system, I made sensitivity calculations. The LEGe was compared to a coaxial HPGe detector with 100 % relative efficiency in a commercial low background shielding made of 10 cm thick lead. It turned out, that the LEGe in its home made shielding is more suited to count γ- and X-rays up to 350 keV energy.

During the fine tuning of the shielding of the system, the cross section of α-induced reactions on ^{169}Tm was measured via X-ray detection. This measurement proves the applicability of the activation method combined with X-ray counting. (Related publications from my publication list: Scientific papers: 2, 3; Other publication: 3; Talk: 3; Poster: 5.)

I calculated the feasibility of several (α,γ) cross section measurements, related to the γ-process, both via counting the γ- or the X-rays with the LEGe detector. It turned out that most of the considered cross sections can be measured closer to the Gamow window via the X-ray counting, opening the way for more precise stellar reaction rate determinations. Based on my calculations, some of these reaction studies have already started at ATOMKI.

Summary

In this chapter a summary of my thesis is given both in English and in Hungarian. It includes the motivation, the experimental work, results, and new possibilities opened up using the findings of this work.

Summary

This dissertation summarises my work between 2008 and 2012 at ATOMKI in the subject of low cross section measurement methods, and my laboratory background measurements in Dresden at the Research Centrum (HZDR) and at the underground laboratory (Felsenkeller) during my half year long fellowship in 2009. I also performed some laboratory background measurements deep underground at Gran Sasso National Laboratory (LNGS).

The cross section of astrophysically relevant charged particle induced reactions in stellar environment is usually very low, sometimes in the picobarn range or below. Usually the parameters of the reactions are well known at higher energies (above the Coulomb barrier), but the extrapolation from these data are very uncertain. One aim of the experimental nuclear astrophysics is to measure these reaction cross sections in the energy range in which they occur in stars (Gamow window), much below the Coulomb barrier, where the cross sections drop exponentially with decreasing energy. Therefore, towards the Gamow window very low experimental yields should be detected. In my thesis I am dealing with background reduction and signal enhancement techniques to get higher sensitivity, thus

smaller measurable cross sections closer to the Gamow window. I made feasibility studies for both subjects to determine which is the lowest energy, where a reaction cross section is still measurable under the explained conditions.

Background reduction

The laboratory background measurements were performed at the surface of Earth, and at underground laboratories with different depths. The aim of my measurements was to check the effect of the active shielding on the high energy ($E_\gamma > 3\,\mathrm{MeV}$) laboratory background. The surface locations were the ATOMKI and the HZDR. The shallow underground (47 m depth) location was the Dresden Felsenkeller laboratory in Germany, while the deep underground (1400 m depth) place was the Gran Sasso laboratory in Italy. The same actively shielded HPGe Clover detector was used subsequently at each sites, to avoid the differences not attributed to the laboratory. In addition, I measured the laboratory background with three other detectors at the mentioned sites, too. The effect of the active shield was tested at the surface and at Felsenkeller by a $LaBr_3$ detector too, while the effect of the depth was also tested by a NaI scintillator and a HPGe detector with 60 % relative efficiency.

My measurements proved, that at deep underground the active shield causes no substantial reduction in the high energy background region, while at shallow underground it is more efficient than at the surface. Because the underground location by itself already reduces the high energy laboratory background, the additional active shield results in a counting rate comparable to that at the deep underground site, within a factor of 2–3 difference. The reason of this effect is that the background is dominated by the direct effect of the muons from the cosmic-rays at shallow underground, which can be vetoed very effectively by the active shield, however, at deep underground the main background sources are the (n,γ) reactions, since the muons are highly suppressed (their flux is reduced by a factor of 10^6). The naturally occurring neutron background cannot be reduced further by an active shield.

With the measured laboratory background rates, I calculated the feasibility of some astrophysically relevant reactions, which are producing high energy γ-rays, considering the Clover detector in a geometry that has already been used for in-beam cross section measurements of astrophysical interest. I calculated the time requirement for the reactions at different sites, in the projectile energy range which was not considered to be measurable at a surface laboratory. It should be emphasised, that using an active shield at a shallow underground location provides reasonably low laboratory background to these reactions. They turned to be measurable in realistic time already at shallow underground. This finding opens the way to a complementary approach, where shallow underground laboratories can first quickly gain low-energy data near the Gamow peak, and deep underground laboratories with even better background conditions push the data limits even lower for the selected important reactions.

Signal enhancement

The second part of my thesis deals with the improvement of cross section measurement for the γ-process based on the widely used activation technique. Higher signal is expected when the accumulated activity is measured via detection of the X-rays released after the decay of the radioactive reaction product nuclei instead of detecting the γ-rays. This is possible, because in this mass range the produced radioactive isotopes decay totally or partially via electron capture, followed by X-ray emission. The relative intensities of these X-rays are usually much higher than that of the γ-rays, and also the efficiency of the detectors is the highest in the energy range of the X-rays. The disadvantage of the X-ray detection is that one can not separate different isotopes of the same element. Care has to be taken to circumvent somehow this problem. It can be done if the half-lives of them are different. Following the decay-curve of the X-ray peak and fitting it by several exponentials, the produced partial activities can be derived.

For the X-ray counting a LEGe detector was used, for which I designed and built up a multi layer shield. I compared the sensitivity of this detector to a HPGe detector with 100% relative efficiency in a commercial 10 cm

thick lead shielding. It was proved, that the sensitivity of the LEGe detector is a factor of 3.5 higher in the X-ray region than that of the HPGe, and the LEGe is more suited to count γ- or X-rays up to 350 keV energy.

To demonstrate the applicability of the X-ray detection method, I measured α-induced reaction cross sections on ^{169}Tm. This element has only one stable isotope, therefore the enrichment was naturally granted. In the energy range where the expected yield from the reaction is higher than the detection limit (above 12 MeV) both the (α,n) and (α,γ) reactions take place. The resulted two lutetium isotopes can be separated with two countings, owing to the very different half-lives (6.7 days and 500 days). Right after the irradiation the activity of isotope from the much stronger (α,n) channel can be measured and several months later only the other isotope from the (α,γ) channel produces the X-ray peak. Several cross sections were also measured via the conventional γ-counting. Consistent results were obtained. With this I proved that the X-ray and γ-ray countings are identically usable for deriving the accumulated activity, and with X-ray counting lower cross sections are measurable. The method opens the way to cross section measurements with the activation technique, which were not measurable before via γ-ray counting, and/or can push the measurable energy range down, closer to the Gamow window. In this mass range there is no experimental data for α-capture reactions, however the γ-process is the most sensitive to them. The experimental data reported in this work can be used to test and improve the theoretical cross section calculations for the astrophysical γ-process.

I also performed a feasibility study of different (α,γ) cross section measurements relevant to the γ-process. In most cases the measurable energy range reaches the Gamow window. Based on my calculations the cross section measurement of some reactions has already started at ATOMKI.

Összefoglalás

Dolgozatom összefoglalja az ATOMKI-ben 2008 és 2012 között végzett kis hatáskeresztmetszetek mérési módszereinek továbbfejlesztését célzó vizsgálataimat, valamint az olasz Gran Sasso-i mély földalatti laboratóriumban (LNGS) és 2009-ben féléves ösztöndíjam alatt a drezdai kutatóintézetben (HZDR) és földalatti laborban (Felsenkeller) végzett laboratóriumi háttér méréseimet.

Az asztrofizikai szempontból fontos töltött részecskékkel lejátszódó magreakcióknak általában kicsi a hatáskeresztmetszete a csillaghőmérsékletnek megfelelő alacsony energiák mellett, sokszor a pikobarn tartományba vagy az alá esik. A reakciók paraméterei általában jól ismertek nagy reakcióenergiák mellett (a Coulomb gát felett), de az ezen mérésekből végzett extrapoláció bizonytalansággal terhelt. A kísérleti nukleáris asztrofizika egyik célja, hogy minél közelebbi energián mérje meg a reakciók hatáskeresztmetszeteit a csillagokban uralkodó energiákhoz (Gamow ablak), jóval a Coulomb gát alatt, hogy csökkentse az extrapoláció bizonytalanságát. Gamow ablak közeli energiákon a hatáskeresztmetszetek exponenciálisan csökkennek az energia csökkenésével, így nagyon kis reakcióhozamokat kell detektálni. Dolgozatom a γ-detektorokban fellépő laboratóriumi háttér csökkentési módszereivel és a jel nagyságát növelő lehetőségekkel foglalkozik részletesen. Mindkét módszerrel az érzékenység növelése volt a célom, hogy minél kisebb hatáskeresztmetszetek mérhetővé váljanak, ezzel a Gamow ablakhoz közelebbi kísérleti adatokat nyerhessünk. Megvalósíthatósági számításokat végeztem mindkét eljáráshoz, megbecsülve azt a minimális energiát, ahol még egy-egy reakciót meg lehetne mérni adott körülmények között.

Háttércsökkentés

Laboratóriumi háttér méréseket végeztem földfelszínen és különböző mélységekben. Méréseim célja a mélység és az aktív pajzs nagyenergiás ($E_\gamma > 3\,\mathrm{MeV}$) háttérre gyakorolt együttes hatásának tesztelése volt. Földfelszínen az ATOMKI-ben és a drezdai HZDR-ben végeztem méréseket.

A sekély (47 m mély) földalatti helyszín a drezdai Felsenkeller labor volt, míg a mély (1400 m) földalatti méréseket az olaszországi Gran Sasso laboratóriumban végeztem. Ugyanazt az aktív pajzzsal ellátott HPGe Clover detektort használtam mindegyik laboratóriumban, hogy elkerüljem a helyszínnel össze nem függő eltéréseket. Összehasonlításképp három másik detektorral is végeztem méréseket az említett helyszíneken. Az aktív pajzs hatását a felszínen és a Felsenkellerben egy $LaBr_3$ detektorral is teszteltem, míg a mélység hatását egy NaI és egy 60 %-os relatív hatásfokú HPGe detektorral is ellenőriztem.

Megállapítottam, hogy az aktív árnyékolás a mély földalatti helyszínen nem jelent további laboratóriumi háttércsökkentést a nagyenergiás tartományban, viszont a sekély földalatti laborban még a felszíni hatásánál is hatékonyabbnak bizonyult. Mivel a földalatti elhelyezés önmagában is csökkenti a kozmikus hátteret, így a sekély földalatti elhelyezkedés és az aktív pajzs együttes alkalmazása a mély földalattival azonos nagyságrendbe eső beütésszámokat eredményez a nagyenergiás laboratóriumi háttértartományban (2–3-szor magasabb beütésszám). Mindez annak köszönhető, hogy a sekély földalatti kozmikus müonok dominálta háttér nagyon hatékonyan csökkenthető az aktív árnyékolással, míg mélyen a föld alatt a kozmikus müonok hatása elhanyagolható, itt már az (n,γ) reakciók uralják a nagyenergiás háttértartományt, melyekre az aktív pajzs nincs hatással.

A mért laboratóriumi háttér beütésszámokkal megbecsültem néhány asztrofizikailag fontos, nagyenergiás γ-sugárzást kibocsátó magreakció mérésének megvalósíthatóságát. A becsléshez a korábban hasonló in-beam hatáskeresztmetszet méréshez alkalmazott Clover elrendezést vettem alapul. Megbecsültem a reakciók mérési idejét a különböző helyszíneken, olyan energiákon, ahol korábban a földfelszínen nem találták a reakciókat mérhetőnek. Megmutattam, hogy egy sekély földalatti laborban megfelelő aktív árnyékolást alkalmazva elegendően alacsony hátteret nyerünk e reakciók reális idő alatti méréséhez. Ezzel megteremthetjük az utat egy többlépcsős mérésnek, amelyben már a sekély földalatti laborok is alacsony energiás, asztrofizikailag fontos hatáskeresztmetszeteket szolgáltatnak, és csak a nagyobb pontosság eléréséhez, illetve a méréshatárok még lejjebb szorításához szükségesek a nehezen hozzáférhető mély földalatti laborok.

Jelnövelés

Dolgozatom második fele az asztrofizikai γ-folyamat modellezéséhez fontos hatáskeresztmetszetek méréseihez használt aktivációs technika egy új, továbbfejlesztett változatát mutatja be. Nagyobb jelet várunk, ha a létrehozott aktivitást nem γ-sugárzás detektálása alapján, hanem a bomlást követő karakterisztikus röntgensugárzás detektálása útján határozzuk meg. Ez azért lehetséges, mert a p-folyamat tömegtartományában a keletkező radioaktív végmagok nagy valószínűséggel elektronbefogással bomlanak, amit karakterisztikus röntgensugárzás kibocsátása követ. A röntgenfotonok intenzitásaránya általában nagyobb, mint a gammáké, emellett a legtöbb detektor hatásfoka a röntgen energiatartományban a legnagyobb. Hátránya a karakterisztikus röntgensugárzás detektálásának, hogy ugyan az elemekre jellemző, de izotópok közt nem tud különbséget tenni, így valamilyen más módszerrel el kell választanunk a keletkezett reakciótermékek aktivitását. Ezt könnyen megtehetjük a röntgencsúcs bomlási görbéjének követésével. A görbét több exponenciális függvény összegével illesztve a rész-aktivitások egyenként meghatározhatók.

A röntgenmérésekhez egy LEGe detektort használtunk, amihez több rétegű árnyékolást terveztem és építettem. Használhatóságának bizonyítására összehasonlítottam érzékenységét egy 100 % relatív hatásfokú HPGe detektorral, amit 10 cm ólomárnyékolás vett körül. Megmutattam, hogy az általam összeállított árnyékolásban a LEGe detektor 3,5-ször érzékenyebb a röntgen energiatartományban, és 350 keV γ-energiáig alkalmasabb az aktivitás mérésére, mint a 100 %-os HPGe detektor.

A röntgendetektálási módszer alkalmazhatóságának bizonyítására ^{169}Tm izotópon mértünk α indukált hatáskeresztmetszeteket. Ez az elem egyetlen stabil izotóppal rendelkezik, így a dúsítás természetesen megoldott. A detektálási küszöböt meghaladó hozamot eredményező α energiákon (12 MeV felett) az (α,n) és (α,γ) reakciók is lejátszódnak. A két keletkező lutécium izotópot nagy felezési idő különbségük segítségével (6,7 nap és 500 nap) választottuk szét. A besugárzás után megmértük az (α,n) csatorna aktivitását, míg hónapokkal később már csak az (α,γ) aktivitás maradt a mintában. Összehasonlításul néhány hatáskeresztmetszetet hagyományos

módszerrel γ-sugárzás detektálásának segítségével is meghatároztunk. Konzisztens eredményeket kaptunk, ezzel bizonyítva, hogy a karakterisztikus röntgensugárzás és γ-sugárzás detektálása egyaránt alkalmazható az aktivitás meghatározására nukleáris asztrofizikai aktivációs mérésekben, ezenfelül a röntgensugárzás detektálásával kisebb hatáskeresztmetszetek is mérhetők.

A módszer utat nyit a γ-számlálást használó aktivációs hatáskeresztmetszet mérésekkel nem elérhető reakciók vizsgálatához, illetve a mérhető energiatartomány kiterjesztéséhez a Gamow ablak felé.

Végül a dolgozat különböző α indukált reakciók detektálási határának becslésével foglalkozik a LEGe detektor esetén. Megmutattam, hogy szinte minden esetben lejjebb vihető a mérhető energia tartomány – közelebb az asztrofizikailag fontos tartományhoz – néhány reakcióra elérve a Gamow ablakot is. Számításaim nyomán a megbecsült reakciók közül néhánynak a kísérleti vizsgálata már el is kezdődött az ATOMKI-ben.

Acknowledgment

My thesis summarises more than four years of work during my PhD course. I got guidance and the help from many people during these years, it is my pleasure to thank all of them.

First of all, I would like to thank the Nuclear Astrophysics Group of ATOMKI. I am glad for the opportunity to be a member of this group. I would like to thank my supervisor Zsolt Fülöp for inviting me to this group and guiding me during the years. Special thanks goes to the members of the group namely György Gyürky, Endre Somorjai, Gábor Kiss, János Farkas, and Zoltán Halász for the continuous help in the everyday works.

I am grateful to be a member of the LUNA collaboration, and to have the opportunity to perform part of my work at a deep underground laboratory.

I am thankful to Daniel Bemmerer for supervising my work at Dresden during my time spent there. I would like to acknowledge the Herbert Quandt Stiftung for the half year long fellowship. Thanks to Matthias Köhler and the VKTA for providing access for me to the Felsenkeller underground laboratory, and helping me during the measurements.

I am indebted to Zsolt Fülöp, György Gyürky, Endre Somorjai, Daniel Bemmerer, and Peter Mohr for the careful reading and correction of my thesis.

Last but not least, I would like to thank for the support and help got from my family, friends, and beloved girlfriend.

Publications

Scientific papers related to the PhD thesis

1. **T. Szücs**, D. Bemmerer, C. Broggini, A. Caciolli, F. Confortola, P. Corvisiero, Z. Elekes, A. Formicola, Zs. Fülöp, G. Gervino, A. Guglielmetti, C. Gustavino, Gy. Gyürky, G. Imbriani, M. Junker, A. Lemut, M. Marta, C. Mazzocchi, R. Menegazzo, P. Prati, V. Roca, C. Rolfs, C. Rossi Alvarez, E. Somorjai, O. Straniero, F. Strieder, F. Terrasi and H. P. Trautvetter (LUNA Collaboration)
An actively vetoed Clover γ-detector for nuclear astrophysics at LUNA
European Physical Journal A **44**, 513 (2010)

2. G. Gy. Kiss, T. Rauscher, **T. Szücs**, Zs. Kertész, Zs. Fülöp, Gy. Gyürky, C. Fröhlich, J. Farkas, Z. Elekes, and E. Somorjai
Determining reaction cross sections via characteristic X-ray detection: α-induced reactions on ^{169}Tm for the astrophysical γ-process
Physics Letters B **695**, 419 (2011)

3. G. Gy. Kiss, **T. Szücs**, Gy. Gyürky, Zs. Fülöp, J. Farkas, Zs. Kertész, E. Somorjai, M. Laubenstein, C. Fröhlich, and T. Rauscher
Activation method combined with characteristic X-ray counting: A possibility to measure (α,γ) cross sections
Nuclear Physics A **867**, 52 (2011)

4. **T. Szücs**, D. Bemmerer, T. Cowan, D. Degering, Z. Elekes, Zs. Fülöp, Gy. Gyürky, A. Junghans, M. Köhler, M. Marta, R. Schwengner, A. Wagner, and K. Zuber
Shallow-underground accelerator sites for nuclear astrophysics: Is the background low enough?
European Physical Journal A **48**, 8 (2012)

Conference proceedings and other publications related to the PhD thesis

1. **T. Szücs**
   Laboratory background of an escape-suppressed Clover γ-ray detector overground, shallow underground, and deep underground
   AIP Conference Proceedings **1213**, 246 (2010)

2. **T. Szücs**
   Laboratory background of an escape-suppressed clover γ-ray detector at different environments
   Acta Physica Debrecina **44**, 141 (2010)

3. **T. Szücs**
   α induced cross section measurement on ^{169}Tm for the astrophysical γ-process
   Acta Physica Debrecina **45**, 218 (2011)

4. **T. Szücs**, D. Bemmerer, T. Cowan, and K. Zuber
   A possible underground accelerator in the Dresden Felsenkeller
   Journal of Physics: Conference Series **337**, 012032 (2012)

Talks related to the PhD thesis

1. **T. Szücs**
   Laboratory background of an escape-suppressed Clover γ-ray detector overground, shallow underground, and deep underground
   5th European Summer School on Experimental Nuclear Astrophysics, Santa Tecla, Catania, Italy, 20–27 September, 2009

2. **T. Szücs**
   Laboratory γ-background studies with an actively shielded High Purity Germanium (HPGe) detector in Felsenkeller
   Work in Progress Seminar. Forschungszentrum Dresden Rossendorf, Dresden, Germany, 2 October, 2009

3. **T. Szücs**
   Current status of ATOMKI measurements, and future plans
   Workshop on Data Requirements in Nuclear Astrophysics,
   Darmstadt, Germany, 25–27 July, 2010

Posters related to the PhD thesis

1. **T. Szücs**, *et al.* (LUNA Collaboration)
   An escape-suppressed Clover γ-ray detector overground and underground
   Nuclear Physics in Astrophysics IV (NPA4),
   Frascati, Italy, 8–12 June, 2009

2. **T. Szücs**
   An escape-suppressed germanium gamma-ray detector at the Felsenkeller Underground Laboratory
   4th PhD Seminar, Forschungszentrum Dresden Rossendorf,
   Dresden, Germany, 16–18 September, 2009

3. **T. Szücs**
   An escape-suppressed germanium γ-ray detector at the Felsenkeller underground laboratory
   Underground Nuclear-Reaction Experiments for Astrophysics and Applications, Dresden, Germany, 28–30 April, 2010

4. D. Bemmerer, K. Zuber, and **T. Szücs**
   A possible accelerator laboratory in the Dresden Felsenkeller
   11th International Symposium on Nuclei in the Cosmos (NIC XI)
   Heidelberg, Germany, 19–23 July, 2010

5. G. Gy. Kiss, Gy. Gyürky, T. Rauscher, **T. Szücs**, Zs. Kertész, J. Farkas, Zs. Fülöp, and E. Somorjai
   Measuring alpha-induce cross sections in the region of heavy p-nuclei: The case of $^{169}Tm+\alpha$
   11th International Symposium on Nuclei in the Cosmos (NIC XI)
   Heidelberg, Germany, 19–23 July, 2010

6. D. Bemmerer, T. Cowan, **T. Szücs**, and K. Zuber
   A possible accelerator laboratory in the Dresden Felsenkeller
   Nuclear Physics in Astrophysics V. (NPA5),
   Eilat, Israel, 3–8 April, 2011

Other publications

1. Gy. Gyürky, ..., **T. Szücs**, *et al.*
Precise half-life measurement of the 10 h isomer in ^{154}Tb
Nuclear Physics A **828**, 1 (2009)
2. Gy. Gyürky, ..., **T. Szücs**, *et al.*
Alpha-induced reaction cross section measurements on ^{151}Eu for the astrophysical γ-process
Journal of Physics G Nuclear and Particle Physics **37**, 115201 (2010)
3. M. Marta, ..., **T. Szücs**, *et al.*
Resonance strengths in the $^{14}N(p,\gamma)^{15}O$ and $^{15}N(p,\alpha\gamma)^{12}C$ reactions
Physical Review C **81**, 055807 (2010)
4. Gy. Gyürky, ..., **T. Szücs**, *et al.*
Alpha-induced reactions for the astrophysical p-process: The case of ^{151}Eu
Journal of Physics: Conference Series **202**, 012004 (2010)
5. C. Mazzocchi, ..., **T. Szücs**, *et al.* (LUNA Collaboration)
Nuclear astrophysics deep underground: The LUNA experiment
Proceedings of Science **BORMIO2010**, 055 (2010)
6. Q. Zhong, ..., **T. Szücs**, *et al.*
$^{96}Ru(p,\gamma)^{97}Rh$ measurement at the GSI storage ring
Journal of Physics: Conference Series **202**, 012011 (2010)
7. J. Farkas, ..., **T. Szücs**, *et al.*
Half-life measurement of ^{133m}Ce with γ-spectrometry
European Physical Journal A **47**, 7 (2011)
8. C. Broggini, ..., **T. Szücs**, *et al.* (LUNA Collaboration)
Twenty years of LUNA
Progress in Particle and Nuclear Physics **66**, 293 (2011)
9. M. Erhard, ..., **T. Szücs**, *et al.* (LUNA Collaboration)
Study of the Big Bang Nucleosynthesis reaction D(α, γ)^{6}Li deep underground at LUNA
Proceedings of Science **NIC IX**, 003 (2011)
10. H. Costantini, ..., **T. Szücs**, *et al.* (LUNA Collaboration)
Reaction rate measurements in underground laboratories
Proceedings of Science **NIC IX**, 014 (2011)
11. A. Caciolli, ..., **T. Szücs**, *et al.* (LUNA Collaboration)
LUNA: The $^{15}N(p,\gamma)^{16}O$ reaction study at low energies with a BGO detector
Proceedings of Science **NIC IX**, 117 (2011)

12. **T. Szücs**, *et al.*
The new p-process database of KADoNiS
Proceedings of Science **NIC IX**, 247 (2011)

13. Gy. Gyürky, ..., **T. Szücs**, *et al.*
Target characterization for the $^{130}Ba(\alpha,\gamma)^{134}Ce$ γ-process experiment
Proceedings of Science **NIC IX**, 238 (2011)

14. A. Guglielmetti, ..., **T. Szücs**, *et al.* (LUNA Collaboration)
Recent results on (p,γ) and (α,γ) fusion reactions at LUNA
EPJ Web of Conferences **17**, 06001 (2011)

15. G. Imbriani, ..., **T. Szücs**, *et al.* (LUNA Collaboration)
Direct measurements of cross section of astrophysical interest
Journal of Physics: Conference Series **312**, 042004 (2011)

16. Gy. Gyürky, ..., **T. Szücs**, *et al.*
Half-life measurement of ^{66}Ga with γ-spectroscopy
Applied Radiation and Isotopes **70**, 278 (2012)

17. Z. Halász, ..., **T. Szücs**, *et al.*
α-capture on ^{130}Ba for the synthesis of p-isotopes
Physical Review C **85**, 025804 (2012)

18. D. Trezzi D, ..., **T. Szücs**, *et al.* (LUNA Collaboration)
Nuclear astrophysics deep underground: The LUNA experiment
Acta Physica Polonica B **43**, 221 (2012)

19. A. Bellini, ..., **T. Szücs**, *et al.* (LUNA Collaboration)
Direct measurement of the $^{2}H(\alpha,\gamma)^{6}Li$ cross section at energies of astrophysical interest
Journal of Physics: Conference Series **337**, 012053 (2012)

20. A. Caciolli, ..., **T. Szücs**, *et al.* (LUNA Collaboration)
Study of the $^{15}N(p,\gamma)^{16}O$ at LUNA
Journal of Physics: Conference Series **337**, 012060 (2012)

21. Gy. Gyürky, ..., **T. Szücs**, *et al.*
Experimental study of α-induced reactions on ^{64}Zn for the astrophysical γ-process
Journal of Physics: Conference Series **337**, 012009 (2012)

22. Z. Halász, ..., **T. Szücs**, *et al.*
Towards in-beam (α,γ) cross section measurements for the astrophysical γ-process
Journal of Physics: Conference Series **337**, 012063 (2012)

23. **T. Szücs**, *et al.*
The KADoNiS databases - progress and future plans
Journal of Physics: Conference Series **337**, 012033 (2012)

Bibliography

[1] E. Rutherford,
Collisions of alpha particles with light atoms. IV. An anomalous effect in nitrogen.
Philosophical Magazine **37**, 581 (1919)

[2] F. W. Aston,
The mass-spectra of chemical elements,
Philosophical Magazine **39**, 233 (1920)

[3] G. Gamow,
Zur Quantentheorie des Atomkernes,
Zeitschrift für Physik **51**, 204 (1928)

[4] R. d'E. Atkinson and F. G. Houterman,
Aufbaumöglichkeit in Sternen,
Zeitschrift für Physik **54**, 565 (1929)

[5] H. A. Bethe,
Energy Production in Stars,
Physical Review **55**, 434 (1939)

[6] R. A. Alpher, H. Bethe, and G. Gamow,
The Origin of Chemical Elements,
Physical Review **73**, 803 (1948)

[7] E. M. Burbidge, G. R. Burbidge, W. A. Fowler, and F. Hoyle,
Synthesis of Elements in Stars,
Review of Modern Physics **29**, 547 (1957)

[8] A. G. W. Cameron,
Report CRL-41,
Atomic Energy of Canada Ltd., Chalk River (1957)

[9] C. Rolfs and W. Rodney,
Cauldrons in the Cosmos,
The University of Chicago Press (1988)

[10] C. Iliadis,
Nuclear Physics of Stars,
WILEY-VCH Verlag Gmbh Co. KGaA (2007)

[11] R. N. Boyd,
An introduction to Nuclear Astrophysics,
The University of Chicago Press (2008)

[12] K. Lodders, H. Palme, and H.-P. Gail,
4.4 Abundances of the elements in the Solar System,
J.E. Trümper (ed.), SpringerMaterials - The Landolt-Börnstein Database (`http://www.springermaterials.com`)
Springer-Verlag Berlin Heidelberg (2009)

[13] M. Busso, R. Gallino, and G. J. Wasserburg,
Nucleosynthesis in Asymptotic Giant Branch Stars: Relevance for Galactic Enrichment and Solar System Formation,
Annual Review of Astronomy and Astrophysics **37**, 239 (1999)

[14] L.-S. The, M. El Eid, and B. Meyer,
A new study of s-process nucleosynthesis in massive stars,
The Astrophysical Journal **533**, 998 (2000)

[15] Y.-Z. Qian,
Supernovae versus neutron star merges as the major r-process sources,
The Astrophysical Journal Letters **534**, L67 (2000)

[16] C. Freiburghaus, S. Rosswog, and F.-K. Thielemann,
r-process in neutron star merges,
The Astrophysical Journal Letters **525**, L121 (1999)

[17] S. E. Woosley and W. M. Howard,
The p-process in supernovae,
The Astrophysical Journal Supplement Series **36**, 285 (1978)

[18] M. Arnould and S. Goriely,
The p-process of stellar nucleosynthesis: astrophysics and nuclear physics status,
Physics Reports **384**, 1 (2003)

[19] T. Rauscher, A. Heger, R. D. Hoffman, and S. E. Woosley,
Nucleosynthesis in Massive Stars with Improved Nuclear and Stellar Physics,
The Astrophysical Journal **576**, 323 (2002)

[20] W. Rapp, J. Görres, M. Wiescher, H. Schatz, and F. Käppeler,
Sensitivity of p-process nucleosynthesis to nuclear reaction rates in a 25 $M_\odot$ supernova model,
The Astrophysical Journal **653**, 474 (2006)

[21] T. Rauscher,
Branchings in the γ process path revisited,
Physical Review C **73**, 015804 (2006)

[22] B. Pritychenko,
Stellar Nucleosynthesis Nuclear Data Mining,
Brookhaven National Laboratory Report BNL-96393-2011-BC

[23] T. Szücs, I. Dillmann, R. Plag, Zs. Fülöp,
The new p-process database of KADoNiS,
Proceedings of Science **(NIC XI)** 247 (2011)

[24] H. Schatz, *et al.,*
rp-process nucleosynthesis at extreme temperature and density conditions,
Physics Reports **294**, 167 (1998)

[25] C. Fröhlich, *et al.,*
Neutrino-Induced Nucleosynthesis of A>64 Nuclei: The νp Process,
Physical Review Letters **96**, 142502 (2006)

[26] C. Nair, *et al.,*
Photodisintegration studies on p-nuclei: the case of Mo and Sm isotopes,
Journal of Physics G: Nuclear and Particle Physics **35**, 014036 (2008)

[27] P. Mohr, Zs. Fülöp, and H. Utsunomiya,
Photo-induced nucleosynthesis:
Current problems and experimental approaches,
The European Physical Journal A **32**, 357 (2007)

[28] G. G. Kiss, *et al.,*
Coulomb Suppression of the Stellar Enhancement Factor,
Physical Review Letters **101**, 191101 (2008)

[29] T. Rauscher, *et al.,*
Suppression of the stellar enhancement factor and the reaction $^{85}Rb(p,n)^{85}Sr$*,*
Physical Review C **80**, 035801 (2009)

[30] `http://www.kadonis.org`

[31] T. Rauscher,
Relevant energy ranges for astrophysical reaction rates,
Physical Review C **81**, 045807 (2010)

[32] G. F. Knoll,
Radiation Detection and Measurement,
John Wiley & Sons Inc., New York (2000)

[33] G. R. Gilmore,
Practical Gamma-ray Spectrometry,
John Wiley & Sons Ltd., Chichester (2008)

[34] J. Simpson,
The AGATA Project,
Journal of Physics G: Nuclear and Particle Physics **31**, S1801 (2005)

[35] A. Spyrou, *et al.,*
Cross-section measurements of capture reactions relevant to the p process using a 4π γ*-summing method,*
Physical Review C **76**, 015802 (2007)

[36] E. Somorjai, *et al.,*
Experimental cross section of $^{144}Sm(\alpha,\gamma)^{148}Gd$ *and implications for the p-process,*
Astronomy & Astrophysics **333**, 1112 (1998)

[37] Gy. Gyürky, *et al.,*
Proton capture cross section of Sr isotopes and their importance for nucleosynthesis of proton-rich nuclides,
Physical Review C **64**, 065803 (2001)

[38] W. Rapp, *et al.,*
α- and neutron-induced reactions on ruthenium isotopes,
Physical Review C **66**, 015803 (2002)

[39] S. Galanopoulos, *et al.,*
The $^{88}Sr(p,\gamma)^{89}Y$ reaction at astrophysically relevant energies,
Physical Review C **67**, 015801 (2003)

[40] Gy. Gyürky, *et al.,*
Proton induced reaction cross section measurements on Se isotopes for the astrophysical p process,
Physical Review C **68**, 055803 (2003)

[41] Gy. Gyürky, *et al.,*
α-induced cross sections of ^{106}Cd for the astrophysical p process,
Physical Review C **74**, 025805 (2006)

[42] Gy. Gyürky, *et al.,*
Proton capture cross-section of $^{106,108}Cd$ for the astrophysical p-process,
Journal of Physics G: Nuclear and Particle Physics **34**, 817 (2007)

[43] G. G. Kiss, *et al.,*
$^{70}Ge(p,\gamma)^{71}As$ and $^{76}Ge(p,n)^{76}As$ cross sections for the astrophysical p process: Sensitivity of the optical proton potential at low energies,
Physical Review C **76**, 055807 (2007)

[44] N. Özkan, *et al.,*
Astrophysical S factor for α-capture on ^{112}Sn in the p-process energy range,
Physical Review C **75**, 025801 (2007)

[45] M. S. Basunia, H. A. Shugart, A. R. Smith, and E. B. Norman,
Measurement of cross sections for α-induced reactions on ^{197}Au and thick-target yields for the (α,γ) process on ^{64}Zn and ^{63}Cu,
Physical Review C **75**, 015802 (2007)

[46] I. Căta-Danil, *et al.,*
Astrophysical S factor for α capture on ^{117}Sn,
Physical Review C **78**, 035803 (2008)

[47] W. Rapp, *et al.,*
Cross section measurements of α-induced reactions on $^{92,94}Mo$ and ^{112}Sn

for p-process studies,
Physical Review C **78**, 025804 (2008)

[48] C. Yalçın, *et al.,*
Odd p isotope ^{113}In: Measurement of α-induced reactions,
Physical Review C **79**, 065801 (2009)

[49] Gy. Gyürky, *et al.,*
Alpha-induced reaction cross section measurements on ^{151}Eu for the astrophysical γ-process,
Journal of Physics G: Nuclear and Particle Physics **37**, 115201 (2010)

[50] P. P. Povinec, M. Betti, A. J. T. Jull, and P. Vojtyla,
New isotope technologies in environmental physics,
Acta Physica Slovaca **58**(1), 1 (2008)

[51] John A. Cameron and Balraj Singh,
Nuclear Data Sheets for A = 40, NDS **102**(2), 293 (2004)

[52] `http://www.nndc.bnl.gov`

[53] P. K. F. Grieder,
Cosmic rays at Earth,
Elsevier Science B. V., Amsterdam (2001)

[54] J. Verplancke,
Low level gamma spectroscopy: low, lower, lowest,
Nucl. Inst. Meth. A **312**, 174 (1992)

[55] R. Wordel, *et al.,*
Study of neutron and muon background in low-level germanium gamma-ray spectrometry,
Nucl. Inst. Meth. A **369**, 557 (1996)

[56] G. Heusser,
Cosmic ray-induced background in Ge-spectrometry,
Nucl. Inst. Meth. B **83**, 223 (1993)

[57] G. Fehrenbacher, R. Meckbach, and H. G. Paretzke
Fast neutron detection with germanium detectors: computation of response functions for the 692 keV inelastic scattering peak,
Nucl. Inst. Meth. A **372**, 239 (1996)

[58] E. Browne,
Nuclear Data Sheets for A = 210, NDS **99**(3), 649 (2003)

[59] K. Bunzl and W. Kracke,
Natural radioactive contaminants in solder,
Nucl. Inst. Meth. A **238**, 191 (1985)

[60] R. L. Brodzinski, J. H. Reeves, F. T. Avignone, and H. S. Miley,
The impact of natural radioactivity in solder on low background experiments,
Nucl. Inst. Meth. A **254**, 472 (1987)

[61] Y. A. Akovali,
Nuclear Data Sheets for A = 222, NDS **77**(1), 271 (1996)

[62] G. Heusser,
Low-radioactivity background techniques,
Annual Review of Nuclear and Particle Science **45**, 543 (1995)

[63] E. Browne and J. K. Tuli,
Nuclear Data Sheets for A = 220, NDS **112**(4), 1115 (2011)

[64] P. Vojtyla,
Influence of shield parameters on cosmic-muon induced backgrounds of Ge γ-spectrometers,
Nucl. Inst. Meth. B **111**, 163 (1996)

[65] K. Shizuma, K. Fukami, K. Iwatani, and H. Hasai,
Low-background shielding of Ge detectors for the measurement of residual ^{152}Eu radioactivity induced by neutrons from the Hiroshima atomic bomb,
Nucl. Inst. Meth. B **66**, 459 (1992)

[66] H. Wulandari, J. Jochum, W. Rau, and F. von Feilitzsch,
Neutron flux at the Gran Sasso underground laboratory revisited,
Astroparticle Physics **22**, 313 (2004)

[67] P. Belli, *et al.,*
Deep underground neutron flux measurement with large BF_3 counters
Nuovo Cimento della Societa Italiana di Fisica A **101**, 959 (1989)

[68] F. Arneodo, *et al.,*
Neutron background measurements in the Hall C of the Gran Sasso

Laboratory
Nuovo Cimento della Societa Italiana di Fisica A **112**, 819 (1999)

[69] S. Niese,
Underground laboratories for low-level radioactivity measurements,
Radioactivity in the Environment **11**, 209 (2008)

[70] C. Broggini, D. Bemmerer, A. Guglielmetti, and R. Menegazzo,
LUNA: Nuclear Astrophysics Deep Underground,
Annual Review of Nuclear and Particle Science **60**, 53 (2010)

[71] *Long Range Plan: Perspectives of Nuclear Physics in Europe*
(NuPECC, 2010),
`http://www.nupecc.org/index.php?display=lrp2010/main`

[72] G. Heusser,
Cosmic ray interaction study with low-level Ge-spectrometry,
Nucl. Inst. Meth. A **369**, 539 (1996)

[73] G. Heusser,
Studies of γ-ray background with a low level germanium spectrometer,
Nucl. Inst. Meth. B **58**, 79 (1991)

[74] G. Duchêne, *et al.,*
The Clover: a new generation of composite Ge detectors,
Nucl. Inst. Meth. A **432**, 90 (1999)

[75] Z. Elekes, *et al.,*
Absolute full-energy peak efficiency calibration of a Clover–BGO detector system,
Nucl. Inst. Meth. A **503**, 580 (2003)

[76] A. A. Sonzogni,
Nuclear Data Sheets for A = 138, NDS **98**(3), 515 (2003)

[77] F. C. L. Crespi, *et al.,*
Alpha–gamma discrimination by pulse shape in $LaBr_3$:Ce and $LaCl_3$:Ce,
Nucl. Inst. Meth. A **602**, 520 (2009)

[78] M. Köhler, *et al.,*
A new low-level γ-ray spectrometry system for environmental radioactivity

at the underground laboratory Felsenkeller,
Applied Radiation and Isotopes **67**, 736 (2009)

[79] S. Niese, M. Köhler, and B. Gleisberg,
Low-level counting techniques in the underground laboratory "Felsenkeller" in Dresden,
Journal of Radioanalytical and Nuclear Chemistry **233**, 167 (1998)

[80] W. Helbig, S. Niese, and D. Birnstein,
Untergrundlaboratorium für Messungen geringer Radioaktivität,
Isotopenpraxis **20**, 60 (1984)

[81] F. Krüger, K. Zuber, D. Degering, A. Wagner, and T. Wester
Charakterisierung der Höhenstrahlungskomponente im Niederniveau-Messlabor Felsenkeller/Dresden,
DPG Spring Meeting; Bonn, Germany, 15–19 Marc, 2010
`http://iktp.tu-dresden.de/IKTP/pub/10/FelixKruegerDPG2010.1.pdf`

[82] M. Marta, *et al.* (LUNA Collaboration),
The $^{14}N(p,\gamma)^{15}O$ reaction studied with a composite germanium detector,
Physical Review C **83**, 045804 (2011)

[83] M. Marta, *et al.* (LUNA Collaboration),
Precision study of ground state capture in the $^{14}N(p,\gamma)^{15}O$ reaction,
Physical Review C **78**, 022802(R) (2008)

[84] T. Szücs, *et al.* (LUNA Collaboration),
An actively vetoed Clover γ-detector for nuclear astrophysics at LUNA,
The European Physical Journal A **44**, 513 (2010)

[85] K. Fushimi, *et al.,*
Determination of Th-chain contamination in a high sensitivity detector,
Nucl. Inst. Meth. A **491**, 163 (2002)

[86] D. Bemmerer, *et al.* (LUNA Collaboration),
Feasibility of low-energy radiative-capture experiments at the LUNA underground accelerator facility,
The European Physical Journal A **24**, 313 (2005)

[87] E. G. Adelberger, *et al.,*
Solar fusion cross sections. II. The pp chain and CNO cycles,
Review of Modern Physics **83**, 195 (2011)

[88] L. R. Buchmann and C. A. Barnes,
Nuclear reactions in stellar helium burning and later hydrostatic burning stages,
Nuclear Physics A **777**, 254 (2006)

[89] J. José and C. Iliadis,
Nuclear astrophysics: the unfinished quest for the origin of the elements,
Reports on Progress in Physics **74**, 096901 (2011)

[90] H. Costantini, *et al.,*
$^{16}O(\alpha,\gamma)^{20}Ne$ S factor: Measurements and R-matrix analysis,
Physical Review C **82**, 035802 (2010)

[91] S. Dababneh, *et al.,*
Stellar He burning of ^{18}O: A measurement of low-energy resonances and their astrophysical implications,
Physical Review C **68**, 025801 (2003)

[92] S. Seuthe, *et al.,*
Production and properties of implanted targets,
Nucl. Inst. Meth. A **260**, 33 (1987)

[93] D. Bemmerer, *et al.* (LUNA Collaboration),
Direct measurement of the $^{15}N(p,\gamma)^{16}O$ total cross section at novae energies,
Journal of Physics G: Nuclear and Particle Physics **36**, 045202 (2009)

[94] B. Aharmim, *et al.* (SNO Collaboration),
Independent Measurement of the Total Active ^{8}B Solar Neutrino Flux Using an Array of ^{3}He Proportional Counters at the Sudbury Neutrino Observatory,
Physical Review Letters **101**, 111301 (2008)

[95] Workshop on *"Underground nuclear-reaction experiments for astrophysics and application"*
Dresden, Germany, 28–30 April, 2010
`http://www.hzdr.de/felsenkeller`

[96] Workshop on *"LUNA-MV at Gran Sasso"*
Assergi, Italy, 10–11 February, 2011
`http://luna.lngs.infn.it/luna-mv`

[97] Workshop on *"Nuclear Astrophysics at LSC"*
Canfranc Estación, Spain, 22–23 March, 2012
`http://nuclear.fis.ucm.es/nucastro`

[98] D. Bemmerer, K. Zuber, and T. Szücs
A possible accelerator laboratory in the Dresden Felsenkeller
11th International Symposium on Nuclei in the Cosmos (NIC XI)
Heidelberg, Germany, 19–23 July, 2010

[99] T. Szücs, D. Bemmerer, T. Cowan, and K. Zuber
A possible underground accelerator in the Dresden Felsenkeller
Nuclear Physics in Astrophysics V. (NPA5),
Eilat, Israel, 3–8 April, 2011
Journal of Physics: Conference Series **337**, 012032 (2012)

[100] D. Karamanis,
Efficiency simulation of HPGe and Si(Li) detectors in γ- and X-ray spectroscopy,
Nucl. Inst. Meth. A **505**, 282 (2003)

[101] Z. Halász, *et al.,*
Alpha-capture on ^{130}Ba for the synthesis of p-isotopes,
Physical Review C **85**, 025804 (2012)

[102] Balraj Singh,
Nuclear Data Sheets for A = 172, NDS **75**(2), 199 (1995)

[103] V. S. Shirley,
Nuclear Data Sheets for A = 173, NDS **75**(2), 377 (1995)

[104] S. A. E. Johansson, J. L. Campbell, and K. G. Malmqvist
Particle Induced X-ray Emission Spectroscopy (PIXE),
John Wiley & Sons Inc., New York (1995)

[105] C. Arpesella,
A Low Background Counting Facility at Laboratori Nazionali del Gran Sasso,
Applied Radiation and Isotopes **47**, 991 (1996)

[106] M. Bauer, *et al.,*
MaGe: a Monte Carlo framework for the Gerda and Majorana double beta

decay experiments,
Journal of Physics: Conference Series **39**, 362 (2006)

[107] O. Tarasov and D. Bazin LISE Code, Version 9.3, available at `http://lise.nscl.msu.edu/lise.html`

[108] SRIM Code, Version 2006.02, available at `http://www.srim.org/`

[109] `http://nucastro.org/nonsmoker.html`

[110] L. McFadden, G. R. Satchler,
Optical-model analysis of the scattering of 24.7 MeV alpha particles Nuclear Physics **84**, 177 (1966)

[111] T. Rauscher, *et al.,*
submitted to Physical Review C

[112] J. Katakura,
Nuclear Data Sheets for A = 125, NDS **112**(3), 495 (2011)

[113] Yu. Khazov, I. Mitropolsky, and A. Rodionov,
Nuclear Data Sheets for A = 131, NDS **107**(11), 2715 (2006)

[114] M. Kanbe and K. Kitao,
Nuclear Data Sheets for A = 128, NDS **94**(2), 227 (2001)

[115] A. A. Sonzogni,
Nuclear Data Sheets for A = 134, NDS **103**(1), 1 (2004)

[116] N. Nica,
Nuclear Data Sheets for A = 140, NDS **108**(7), 1287 (2007)

[117] Coral M. Baglin,
Nuclear Data Sheets for A = 166, NDS **109**(5), 1103 (2008)

[118] Coral M. Baglin,
Nuclear Data Sheets for A = 179, NDS **110**(2), 265 (2009)